UNIVERSIDAD DE CHILE
FACULTAD DE CIENCIAS FÍSICAS Y MATEMÁTICAS
DEPARTAMENTO DE INGENIERÍA ELÉCTRICA

CONTINUOUS CONTROL SET MODEL PREDICTIVE CONTROL APPLIED TO MODULAR MULTILEVEL CONVERTERS FOR DRIVE AND WIND ENERGY APPLICATIONS

TESIS PARA OPTAR AL GRADO DE
DOCTOR EN INGENIERÍA ELÉCTRICA

YEINER ARIAS ESQUIVEL

PROFESOR GUÍA:
ROBERTO CÁRDENAS DOBSON

MIEMBROS DE LA COMISIÓN:
PATRICIO MENDOZA ARAYA
JAVIER PEREDA TORRES
MARCELO PÉREZ LEIVA
DORIS SÁEZ HUEICHAPAN

Este trabajo ha sido parcialmente financiado por:
FONDECYT 1221392, AC3E BASAL FB0008 y MICITT-PINN-CON-524-2019

SANTIAGO DE CHILE
2023

RESUMEN DE LA TESIS PARA OPTAR
AL GRADO DE DOCTOR EN INGENIERÍA ELÉCTRICA
POR: YEINER ARIAS ESQUIVEL
FECHA: 2023
PROF. GUÍA: ROBERTO CÁRDENAS DOBSON

CONTROL PREDICTIVO CONTINUO APLICADO A CONVERTIDORES MODULARES MULTINIVEL PARA APLICACIONES DE ACCIONAMIENTO Y ENERGÍA EÓLICA

El Convertidor Modular Multinivel (MMC) ha ganado atención en aplicaciones de alta potencia y voltaje medio debido a su modularidad, eficiencia y baja distorsión armónica. Esta tesis propone tres esquemas de control innovadores basados en el Control Predictivo de Modelo de Conjunto Continuo (CCS-MPC) para regular las tensiones de los capacitores del MMC. El primer enfoque utiliza un CCS-MPC de dos etapas para gestionar corrientes circulantes y controlar fluctuaciones de tensión. El segundo enfoque usa un CCS-MPC de una sola etapa para regular las tensiones y corrientes simultáneamente. Además, se presenta un tercer enfoque que implementa un CCS-MPC de un MMC Híbrido con generador sincrónico de imanes permanentes para energía eólica, asegurando el equilibrio de las tensiones en los capacitores sin utilizar corrientes circulantes. Estas estrategias mejoran el rendimiento y minimizan pérdidas del MMC. Además, estas fueron validadas experimentalmente y publicadas en revistas prestigiosas. Esta investigación también contribuye a otros proyectos relacionados con el control de convertidores modulares multinivel.

RESUMEN DE LA TESIS PARA OPTAR
AL GRADO DE DOCTOR EN INGENIERÍA ELÉCTRICA
POR: YEINER ARIAS ESQUIVEL
FECHA: 2023
PROF. GUÍA: ROBERTO CÁRDENAS DOBSON

CONTINUOUS CONTROL SET MODEL PREDICTIVE CONTROL APPLIED TO MODULAR MULTILEVEL CONVERTERS FOR DRIVE AND WIND ENERGY APPLICATIONS

In recent years, the Modular Multilevel Converter (MMC) has gained attention for high-power and medium-voltage applications due to its modularity, efficiency, and low harmonic distortion. However, achieving optimal MMC operation requires multiple control objectives. Maintaining capacitor voltage within an acceptable range and reducing circulating current are key challenges in MMC control. This doctoral thesis proposes three innovative control schemes based on Continuous Control Set Model Predictive Control (CCS-MPC) to regulate MMC capacitor voltages. The first approach employs a two-stage CCS-MPC to manage circulating currents and control voltage fluctuations. The second approach uses a single-stage CCS-MPC to govern voltage oscillations and circulating currents simultaneously. Additionally, a third approach is presented, implementing CCS-MPC for a Hybrid Modular Multilevel Converter integrated with a direct-drive Permanent Magnet Synchronous Generator in wind energy applications. This approach ensures converter energy balance without the need for circulating currents. The proposed control strategies improve MMC performance, minimise losses, and have been experimentally validated, with publications in reputable journals. The research also contributes to other projects related to modular multilevel converter control.

A mi esposa,
y a mi madre.

Acknowledgements

I would like to express my deepest gratitude to the Ministerio de Ciencia, Tecnología y Telecomunicaciones, as well as the Instituto Tecnológico de Costa Rica, for their invaluable support during my doctoral studies at the University of Chile. Additionally, I am grateful for the financial support provided by the Fondecyt 1221392 and the project AC3E basal FB0008, Advanced Centre for Electrical and Electronic Engineering.

The completion of this thesis would not have been possible without the unwavering help and support of my supervisor, colleagues, friends, and family. Their guidance, encouragement, and belief in me have been instrumental throughout this journey. I am truly fortunate to have such a remarkable network of individuals who have stood by me and pushed me to achieve my best.

Table of Content

List of Tables

List of Figures

List of Acronyms

CCS	Continuous Control Set
CC	Central Controller
CHB	Cascaded H-bridge
CPS	Cyber-Physical System
CSC	Current Source Converters
CVO	Capacitor Voltage Oscillation
FC	Flying Capacitor
FCS	Finite Control Set
FDIA	False Data Injection Attack
HFM	High-Frequency Mode
HIL	Hardware-in-the-loop
HVDC	High-Voltage Direct Current
IPD	In-Phase Carrier Disposition
LC	Local Controller
LCC	Line-Commutated Converter
LFM	Low-Frequency Mode
MIMO	Multiple-Input Multiple-Output
MMC	Modular Multilevel Converter
MPC	Model Predictive Control
MPPT	Maximum Power Point Tracking
NPC	Neutral-Point clamped
PCC	Point of Common Coupling
PMSG	Permanent Magnet Synchronous Generator
PWM	Pulse Width Modulation
RL	Reinforcement Learning
SISO	Single-Input Single-Output
SM	Submodule
STATCOM	Static Synchronous Compensator
THD	Total Harmonic Distortion
VSC	Voltage Source Converter
WECS	Wind Energy Conversion System

Chapter 1

Introduction

1.1. Motivation

The Modular Multilevel Converter (MMC) has emerged as a compelling choice for various applications, including drive systems, High-Voltage Direct Current (HVDC) transmission, and Wind Energy Conversion Systems (WECS) [1–3]. There are several key reasons why the MMC is highly suitable for these applications. Firstly, the MMC offers numerous advantages such as high efficiency, modularity and scalability, allowing for easy adaptation to different power requirements [1, 4–7]. This flexibility makes it an ideal choice for high-power and medium-voltage drive and wind energy applications, where efficient and reliable operation is crucial. Secondly, in HVDC transmission, the MMC's unique characteristics make it an excellent candidate for long-distance power transmission [6]. Its ability to handle high voltages and currents, along with its low harmonic distortion capabilities, results in improved power quality, and enhanced overall system performance. Fig. 1.1 illustrates the MMC topology used throughout this thesis, consisting of six clusters, an AC port, a DC port, and six inductors. Each cluster is made up of "n" half/full-bridges, each equipped with a floating capacitor.

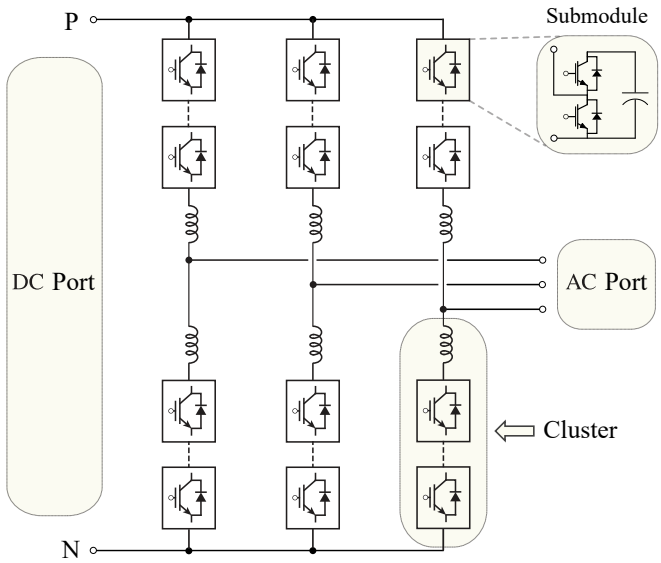

Figure 1.1: DC to three-phase Modular Multilevel Converter topology.

Despite the numerous benefits MMCs offer, achieving proper control of the converter is

quite challenging. This challenge is compounded by the Multiple-Input Multiple-Output (MIMO) characteristic of the converter, which requires accomplishing multiple control objectives. For instance, ensuring the accurate regulation of capacitor voltage, minimising circulating currents, and controlling both the AC and DC ports are essential for the converter's reliable operation [8, 9]. As highlighted in various publications (e.g., [10–12]), this becomes particularly complicated in drive applications, especially when dealing with low output frequencies at the AC port [8, 13–15].

The MMC requires an active balancing of its six energy components to effectively regulate the total energy stored in the MMC capacitors [16] and achieve operation at both high and low frequencies. At high frequencies, two circulating currents are utilised for energy balancing, each consisting of a DC component, a positive sequence AC component, and a negative sequence AC component [10]. Nonetheless, the commonly proposed solution in the literature is to design controllers that overlook the cross-coupling between the energy and circulating current components (e.g., as seen in [11, 17]), resulting in suboptimal performance [18, 19].

To enhance control performance, Multiple-Input Multiple-Output controllers have been suggested (see [18]). Nonetheless, traditional MIMO controllers struggle to incorporate constraints such as maximum current and maximum output voltage in each cluster [19]. Additionally, even in the case of decoupled controllers, achieving saturation limitations for currents and voltages proves to be challenging. For instance, as demonstrated in [16], implementing conventional anti-wind-up schemes typically used for Proportional-Integral (PI) controllers can result in suboptimal system performance.

In order to address these challenges, Model Predictive Control (MPC) has emerged as a potential solution for power converter control due to its versatility and simplicity [20, 21]. MPC algorithms can be designed to incorporate multiple constraints, enabling a fast dynamic response, and can be effectively applied to MIMO systems [4, 22, 23]. These characteristics position MPC as a promising alternative for controlling modular multilevel converters [24].

1.1.1. The MMC as an alternative topology for HVDC applications

In HVDC systems, Current Source Converters (CSC) have been widely used for the last several decades [25, 26]. The Line-Commutated Converter (LCC) topology is one of the first topologies proposed for these applications and is therefore considered a mature technology [22, 27]. This converter has a large transmission capacity and a high transmission voltage level. The circuit configuration of the LCC is shown in 1.2; as seen in the figure, this converter uses thyristors as switching devices.

In general, CSCs have a simple structure, low switching dv/dt, and high efficiency. Additionally, they exhibit robustness against over-current and short-circuit conditions. However, CSCs are characterised by low dynamic performance and significant harmonic distortion, which may not comply with the harmonic guidelines established by standards [28]. Moreover, the LCC configuration is prone to switching failures, necessitates reactive power compensation systems, and is not suitable for connections to weak networks [29]. Conversely, a LCC-based converter station typically has a size approximately 67 % larger than that of a voltage source converter station [30], primarily due to the inclusion of power compensation systems [31].

Although the MMC-based systems present multiple challenges from a control perspective,

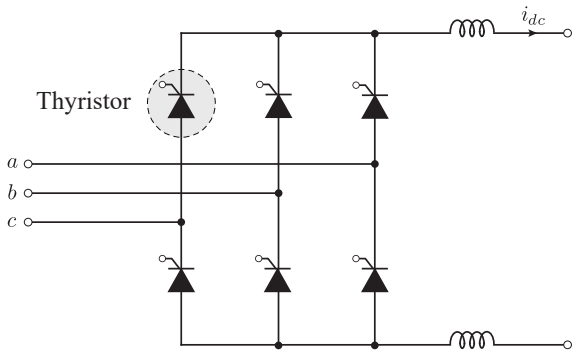

Figure 1.2: Three-phase six-pulse line-commutated current source converter.

the MMC has demonstrated clear advantages such as built-in redundancy, higher efficiency, and low harmonic distortion [32]. For example, according to [30], the transmission losses of MMC-based HVDC systems are similar to those of LCC-based systems. Furthermore, in a well-designed MMC, a high power density can be obtained because it does not require output filters and reactive power support compared to the LCC-based HVDC system [33]. These benefits make MMC a promising alternative, which is increasingly used in HVDC transmission networks.

1.1.2. The MMC as an alternative solution for medium to high power applications

Multilevel converter topologies have emerged as a solution to the limitations of two-level converters for medium- and high-voltage, high-power applications. Before the MMC, different types of multilevel converters were proposed in the literature to operate in these power and voltage ranges. Topologies such as Cascaded H-bridge (CHB), Neutral-Point clamped (NPC), or Flying Capacitor (FC) are typically used in high-power applications. However, these converters come with several drawbacks. Some examples of these topologies are shown in Fig. 1.3.

One of the major problems in NPC and FC converters is that they require an almost complete modification in the topology to increase the number of voltage levels. Additionally, these converters are not fault-tolerant, implying a complete shutdown during faults. In contrast, the CHB converter requires numerous isolated DC sources. Despite the modularity of the converter, DC sources must be generated using a phase-shifting transformer, increasing the cost and size of the converter.

To address these challenges, modular multilevel converter topologies have been proposed. The modularity of these converters enables the achievement of high operating voltages using low-voltage and cost-effective switches. Additionally, the MMC utilises flying capacitors without the need for isolated DC sources or a phase-shifting transformer. These key features make the MMC an attractive alternative for high-power applications.

Nowadays, the MMC topology is utilised in various commercial solutions, although most are related to HVDC systems [34]. Nevertheless, companies like Siemens and Benshaw offer solutions for medium-voltage drives. To the best of the author's knowledge, there are currently two alternatives available: the Sinamics Perfect Harmony GH150 and the M2L Series. The GH150 operates within a voltage range of 4 kV to 13.8 kV [35]. On the other hand, the M2L

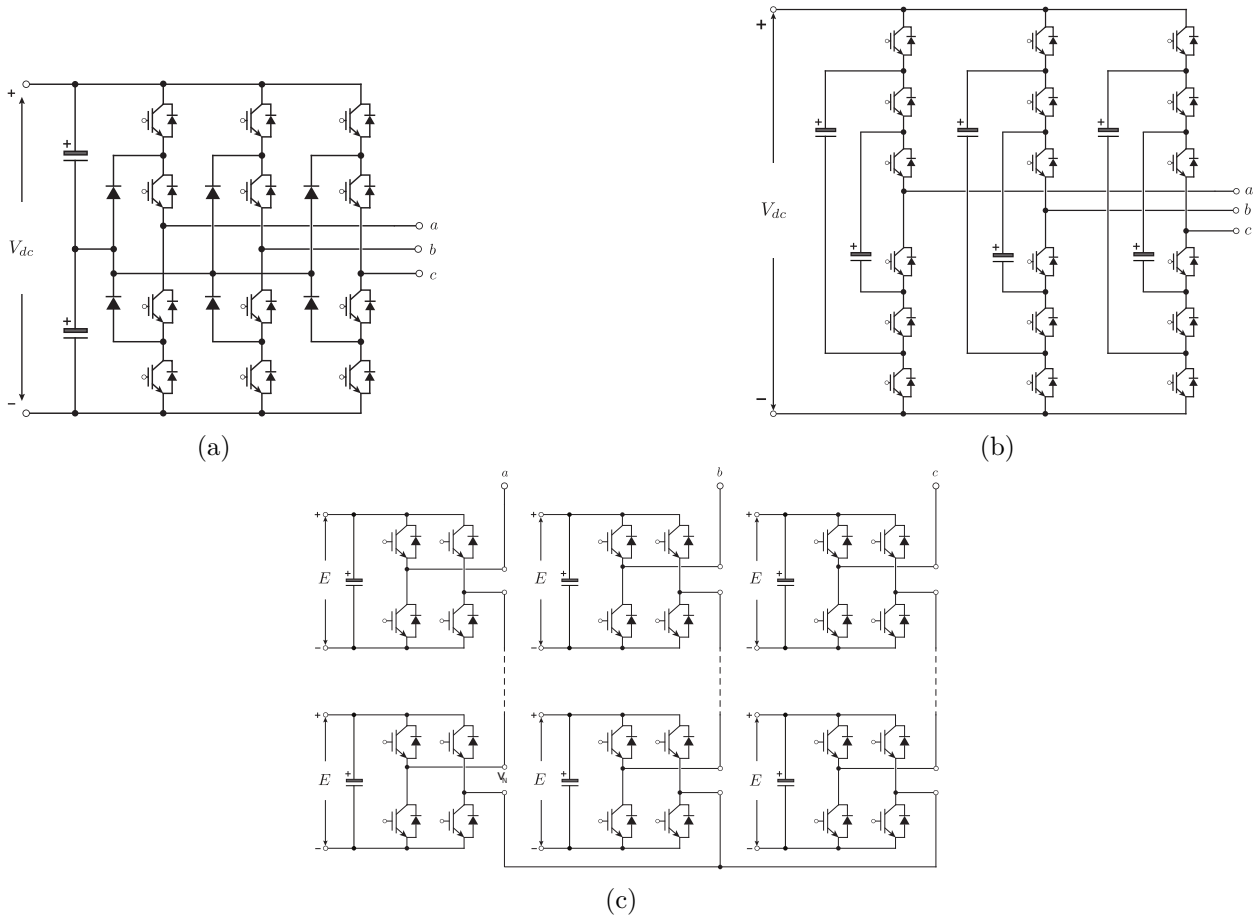

Figure 1.3: Multilevel converter topologies [22]. (a) Three-level neutral-point clamped converter, (b) Four-level flying capacitor converter, (c) Cascaded H-bridge converter.

is designed to function within a voltage range of 2.3 kV to 7.2 kV [36]. Both alternatives incorporate redundancy options to enhance reliability.

1.1.3. Control Challenges of an MMC Operating with Low Frequency at the AC Port

As mentioned before, control of the MMC is complex as multiple control objectives need to be reached simultaneously. This task is especially challenging when the output frequency at the AC port is low. The low-frequency power fluctuation issues are discussed below.

According to Fig. 1.4 and applying a small signal model, the capacitor voltage and the instantaneous power in the converter clusters can be obtained as [12, 13]:

$$nC\overline{v}_C^* \frac{dv_{Ca}^P}{dt} \approx p_a^P = v_a^P i_a^P \tag{1.1}$$

where v_{Ca}^P is the capacitor voltage, p_a^P is the instantaneous power, v_a^P is the output cluster voltage and i_a^P is the cluster current; $\overline{v}_C^*$, n, and C are the capacitor reference voltage, number of capacitors per cluster, and capacitance of each submodule, respectively. Then, ignoring the voltage drop across the cluster inductor and considering that neither circulating current nor

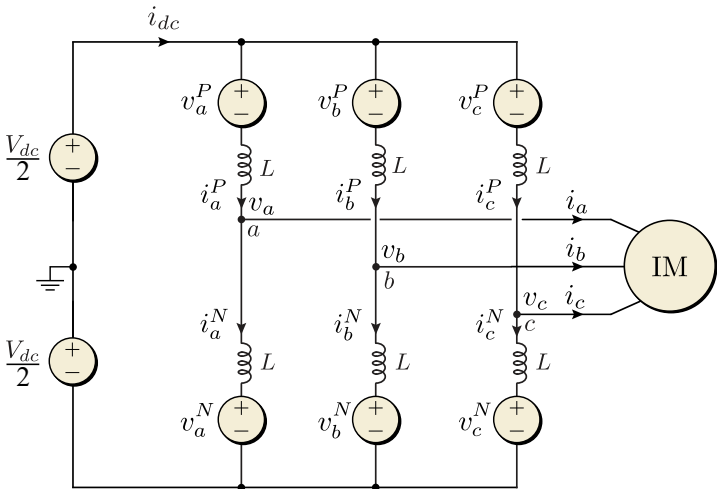

Figure 1.4: Model of the Modular Multilevel Converter.

common-mode voltage is used, the instantaneous power can be approximated as:

$$p_a^P \approx \frac{V_{dc} i_{dc}}{6} - \frac{V_a I_a}{4}\cos(\phi) + \frac{V_a I_a}{4}\cos\left(2\omega_e t + \phi\right) + \overbrace{\frac{V_{dc} I_a}{4}\sin\left(\omega_e t + \phi\right)}^{p_{crit}} - \frac{i_{dc} V_a}{3}\sin\left(\omega_e t\right) \quad (1.2)$$

where the voltage and current of the machine are $V_a \sin(\omega_e)$ and $I_a \sin(\omega_e + \phi)$, respectively. This analysis is performed using the upper cluster of leg A as an example; however, it can be extended to all clusters of the converter. The first two terms of the right side are non-oscillatory, and the remaining terms depend on the frequency of the machine. Nevertheless, if the starting current is high, the power oscillation p_{crit} with frequency ω_e will also be high. This low-frequency power could produce a high voltage ripple in capacitors, as seen in (1.3).

$$v_{Ca}^P \approx \overbrace{\left\{\frac{V_{dc} i_{dc}}{6} - \frac{V_a I_a}{4}\cos(\phi)\right\}}^{\textit{mean energy balance}} t + \frac{V_a I_a}{8\omega_e}\sin\left(2\omega_e t + \phi\right) - \frac{V_{dc} I_a}{4\omega_e}\cos\left(\omega_e t + \phi\right) + \frac{i_{dc} V_a}{3\omega_e}\cos\left(\omega_e t\right) \quad (1.3)$$

According to the numerical results presented in [37], the normalised peak-to-peak capacitor voltage fluctuation could be greater than 40 % of its dc mean value for the low-frequency range (see Fig. 1.5). Moreover, these capacitor voltage fluctuations can affect the voltage rating of semiconductors, make the system unstable or cause over-modulation. For these reasons, some authors suggest that voltage fluctuations should be less than 10 % of the DC means value to avoid these problems [9, 14]. The results shown in [37] were obtained for an induction machine whose specifications are summarised in Table 1.1.

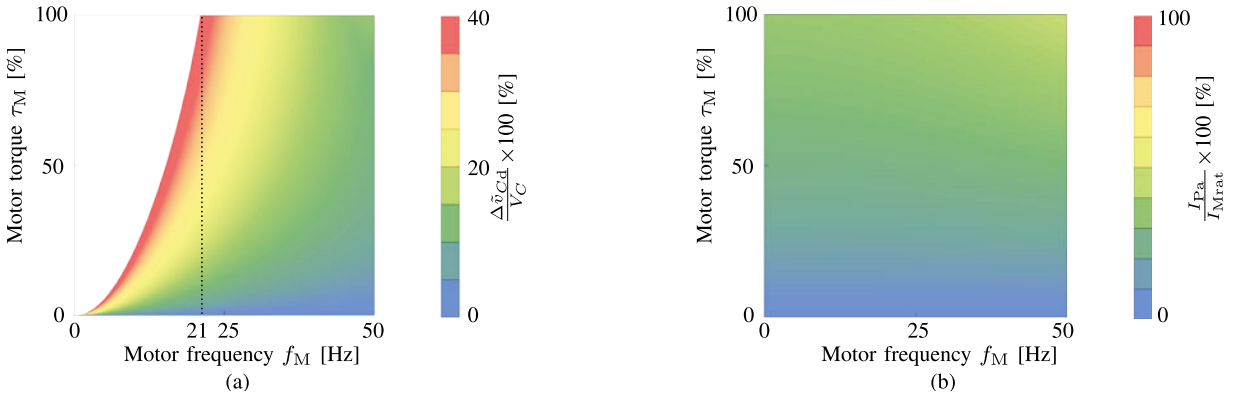

Figure 1.5: Normalised capacitor-voltage fluctuation and normalised cluster rms current [37]. (a) Capacitor-voltage fluctuation. (b) Cluster rms current.

Table 1.1: Parameters of the induction machine employed in [37].

Parameter	Value	Unit
Rated output power	15	kW
Rated frequency	50	Hz
Rated line-to-line rms voltage	380	V
Motor power factor	0.71	-
Rated rotating speed	1460	r/min
Rated stator rms current (I_{Mrat})	32	A
Mutual inductance	60	mH
Pole number	4	-
Moment of inertia	0.2	kgm^2

Due to high-voltage oscillations, circulating currents and common-mode voltage are often utilised to balance the converter energy and mitigate capacitor voltage fluctuations [9, 14, 38–41]. However, as shown in Fig. 1.5, power and voltage oscillations depend on the AC port's operating point (motor torque and frequency). For example, when the frequency of the machine increases, the voltage fluctuations naturally decrease due to the filtering effect of the capacitors. Nevertheless, simultaneously, the machine requires higher voltage, leading to a reduction in cluster voltages available for injecting a high common-mode voltage. As a result, most of the control strategies described in the literature employ different approaches based on the operating frequency [10, 11, 15].

The aforementioned analysis is equally applicable to any element connected to the AC port since, as discussed earlier, the DC-link voltage, the current in the cluster, and the operating frequency are the primary factors influencing voltage oscillations in the capacitors.

1.2. Hypotheses and Goals

The main hypotheses that support this thesis are presented below. This thesis explores using model predictive control strategies in modular multilevel converters for drive and wind energy applications. In drive applications, these strategies exhibit key characteristics such as optimal limitations on cluster currents and voltages within the MMC. Moreover, they offer a comparatively simpler control structure when compared to other control systems described in the literature. In the context of wind energy applications, the proposed strategy stands out for its prominent feature of eliminating the need for circulating currents to balance the voltages across the capacitors.

1. The power-voltage and voltage-current models of the MMC can be used to develop a two-stage CCS-MPC that regulates the capacitor voltages and circulating current references, including current and voltage constraints.

2. The optimal saturation of currents and voltages in the MMC can be achieved through the utilisation of CCS-MPC. This saturation is challenging to achieve using SISO-based anti-windup scheme algorithms. Limiting each component independently does not guarantee that the cluster current or voltage is properly limited or fully exploited.

3. It is not necessary to predefine the waveform, phase, and sequence of the circulating currents. Instead, these currents are obtained automatically by the algorithm. Therefore, if the common-mode voltage waveform or the output port frequency changes, the algorithm adjusts the circulating currents automatically, without modifying the control system. It is important to emphasise that this becomes indispensable when using Single-Input Single-Output-based control systems.

4. It is possible to utilise an external controller to adjust the weighting factors of the CCS-MPC cost function and maintain capacitor voltage fluctuations within an appropriate range. This enables the utilisation of the same control strategy for both high and low frequencies. In MMC control, ensuring the regulation of capacitor voltages within an acceptable range is imperative to guarantee the proper functioning of the converter. However, achieving this requirement at low frequencies presents a challenge. Additionally, the weighting factor controller can be employed to apply a consistent control strategy across both high and low frequencies, eliminating the need to define transition methods between regions.

5. The power-voltage and voltage-current models can be used to develop a one-stage CCS-MPC, including current and voltage constraints. Implementing a single optimisation problem to handle the capacitor voltages and circulating currents can reduce the computational burden compared to the two-stage CCS-MPC. This controller considers both dynamics and constraints in a single cost function.

6. In certain wind energy applications, and considering hybrid MMC, it is possible to achieve voltage balancing and mitigation of voltage oscillations in the capacitors without using circulating currents.

1.2.1. Project Goals

1.2.1.1. General Goal

To develop a new compact and straightforward CCS-MPC strategy that allows the operation of the Modular Multilevel Converter for drive and wind energy applications over the full range of frequencies, including an optimal limitation of cluster currents and voltages.

1.2.1.2. Specific Goals

1. To develop a CCS-MPC algorithm for achieving capacitor voltage balance in an MMC-based drive for induction machines across the entire operating range.
2. To design a CCS-MPC algorithm for controlling circulating currents, incorporating optimal limitation of the currents and voltages.
3. To propose a weight factor adaptation method to keep the capacitor voltages within the defined voltage oscillation band.
4. To integrate the voltage oscillations and circulating currents control in a single optimisation problem, including current and voltage constraints.
5. To analyse the computational burden of the proposed CCS-MPC algorithms.
6. To propose a CCS-MPC algorithm for the capacitor voltage balance in the full range of operation of the permanent magnet synchronous generator without requiring circulating currents.
7. To implement a HIL set-up and simulate the proposed control strategies.
8. To build an experimental prototype of an 18-cell (each) 5 kW back-to-back hybrid-MMC, for validating the control strategies discussed in this document.

1.3. Summary of Contributions

Below is a list of the contributions made to the state of the art, which clearly demonstrates the impact of this doctoral work, as well as some of the conclusions associated with the work conducted. Therefore, the following contributions were obtained at the end of this Ph.D. research:

1. A two-stage CCS-MPC strategy for regulating capacitor voltages and circulating currents in MMC-based drives is developed in this work (see Chapter 2). The CCS-MPC methodology effectively addresses the challenges of voltage and current saturation, which are difficult to achieve with conventional linear controllers due to multiple frequency components and positive/negative sequences in each cluster current. The proposed CCS-MPC algorithm simplifies saturation control by considering maximum current and voltage constraints, achieving optimal saturation without over-modulation. The MIMO design approach offers advantages over SISO designs by accounting for cross-couplings between state variables. The CCS-MPC algorithm automatically determines waveform shape, frequency, electrical sequences, and phase shifts for circulating currents without

predefined parameters. Experimental results demonstrate high performance and seamless transition between low-frequency and high-frequency operation with the proposed CCS-MPC algorithm.

2. An enhanced single-stage two-step CCS-MPC algorithm for MMC operating with variable output frequency is also developed (see Chapter 3). The algorithm employs a predictive control strategy for regulating capacitor voltages and balancing energy using circulating currents. A single cost function incorporating MMC states and constraints leads to a single global optimum. A compensating algorithm based on the Moore-Penrose pseudoinverse matrix effectively reduces circulating currents and improves MMC efficiency, particularly at low frequencies. The control methodologies enable fixed weight-cost matrices for low-frequency and high-frequency operation. Experimental validation using an 18-cell MMC prototype driving a 7.5 kW-cage induction machine demonstrates excellent dynamic and steady-state performance with reduced computational burden.

3. A CCS-MPC approach was proposed for a hybrid-MMC driving a direct-drive PMSG in variable speed wind energy applications (see Chapter 4). The CCS-MPC algorithm controls common-mode and DC-link voltages, enabling operation within a predetermined range. The control system allows the grid-side converter to function at a higher DC-link voltage, reducing the required DC-link current. Experimental validation demonstrates that the reference for common-mode voltage, obtained using a Moore-Penrose pseudoinverse matrix algorithm, is a third harmonic waveform that balances capacitor voltages and increases the modulation index. The proposed control system is validated using a system composed of two 5 kW hybrid-MMCs in a back-to-back configuration, showing excellent performance in variable-speed and fixed-speed wind profiles.

1.4. Published Works

Presented below is a compilation of papers generated as an outcome of this doctoral project, categorised into two sections: published papers and papers currently pending publication or undergoing the review process.

1.4.1. Published Papers:

1. Y. Arias-Esquivel, R. Cárdenas, M. Urrutia, M. Díaz, L. Tarisciotti, and J. C. Clare, "Continuous Control Set Model Predictive Control of a Modular Multilevel Converter for Drive Applications," *IEEE Transactions on Industrial Electronics*, vol. 70, no. 9, pp. 8723–8733, 2023, doi: 10.1109/TIE.2022.3210515. Q1 journal paper. Impact Factor: 7.7. **Abstract:** The Modular Multilevel Converter is a good alternative for high power, medium voltage drive applications due to its modularity and scalability. However, the control is complex and typically involves several highly-coupled circulating current feedback loops implemented using Single-Input Single-Output design tools. Additionally, each circulating current has many different frequency components and electrical sequences to increase the degrees of freedom in the controller. In this work, the use of Continuous Control Set Model Predictive Control is proposed in order to include cross-coupling and interactions between the state variables and consider the system constraints, such as maximum current and maximum output voltage. The controller is intended for drive applications and is designed to operate with good dynamic performance over the entire

speed range of the machine. The control methodology proposed is experimentally validated using an 18-cell MMC prototype driving a cage machine. Additional experimental tests are performed using PLECS-RT HIL platforms.

2. Y. Arias-Esquivel, R. Cárdenas, L. Tarisciotti, M. Díaz, and A. Mora, "A Two-Step Continuous-Control-Set MPC for Modular Multilevel Converters Operating with Variable Output Voltage and Frequency," *IEEE Transactions on Power Electronics*, vol. 38, no. 10, pp. 12091–12103, 2023, doi: 10.1109/TPEL.2023.3288490. Q1 journal paper. Impact Factor: 6.7.
   Abstract: This paper presents a new enhanced single-stage two-step Continuous Control Set Model Predictive Control (CCS-MPC) algorithm, for Modular Multilevel Converters (MMCs) operating with variable output frequency at the AC port. The proposed two-step CCS-MPC allows the implementation of feed-forward compensation of the one-step ahead perturbations at the AC side, using an algorithm based on the Moore–Penrose pseudoinverse matrix. Limitations of the current and voltages in the MMC clusters are implemented to avoid overmodulation and overcurrents, being the solution of the constrained CCS-MPC online solved using the active-set method. Without losing generality, the experimental validation of the single-stage CCS-MPC is performed using an 18-cell MMC prototype, driving a 7.5 kW cage induction machine operating in a wide speed range. A dSPACE MicroLabBox platform is used to control the MMC-based drive by implementing the CCS-MPC algorithm, the modulation stage and the active-set method. It is experimentally demonstrated that the compensation of the low-frequency perturbations allows a considerable reduction in the required circulating currents at the low-frequency operation of the drive. Reduction in the capacitor voltage ripple, improved efficiency, and a smaller Total Harmonic Distortion (THD) in the output currents are also achieved with the proposed single-stage two-step CCS-MPC.

3. C. Burgos-Mellado, C. Zuñiga-Bauerle, D. Muñoz, Y. Arias-Esquivel, R. Cárdenas-Dobson, T. Dragičević, F. Donoso, A. Watson, "Reinforcement Learning-Based Method to Exploit Vulnerabilities of False Data Injection Attack Detectors in Modular Multilevel Converters," *IEEE Transactions on Power Electronics*, vol. 38, no. 7, pp. 8907-8921, 2023, doi: 10.1109/TPEL.2023.3263728. Q1 journal paper. Impact Factor: 6.7.
   Abstract: Implementing control schemes for modular multilevel converters (M2Cs) involves both a cyber and a physical level, leading to a cyber-physical system (CPS). At the cyber level, a communication network enables the data exchange between sensors, control platforms, and monitoring systems. Meanwhile, at the physical level, the semiconductor devices that comprise the M2C are switched ON/OFF by the control system. In this context, almost all published works in this research area assume that the CPS always reports correct information. However, this may not be the case when the M2C is affected by cyber-attacks, such as the one named false data injection attack (FDIA), where the data seen by the control system is corrupted through illegitimate data intrusion into the CPS. To deal with this situation, FDIA detectors for the M2C are recently starting to be studied, where the goal is to detect and mitigate the attacks and the attacked sub-modules. This paper proposes a reinforcement learning (RL)-based method to uncover the deficiencies of existing FDIAs detectors used for M2C applications. The proposed method auto-generates complex attack sequences able to bypass FDIA detectors. Therefore, it points out the weaknesses of current detectors: This valuable information can be used later to improve the performance of the detectors, establishing more reliable

cybersecurity solutions for M2Cs. The RL environment is developed in Matlab/Simulink augmented by PLECS/blockset, and it is made available to researchers on a website to motivate future research efforts in this area. Hardware-in-the-loop (HIL) studies verify the proposal's effectiveness.

4. C. Gallardo, C. Burgos-Mellado, D. Muñoz, Y. Arias-Esquivel, A. Kumar-Verma, A. Navas-Fonseca, R. Cárdenas-Dobson, T. Dragičević, "Reinforcement Learning-based False Data Injection Attacks Detector for Modular Multilevel Converters," *IEEE Transactions on Industrial Electronics*, 2023, doi: 10.1109/TIE.2023.3312433. Q1 journal paper. Impact Factor: 7.7.
   Abstract: The modular multilevel converter (MMC) is a prominent solution for medium to high-voltage, high-power conversion applications. Recently, distributed control strategies have been proposed to make this converter modular in terms of software and control hardware. In this control architecture, high-level control tasks are performed by a central controller (CC), whereas low-level control tasks are achieved by local controllers (LCs) placed on the MMC sub-modules. The CC and LCs use a cyber-physical system (CPS) to share all the necessary information to execute their respective control schemes. In this context, the CPS is vulnerable to cyber-attacks, such as the false data injection attack (FDIA), where the data seen by the controllers is corrupted through illegitimate data intrusion. This cyber-attack may degrade the MMC performance, producing suboptimal or even unstable operations. Even more, diverse FDIAs can be generated using artificial intelligence methods to deceive FDIA detectors. This paper proposes an FDIA detector based on the reinforcement learning (RL) technique to detect sophisticated FDIAs targeting the MMC control system. The performance of the proposed RL-based FDIA detector is verified via Hardware-in-the-loop (HIL) studies, showing its effectiveness in detecting sophisticated attack sequences affecting the MMC control system.

1.4.2. Papers Submitted or Pending Publication:

1. Y. Arias-Esquivel, R. Cárdenas, M. Díaz, and L. Tarisciotti, "Continuous Control Set Model Predictive Control of a Hybrid-MMC for Wind Energy Applications," *IEEE Transactions on Industrial Electronics*, 2023. Q1 journal paper. Impact Factor: 7.7.
   Abstract: This paper discusses a continuous control set model predictive control system of a hybrid modular multilevel converter, driving a direct drive permanent magnet synchronous generator, for variable-speed wind energy applications. The hybrid converter enables operation at a reduced DC-link voltage without the need for circulating currents, even during low-frequency operation in the AC port. To further reduce cluster currents, the capacitor voltages are allowed to oscillate inside predefined voltage limits. The control system is based on a single-step predictive control algorithm, whose outputs are the DC-link and common-mode voltages required to balance the converter energy. Furthermore, it is demonstrated in this work that the reference for the common-mode voltage, obtained using an algorithm based on the Moore-Penrose pseudo-inverse matrix, is a third harmonic waveform which can be used to balance the capacitor voltages, as well as increase the modulation index. The proposed control system is validated using a Hardware-in-the-Loop platform and an experimental system consisting of a 5 kW back-to-back hybrid modular multilevel converter, controlled using dSPACE MicroLabBox platforms. The generator is emulated using a programmable power supply.

2. A. Navas-Fonseca, C. Burgos-Mellado, Y. Arias-Esquivel, A. Kumar-Verma, A. Mora, D. Muñoz and R. Cárdenas-Dobson, "Distributed predictive control for capacitor voltage balancing in a Cascaded H-Bridge Based STATCOM," In *Power Electronics and Application (EPE), 2023 25th European Conference.*
   Abstract: This paper proposes a distributed model predictive control (DMPC) scheme for inter-cell and inter-cluster capacitor voltage balancing control of a cascaded H-bridge multilevel static synchronous compensator (STATCOM). The proposed DMPC does not require a central controller to perform these control tasks as they are cooperatively performed by local controllers placed in the STATCOM cells. Three case scenarios are analysed to highlight the features of the proposed control scheme. The results demonstrate that the DMPC scheme is able to manage large communication delays and communication failures.

1.5. Outline of the Dissertation

This thesis follows the "thesis by published papers" format of the University of Chile. According to this format, the Ph.D. candidate is required to have a minimum of two accepted journal papers, which are then incorporated as chapters in the thesis. Since each paper is self-contained, there may be some repetition between chapters, as they discuss similar or related information. Depending on the supervisor's requirements, additional chapters or appendices can be included.

Hence, this thesis consists of chapters corresponding to three journal papers where the author is the first author. Two of these papers have already been published in IEEE Transactions on Industrial Electronics (TIE) and IEEE Transactions on Power Electronics (TPEL), both esteemed journals with first-quartile rankings and impact factors of 7.7 and 6.7, respectively. The third paper is currently undergoing the first round of review for publication in IEEE Transactions on Industrial Electronics.

Due to the thesis format, the hypotheses, contributions, and overall conclusions of this project are closely intertwined with the papers used as chapters. The correlation between these elements is presented in Table 1.2.

Table 1.2: Structure and relation of this thesis

Chapter	Related paper	Hypothesis						Contribution		
		1	2	3	4	5	6	1	2	3
2	(2) (TIE)	✗	✗	✗	✗			✗		
3	(3) (TPEL)		✗	✗		✗			✗	
4	(4) (Submiteed TIE)						✗			✗

Chapter 2

Continuous Control Set Model Predictive Control of a Modular Multilevel Converter for Drive Applications

This chapter is based on the journal paper:

Y. Arias-Esquivel, R. Cárdenas, M. Urrutia, M. Díaz, L. Tarisciotti, and J. C. Clare, "Continuous Control Set Model Predictive Control of a Modular Multilevel Converter for Drive Applications," *IEEE Transactions on Industrial Electronics*, vol. 70, no. 9, pp. 8723–8733, 2023, doi: 10.1109/TIE.2022.3210515. Q1 journal paper. Impact Factor: 7.7.

Abstract: The Modular Multilevel Converter is a good alternative for high power, medium voltage drive applications due to its modularity and scalability. However, the control is complex and typically involves several highly-coupled circulating current feedback loops implemented using Single-Input Single-Output design tools. Additionally, each circulating current has many different frequency components and electrical sequences to increase the degrees of freedom in the controller. In this work, the use of Continuous Control Set Model Predictive Control is proposed in order to include cross-coupling and interactions between the state variables and consider the system constraints, such as maximum current and maximum output voltage. The controller is intended for drive applications and is designed to operate with good dynamic performance over the entire speed range of the machine. The control methodology proposed is experimentally validated using an 18-cell MMC prototype driving a cage machine. Additional experimental tests are performed using PLECS-RT HIL platforms.

2.1. Introduction

The Modular Multilevel Converter (MMC) was proposed by Marquardt in 2003 [42], for high-voltage DC transmission [8, 43]. However, in recent years its use has been extended to applications such as Medium-Voltage Motor Drives, Power Quality Improvement [4, 10], etc. The popularity of this converter for high-power applications is due, among other reasons, to its power and voltage scalability, high efficiency and reduced dv/dt in the voltages [8]. The MMC topology is shown in Fig. 2.1; the converter is composed of six clusters, an AC port, a DC port, and six inductors. Each cluster consists of "n" half-bridges each of them equipped with a floating capacitor.

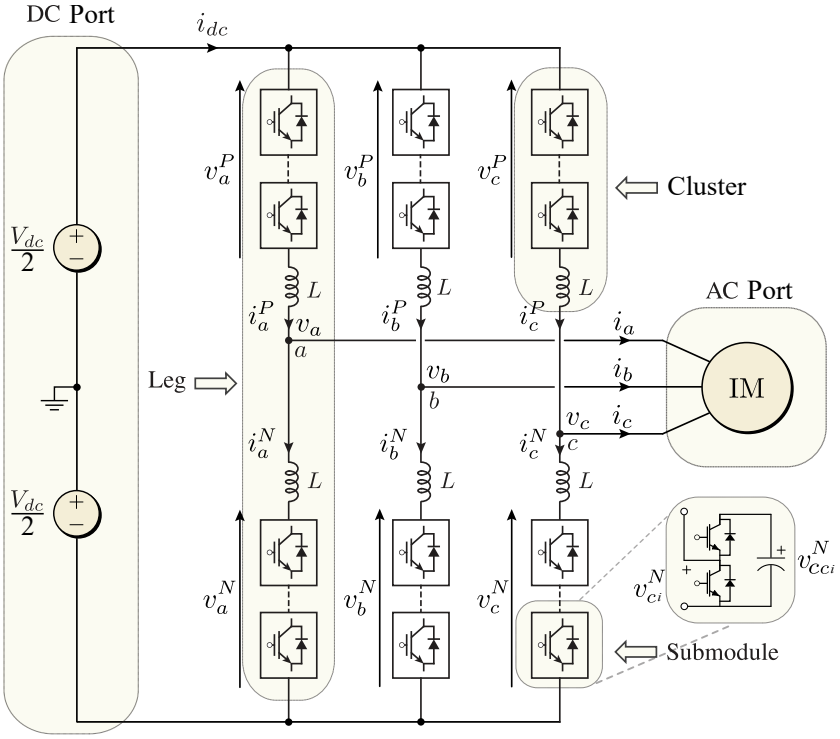

Figure 2.1: Modular Multilevel Converter Topology.

Control of the MMC is complex, considering the Multiple-Input Multiple-Output (MIMO) characteristic of the converter, where multiple control objectives have to be achieved. For example, it is necessary to regulate the voltage of the floating capacitors, balance the energy stored in each arm, regulate the circulating currents, and control the currents and voltages at the AC and DC ports [8, 9]. As reported in several publications (e.g. [10–12]) this is difficult to achieve for drive applications, particularly when the output frequency at the AC port is low [8, 13, 15]. For these applications, the operating range is typically divided into two modes, namely Low-Frequency Mode (LFM) and High-Frequency Mode (HFM) [9, 10, 13]. Each of these operating modes requires a different control strategy typically based on multiple Single-Input Single-Output (SISO) designed control loops. Although LFM and HFM separation provides control of an MMC-based drive over the entire operating range [10, 11, 15], better dynamic performance can be achieved using MIMO controllers [44].

The MMC has six energy components which have to be actively balanced, to control the total energy stored in the MMC capacitors [16] and to achieve LFM or HFM operation. For example, during HFM, two circulating currents are utilised for energy balancing purpo-

ses; however, each circulating current comprises a DC component, a positive sequence AC component and a negative sequence AC component [10]. The solution normally proposed in the literature is to design the controllers neglecting cross-coupling between the energies and the circulating current components (e.g. see [11, 17]), rendering sub-optimal performance [18, 19]. To improve the control performance, MIMO controllers have been proposed in [18]. Nevertheless, conventional MIMO controllers cannot include constraints such as maximum current and maximum output voltage in each arm [19]; moreover, saturation limitation of the currents and voltages is difficult to achieve even in the case of decoupled SISO controllers. For instance, as demonstrated in [16], the implementation of anti-windup schemes to limit separate components of the circulating currents, renders a sub-optimal saturation performance for the total current.

Recently, Model Predictive Control (MPC) has been proposed for power converter control due to its flexibility and simplicity [20, 21]. MPC algorithms can be designed to include multiple constraints, achieving a fast dynamic response, and can be applied to MIMO systems [4, 22]. For power electronic applications, the most widely used MPC methodology is based on Finite Control Set (FCS) algorithms or FCS-MPC [45]. However, FCS-MPC schemes produce variable switching frequency [46, 47] and, for converter structures with a high number of switching states, may result in an unfeasible computational burden for the control platform (see [4]). Conversely, a Continuous Control Set (CCS) MPC algorithm offers a constant switching frequency [48] and the external modulation stage reduces the computational burden [19, 49] of the MPC algorithm. In fact, unlike the conventional FCS-MPC applications to MMC, where the computational burden is heavily dependent on the total number of SMs (see [4, 48]), the computational burden of the proposed CCS-MPC is relatively low and has an almost fixed value which is independent of the number of half-bridge cells.

There are relatively few publications proposing CCS-MPC algorithms for MMC control. In [48], a simplified optimisation problem with only two constraints is proposed and graphically solved. In [19], more constraints are used to limit the total currents in the MMC and the arm voltages. A MATLAB solver is used in [19] to obtain the solution of the optimisation problem and the proposed methodology has been validated using simulation. Neither [48], nor [19] discuss control methods that can be applied to MMC-based drives where the voltage and frequency at the AC port are variable.

In this work, a two-stage CCS-MPC algorithm is proposed. The outer CCS-MPC regulates the MMC capacitor voltages while the inner CCS-MPC regulates the currents. The decoupled model discussed in [11, 12] is used to implement the CCS-MPC. When compared to previous work in the area of MMC control for drive applications, the contributions of this work are: 1) The first CCS-MPC algorithm proposed for the control of MMC-based drives is presented and experimentally validated using an 18-cell MMC-based prototype driving a cage machine. It is experimentally shown that two MIMO CCS-MPC algorithms can replace ten or even more SISO controllers typically used in MMC-based drive applications. 2) The implementation of the proposed CCS-MPC is simplified when compared to conventional control systems reported in the literature. For instance, in [9, 11–13], the parameters of the circulating currents, such as waveform shape, phase, electrical sequence, frequency, among others, have to be predefined. This is unnecessary and automatically accomplished using the proposed CCS-MPC algorithm. 3) Optimal limitation of the arm currents and voltages in an MMC is easily achieved with CCS-MPC using constraints [50], while it is extremely problematic in a conventional control system [11, 16]; 4) The proposed CCS-MPC algorithm can operate in either LFM or HFM with a seamless optimal transition between modes, in contrast to other

control systems reported in [10, 11, 40].

The rest of this paper is organised as follows. In Section 2.2, the MMC modelling is briefly described. The MPC formulation to regulate the capacitor voltages and circulating currents are provided in Section 2.3. In Section 2.4 hardware in the loop results are discussed and, in Section 2.5, experimental work is presented. Finally, Section 2.6 presents the conclusions.

2.2. Modelling of the MMC

The decoupled model of the MMC discussed in this section has been reported in previous works [10, 12], and for completeness, it is briefly addressed here. This work utilises the $\Sigma\Delta\alpha\beta 0$-transformation to represent the voltages and currents of the MMC. Using the transformed currents and voltages a simplified decoupled model is obtained (see [10, 12]).

The $\Sigma\Delta\alpha\beta 0$-transformation is defined by

$$[X]^{\Sigma\Delta}_{\alpha\beta 0} \doteq [T]_{\Sigma\Delta} \cdot [X]^{PN}_{abc} \cdot [C]_{\alpha\beta 0} \tag{2.1}$$

where $[X]^{PN}_{abc}$ represents the matrix with the instantaneous abc variables (e.g. capacitor voltages, arm currents, etc.) to be transformed, and the matrices $[T]_{\Sigma\Delta}$ and $[C]_{\alpha\beta 0}$ are given by

$$[T]_{\Sigma\Delta} = \begin{bmatrix} \frac{1}{2} & \frac{1}{2} \\ 1 & -1 \end{bmatrix} \quad , \quad [C]_{\alpha\beta 0} = \begin{bmatrix} \frac{2}{3} & 0 & \frac{1}{3} \\ -\frac{1}{3} & \frac{1}{\sqrt{3}} & \frac{1}{3} \\ -\frac{1}{3} & -\frac{1}{\sqrt{3}} & \frac{1}{3} \end{bmatrix} \tag{2.2}$$

By applying this transformation to the converter voltages and currents, the dynamics of the MMC can be divided into two models, as shown below. Using the circuit of Fig. 2.1 and applying Kirchhoff's voltage law, the current-voltage model describing the dynamics of the currents is defined as [15]

$$\frac{V_{dc}}{2}\begin{bmatrix} 1 & 1 & 1 \\ 1 & 1 & 1 \end{bmatrix} = \begin{bmatrix} v_a^P & v_b^P & v_c^P \\ v_a^N & v_b^N & v_c^N \end{bmatrix} + L\frac{d}{dt}\begin{bmatrix} i_a^P & i_b^P & i_c^P \\ i_a^N & i_b^N & i_c^N \end{bmatrix} + \begin{bmatrix} v_a & v_b & v_c \\ -v_a & -v_b & -v_c \end{bmatrix} \tag{2.3}$$

Then, applying (2.1) to (2.3) yields the following transformed model:

$$\frac{1}{2}\begin{bmatrix} 0 & 0 & V_{dc} \\ 0 & 0 & 0 \end{bmatrix} = \begin{bmatrix} v_\alpha^\Sigma & v_\beta^\Sigma & v_0^\Sigma \\ v_\alpha^\Delta & v_\beta^\Delta & v_0^\Delta \end{bmatrix} + L\frac{d}{dt}\begin{bmatrix} i_\alpha^\Sigma & i_\beta^\Sigma & \frac{1}{3}i_{dc} \\ i_\alpha & i_\beta & 0 \end{bmatrix} + 2\begin{bmatrix} 0 & 0 & 0 \\ v_\alpha & v_\beta & v_0 \end{bmatrix} \tag{2.4}$$

where i_α^Σ and i_β^Σ are the arm circulating currents, i_{dc} is the DC port current, v_0 is the common-mode voltage and v_α, v_β, i_α and i_β are the machine voltages and currents. These variables are expressed in $\alpha\beta 0$-coordinates.

The instantaneous cluster power can be obtained by using the voltages and currents[12, 13], i.e., $p_i^j = v_i^j i_i^j \; \forall \; i \in \{a, b, c\}$ and $j \in \{P, N\}$. Assuming that the capacitor voltages are close to the reference $\overline{v}_C^*$, this power is related to the voltage of the capacitors using the approximation:

$$\frac{d}{dt}\begin{bmatrix} v_{Ca}^P & v_{Cb}^P & v_{Cc}^P \\ v_{Ca}^N & v_{Cb}^N & v_{Cc}^N \end{bmatrix} \approx \frac{1}{nC\overline{v}_C^*}\begin{bmatrix} p_a^P & p_b^P & p_c^P \\ p_a^N & p_b^N & p_c^N \end{bmatrix} \tag{2.5}$$

where n is the number of capacitors per cluster, C is the capacitance of each submodule and v_{Ca}^{P}, v_{Cb}^{P}, etc., are the capacitor voltages. Applying the $\Sigma\Delta\alpha\beta 0$-transformation to the power-voltage model of (2.5) yields,

$$\frac{d}{dt}\begin{bmatrix} v_{C\alpha}^{\Sigma} & v_{C\beta}^{\Sigma} & v_{C0}^{\Sigma} \\ v_{C\alpha}^{\Delta} & v_{C\beta}^{\Delta} & v_{C0}^{\Delta} \end{bmatrix} \approx \frac{1}{nC\overline{v}_{C}^{*}}\begin{bmatrix} p_{\alpha}^{\Sigma} & p_{\beta}^{\Sigma} & p_{0}^{\Sigma} \\ p_{\alpha}^{\Delta} & p_{\beta}^{\Delta} & p_{0}^{\Delta} \end{bmatrix} \tag{2.6}$$

Replacing (2.3) and (2.4) in (2.6) and after several manipulations (2.7) is obtained (see [10, 12]); notice that in (2.7) the symbol "$\circ$" represents the dot product between vectors and the superscript "c" is the complex conjugate operator. The power $\underline{p}_{\alpha\beta}^{\Sigma} = p_{\alpha}^{\Sigma} + jp_{\beta}^{\Sigma}$ is a vector that represents the power that is transferred between the converter phases.

$$\underline{p}_{\alpha\beta}^{\Sigma} = \frac{1}{2}V_{dc}\underline{i}_{\alpha\beta}^{\Sigma} - \frac{1}{4}\left(\underline{i}_{\alpha\beta}\underline{v}_{\alpha\beta}\right)^{c} - \frac{1}{2}v_{0}\underline{i}_{\alpha\beta} \tag{2.7a}$$

$$\underline{p}_{\alpha\beta}^{\Delta} = \frac{1}{2}V_{dc}\underline{i}_{\alpha\beta} - \frac{2}{3}i_{dc}\underline{v}_{\alpha\beta} - \left(\underline{v}_{\alpha\beta}\underline{i}_{\alpha\beta}^{\Sigma}\right)^{c} - 2v_{0}\underline{i}_{\alpha\beta}^{\Sigma} \tag{2.7b}$$

$$p_{0}^{\Delta} = -\left(\underline{v}_{\alpha\beta}\circ\underline{i}_{\alpha\beta}^{\Sigma}\right) - \frac{2}{3}i_{dc}v_{0} \tag{2.7c}$$

$$p_{0}^{\Sigma} = \frac{1}{6}V_{dc}i_{dc} - \frac{1}{4}\left(\underline{v}_{\alpha\beta}\circ\underline{i}_{\alpha\beta}\right) \tag{2.7d}$$

The vector $\underline{p}_{\alpha\beta}^{\Delta}$ and the scalar p_{0}^{Δ} represent the power flow between the upper and lower clusters. Finally, in (2.7d), p_{0}^{Σ} represents the power that is transferred between the AC port and the DC port of the MMC; this latter power is not considered in the MPC formulation since it does not depend on the circulating currents.

2.3. Proposed Control Scheme for the MMC

A control system based on nested CCS-MPC algorithms is designed and implemented as shown in Fig. 2.2. The outer CCS-MPC regulates the voltages of (6), with the exception of ${v_{C0}}^{\Sigma}$, which is dependent on p_{0}^{Σ} [see (2.7d) above] and is regulated by a PI controller. The inner CCS-MPC regulates the circulating current $\underline{i}_{\alpha\beta}^{\Sigma}$ while balancing of the cell-capacitor voltages in each cluster is performed by a sorting-based modulation algorithm [21]. As extensively discussed in [11], during LFM operation, the voltage $v_{C\alpha\beta}^{\Delta}$ is approximately equal to the total capacitor voltage oscillation around the cluster average voltage. Therefore, in Fig. 2.2 the reference $v_{Cd}^{\Delta *}$ represents the peak magnitude of $|v_{C\alpha\beta}^{\Delta}|$ which is desired (or allowable) in the capacitor voltage oscillations during LFM.

In this work, it is assumed that the MMC is feeding an induction machine that is controlled using a conventional rotor-flux orientated vector control method (see [12, 17]) which is implemented outside the proposed CCS-MPC algorithm. Fig. 2.3 shows the control block diagram for the AC [Fig. 2.3(a)] and DC [Fig. 2.3(b)] ports, where v_{dF}^{Δ} and v_{qF}^{Δ} are feed-forward terms, and ω_0 is the frequency of v_0. During LFM, a trapezoidal common-mode voltage interacting with the circulating currents [see the term $2v_{0}\underline{i}_{\alpha\beta}^{\Sigma}$ in (2.7b)] is used to compensate the large low-frequency capacitor voltage oscillations. As discussed in Section 2.1, circulating currents must include multiple frequency components to balance the capacitor voltages properly. However, note that the current waveforms will have trapezoidal components at LFM to compensate for power oscillations caused by the $0.5V_{dc}\underline{i}_{\alpha\beta}$ term when a trapezoidal

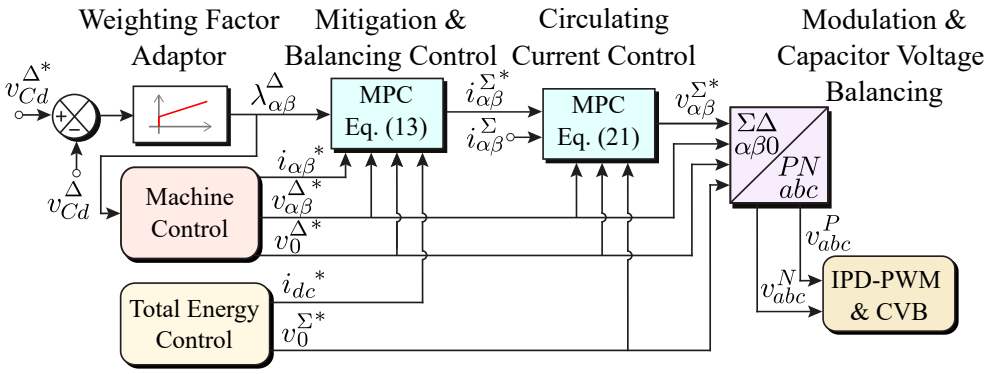

Figure 2.2: Overall Control Scheme for the Modular Multilevel Converter. The term $v_{Cd}^{\Delta *}$ represents the maximum oscillation allowed at low frequency operation.

common-mode voltage is used. The trapezoidal waveform allows the magnitude of the circulating currents to be reduced. A comparative study on the effects of using sinusoidal and square wave circulating currents is presented in [51]. The amplitude of the common-mode voltage is regulated using (2.8). In this equation, a voltage margin of $\approx 20\,\%$ in the cluster voltages is considered to ensure control of the circulating currents [40, 52, 53] and to manage external perturbations. As shown, (2.8) assumes that the machine stator voltage is dependent on a V/F relationship; therefore, the voltage margin to synthesise V_o during LFM is larger. The trapezoidal voltage is automatically removed at HFM using the information from the weighting factor controller (see Section 2.3.2).

$$V_0 = \frac{0.8V_{dc}}{2}\left(1 - \frac{\omega_e}{\omega_n}\right) \tag{2.8}$$

where ω_n is the nominal machine frequency.

Finally, to solve the CCS-MPC problem, an active-set method is used [54]. For optimal problems with a reduced number of restrictions, such as the one discussed in this work, the active-set algorithm is usually one of the best in terms of speed and accuracy compared to methods such as interior-point or gradient projection [55, 56]. Details concerning the implementation of the algorithm are discussed extensively in [16], and a detailed description of the active-set method is presented in [50], chapter 16.

2.3.1. Mitigation and Balancing Control

For balancing purposes, a discrete-time state model of the system is obtained by substituting (2.7a) - (2.7c) in (2.6) and applying the forward Euler approximation. Considering a sample time T_s, the discrete-time model is given by (2.9), where $K = T_s/(nC\overline{v}_C^*)$. To avoid the unfeasible computational burden typically produced by a long prediction horizon [57], a single-step prediction algorithm is implemented in this work.

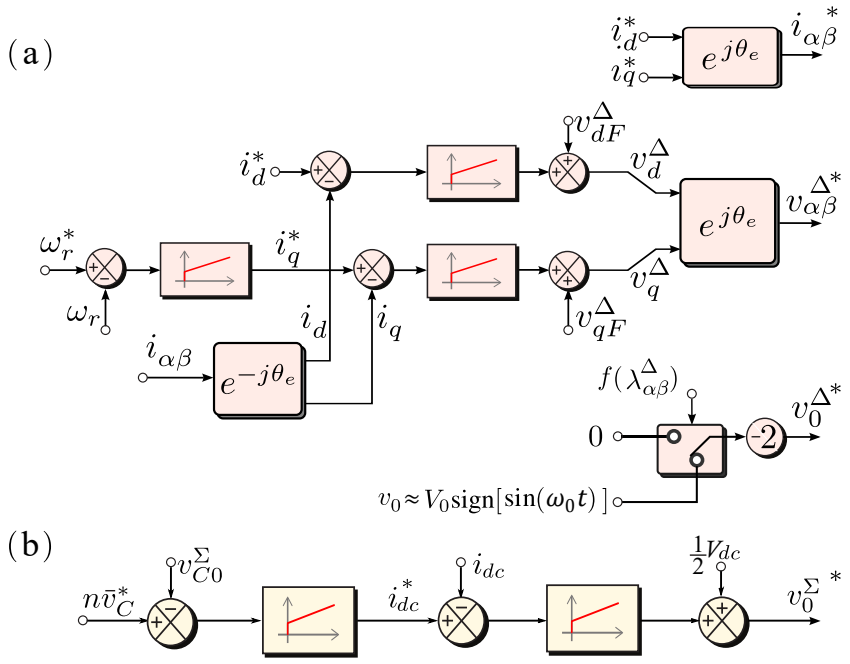

Figure 2.3: AC and DC port controllers. (a) Machine Control and (b) Total Energy Control.

$$
\underbrace{\begin{bmatrix} v_{C\alpha}^{\Delta}(k+1) \\ v_{C\beta}^{\Delta}(k+1) \\ v_{C0}^{\Delta}(k+1) \\ v_{C\alpha}^{\Sigma}(k+1) \\ v_{C\beta}^{\Sigma}(k+1) \end{bmatrix}}_{\mathbf{x}_{k+1}} \approx \underbrace{\begin{bmatrix} 1 & 0 & 0 & 0 & 0 \\ 0 & 1 & 0 & 0 & 0 \\ 0 & 0 & 1 & 0 & 0 \\ 0 & 0 & 0 & 1 & 0 \\ 0 & 0 & 0 & 1 & 1 \end{bmatrix}}_{\mathbf{A}} \underbrace{\begin{bmatrix} v_{C\alpha}^{\Delta}(k) \\ v_{C\beta}^{\Delta}(k) \\ v_{C0}^{\Delta}(k) \\ v_{C\alpha}^{\Sigma}(k) \\ v_{C\beta}^{\Sigma}(k) \end{bmatrix}}_{\mathbf{x}_k}
$$

$$
+ \underbrace{K \begin{bmatrix} -v_\alpha(k) - 2v_0(k) & v_\beta(k) \\ v_\beta(k) & v_\alpha(k) - 2v_0(k) \\ -v_\alpha(k) & -v_\beta(k) \\ \frac{1}{2}V_{dc} & 0 \\ 0 & \frac{1}{2}V_{dc} \end{bmatrix}}_{\mathbf{B}} \underbrace{\begin{bmatrix} i_\alpha^{\Sigma}(k) \\ i_\beta^{\Sigma}(k) \end{bmatrix}}_{\mathbf{u}_k}
$$

$$
+ \underbrace{K \begin{bmatrix} \frac{1}{2}V_{dc}i_\alpha(k) - \frac{2}{3}i_{dc}(k)v_\alpha(k) \\ \frac{1}{2}V_{dc}i_\beta(k) - \frac{2}{3}i_{dc}(k)v_\beta(k) \\ -\frac{2}{3}i_{dc}(k)v_0(k) \\ \frac{1}{4}i_\beta(k)v_\beta(k) - \frac{1}{4}i_\alpha(k)v_\alpha(k) - \frac{1}{2}i_\alpha(k)v_0(k) \\ \frac{1}{4}i_\beta(k)v_\alpha(k) + \frac{1}{4}i_\alpha(k)v_\beta(k) - \frac{1}{2}i_\beta(k)v_0(k) \end{bmatrix}}_{\mathbf{d}_k} \tag{2.9}
$$

Using (2.9) the discrete state space equations can be written as

$$\mathbf{x}_{k+1} = \mathbf{A}\mathbf{x}_k + \mathbf{B}\mathbf{u}_k + \mathbf{d}_k \tag{2.10}$$

The one-step delay compensation algorithm presented in [58] is applied to (2.10). The formulation of the outer CCS-MPC stage is given by:

$$\begin{aligned} \min_{\mathbf{x}_{k+1},\mathbf{u}_k} \quad & \mathbf{x}_{k+1}^T \mathbf{Q} \mathbf{x}_{k+1} + \mathbf{u}_k^T \mathbf{R} \mathbf{u}_k \\ \text{s.t.} \quad & \mathbf{x}_{k+1} = \mathbf{A} x_k + \mathbf{B}\mathbf{u}_k + \mathbf{d}_k \\ & \mathbf{G}\mathbf{u}_k \geq \mathbf{W} \end{aligned} \tag{2.11}$$

where $\mathbf{x}_k$ is the state vector measured at time instant k, $\mathbf{x}_{k+1}$ are the prediction of the state vector at time $k+1$, and $\mathbf{u}_k$ is the control vector. $\mathbf{A}$ is the system matrix, $\mathbf{B}$ is the input matrix, and $\mathbf{Q}$, $\mathbf{R}$ are the weighting matrices that penalise the states and control actions, respectively. Finally, $\mathbf{d}_k$ represents the set of measurable disturbances in the system, and $\mathbf{G}$, $\mathbf{W}$ are the constraints imposed on the control actions. The weighting matrices are diagonal and defined as:

$$\mathbf{Q} = \mathbf{Diag}[\lambda_\alpha^\Delta, \lambda_\beta^\Delta, \lambda_0^\Delta, \lambda_\alpha^\Sigma, \lambda_\beta^\Sigma],\ \mathbf{R} = \mathbf{Diag}[\lambda_\alpha^U, \lambda_\beta^U] \tag{2.12}$$

In this work matrices $\mathbf{Q}$ and $\mathbf{R}$ are both positive definite and, for LFM operation, the weighting factors λ_α^Δ and λ_β^Δ are modified online as a function of the magnitude of the capacitor voltage oscillations (see the block labelled "weighting factor adaptor" in Fig. 2.2). This approach is further discussed in Section 2.3.2. The remaining weighting factors are defined as 1.

To simplify the optimal problem [16, 44, 45], the equality constraint of (2.11) is included in the cost function, yielding:

$$\begin{aligned} \min_{\mathbf{u}_k} \quad & \mathbf{u}_k^T \mathbf{H} \mathbf{u}_k + 2\left[(\mathbf{A}\mathbf{x}_k + \mathbf{d}_k)^T \mathbf{F}\right] \mathbf{u}_k \\ \text{s.t.} \quad & \mathbf{G}\mathbf{u}_k \geq \mathbf{W} \end{aligned} \tag{2.13}$$

where

$$\begin{aligned} \mathbf{H} &= \mathbf{B}^T \mathbf{Q} \mathbf{B} + \mathbf{R} \\ \mathbf{F} &= \mathbf{Q}\mathbf{B} \end{aligned} \tag{2.14}$$

Solving (2.13) (by implementing the active-set method in the control platform), the optimal circulating current vector $\underline{i}_{\alpha\beta}^\Sigma$ is obtained. Matrices $\mathbf{H}$ and $\mathbf{F}$ have to be updated at each sampling time since the system is a time variant. Notice that in (2.9), the common-mode voltage is included as a disturbance. For LFM operation, the optimal circulating currents are automatically obtained by solving (2.13) and considering v_0. Notice that the pre-definition of circulating current frequency, waveform shapes, phase shifts and sub-component sequences is no longer required. This feature is one of the important contributions of this paper and it is also applicable to HFM operation.

For saturation limitation to the cluster currents, the circulating currents are limited to $\pm i_{max}$ by the CCS-MPC outer stage; the value of i_{max} is selected considering the thermal

limits of the MMC devices and components (see [16]). To perform this limitation, the cluster currents are defined in $\Sigma\Delta\alpha\beta 0$ coordinates as:

$$\begin{bmatrix} i_a^P \\ i_b^P \\ i_c^P \\ i_a^N \\ i_b^N \\ i_c^N \end{bmatrix} = \begin{bmatrix} \frac{1}{3}i_{dc} + \frac{1}{2}i_\alpha + i_\alpha^\Sigma \\ \frac{1}{3}i_{dc} - \frac{1}{4}i_\alpha - \frac{1}{2}i_\alpha^\Sigma + \frac{\sqrt{3}}{2}i_\beta^\Sigma + \frac{\sqrt{3}}{4}i_\beta \\ \frac{1}{3}i_{dc} - \frac{1}{4}i_\alpha - \frac{1}{2}i_\alpha^\Sigma - \frac{\sqrt{3}}{2}i_\beta^\Sigma - \frac{\sqrt{3}}{4}i_\beta \\ \frac{1}{3}i_{dc} - \frac{1}{2}i_\alpha + i_\alpha^\Sigma \\ \frac{1}{3}i_{dc} + \frac{1}{4}i_\alpha - \frac{1}{2}i_\alpha^\Sigma + \frac{\sqrt{3}}{2}i_\beta^\Sigma - \frac{\sqrt{3}}{4}i_\beta \\ \frac{1}{3}i_{dc} + \frac{1}{4}i_\alpha - \frac{1}{2}i_\alpha^\Sigma - \frac{\sqrt{3}}{2}i_\beta^\Sigma + \frac{\sqrt{3}}{4}i_\beta \end{bmatrix} \tag{2.15}$$

Limiting these currents to $-i_{max} \leq i_i^j \leq i_{max}\ \forall\ i \in \{a,b,c\}$ and $j \in \{P,N\}$ produces a total of 12 constraints. However, after analysing (2.15) the constraints can be reduced to six, by exploiting symmetries in the currents i_x^P and i_x^N of phase "x", $\forall\ x \in \{a,b,c\}$. After some manipulation, (2.16) and (2.17) are obtained:

$$\underbrace{\begin{bmatrix} -1 & 0 \\ \frac{1}{2} & -\frac{\sqrt{3}}{2} \\ \frac{1}{2} & \frac{\sqrt{3}}{2} \\ 1 & 0 \\ -\frac{1}{2} & \frac{\sqrt{3}}{2} \\ -\frac{1}{2} & -\frac{\sqrt{3}}{2} \end{bmatrix}}_{\mathbf{G}} \begin{bmatrix} i_\alpha^\Sigma(k) \\ i_\beta^\Sigma(k) \end{bmatrix} \geq \underbrace{\begin{bmatrix} -i_{max} - \min(i_1, i_4) \\ -i_{max} - \min(i_2, i_5) \\ -i_{max} - \min(i_3, i_6) \\ -i_{max} + \max(i_1, i_4) \\ -i_{max} + \max(i_2, i_5) \\ -i_{max} + \max(i_3, i_6) \end{bmatrix}}_{\mathbf{W}} \tag{2.16}$$

$$\begin{bmatrix} i_1 \\ i_2 \\ i_3 \\ i_4 \\ i_5 \\ i_6 \end{bmatrix} = \begin{bmatrix} -\frac{1}{3}i_{dc}(k) - \frac{1}{2}i_\alpha(k) \\ -\frac{1}{3}i_{dc}(k) + \frac{1}{4}i_\alpha(k) - \frac{\sqrt{3}}{4}i_\beta(k) \\ -\frac{1}{3}i_{dc}(k) + \frac{1}{4}i_\alpha(k) + \frac{\sqrt{3}}{4}i_\beta(k) \\ -\frac{1}{3}i_{dc}(k) + \frac{1}{2}i_\alpha(k) \\ -\frac{1}{3}i_{dc}(k) - \frac{1}{4}i_\alpha(k) + \frac{\sqrt{3}}{4}i_\beta(k) \\ -\frac{1}{3}i_{dc}(k) - \frac{1}{4}i_\alpha(k) - \frac{\sqrt{3}}{4}i_\beta(k) \end{bmatrix} \tag{2.17}$$

2.3.2. On-Line Adaptation of the Cost Function Weights

The optimal algorithm of (2.13) is designed to drive the voltage unbalances in the capacitors to zero. However, when the system is operating at LFM, a relatively large circulating current interacting with the common mode voltage v_0 [see (2.7b)] is required to drive the voltage vector $\underline{v}_{C\alpha\beta}^\Delta$ to zero. Nevertheless, as discussed in previous publications [9, 11], the converter can perform adequately when the capacitor voltage oscillations are maintained within a band of $\approx 10\,\%$ of the reference voltage. To achieve this target a variable weight strategy is proposed and the weights $\lambda_\alpha^\Delta = \lambda_\beta^\Delta$ are obtained from the output of a PI controller (see Fig. 2.2) which acts on the error between a banded reference $v_{Cd}^{\Delta *}$ and the peak oscillating voltage obtained from the capacitor voltage measurements [processed using the $\Sigma\Delta\alpha\beta 0$ transform of (2.2)]. As discussed in [11], during LFM operation, the voltage v_{Cd}^Δ is approximately equal to the peak magnitude of the capacitor voltage oscillations. A complete discussion of the relationship between the voltage fluctuations and v_{Cdq}^Δ is presented in [11].

The weighting factor control is implemented in a $d-q$ frame rotating at the frequency of

the AC port (ω_e) and orientated along the voltage vector $\underline{v}^{\Delta}_{C\alpha\beta}$. When the AC-port frequency ω_e increases, the voltage oscillations $\underline{v}^{\Delta}_{C\alpha\beta}$ naturally decrease due to the filtering effect of the submodule capacitors. This allows the implementation of a simple seamless transition between LFM to HFM and vice versa, i.e. when the weights $\lambda^{\Delta}_{\alpha\beta}$ are below a predefined threshold, the system is considered in HFM; therefore, the trapezoidal common-mode voltage v_0 could be reduced or indeed it is no longer required.

2.3.3. Circulating Current Control

In this work, a second inner CCS-MPC stage is proposed to control the circulating currents (see Fig. 2.2) with the model being obtained from (2.4). To obtain a discrete-time model of the currents the forward Euler approximation is applied.

$$\underbrace{\begin{bmatrix} i^{\Sigma}_{\alpha}(k+1) \\ i^{\Sigma}_{\beta}(k+1) \end{bmatrix}}_{\mathbf{x}_{k+1}} = \underbrace{\begin{bmatrix} 1 & 0 \\ 0 & 1 \end{bmatrix}}_{\mathbf{A}} \underbrace{\begin{bmatrix} i^{\Sigma}_{\alpha}(k) \\ i^{\Sigma}_{\beta}(k) \end{bmatrix}}_{\mathbf{x}_k} + \underbrace{\frac{-T_s}{L} \begin{bmatrix} 1 & 0 \\ 0 & 1 \end{bmatrix}}_{\mathbf{B}} \underbrace{\begin{bmatrix} v^{\Sigma}_{\alpha}(k) \\ v^{\Sigma}_{\beta}(k) \end{bmatrix}}_{\mathbf{u}_k} \tag{2.18}$$

The inner CCS-MPC receives a circulating current reference from the output of the outer CCS-MPC stage [see (2.13)] and minimises the following cost function:

$$\begin{aligned} \min_{\mathbf{x}_{k+1},\mathbf{u}_k} \quad & (\mathbf{x}_{k+1} - \mathbf{x}^*)^T \mathbf{Q} (\mathbf{x}_{k+1} - \mathbf{x}^*) \\ & + (\mathbf{u}_k - \mathbf{u}^*)^T \mathbf{R} (\mathbf{u}_k - \mathbf{u}^*) \\ \text{s.t.} \quad & \mathbf{x}_{k+1} = \mathbf{A}\mathbf{x}_k + \mathbf{B}\mathbf{u}_k \\ & \mathbf{G}\mathbf{u}_k \geq \mathbf{W} \end{aligned} \tag{2.19}$$

where $\mathbf{A}, \mathbf{B}$ and $\mathbf{X}$ are defined in (2.18); $\mathbf{x}^*$ is the reference state which is equal to the circulating current reference $\underline{i}^{\Sigma *}_{\alpha\beta}$, and $\mathbf{u}^*$ is the equilibrium control action that brings the system to $\mathbf{x}^*$. Furthermore, $\mathbf{u}^*$ can be obtained as a function of the reference state by

$$\mathbf{u}^* = \mathbf{B}^{-1}(\mathbf{I} - \mathbf{A})\mathbf{x}^* \tag{2.20}$$

In this case, $\mathbf{u}^*$ is zero considering that $\mathbf{A} = \mathbf{I}$ [see (2.18)]. More details about the resulting equilibrium point are presented in [45]. Simplifying (2.19) by including $\mathbf{x}_{k+1} = \mathbf{A}\mathbf{x}_k + \mathbf{B}\mathbf{u}_k$ in the cost function, yields:

$$\begin{aligned} \min_{\mathbf{u}_k} \quad & \mathbf{u}_k^T \mathbf{H} \mathbf{u}_k + 2 \left[(\mathbf{A}\mathbf{x}_k - \mathbf{x}^*)^T \mathbf{F} \right] \mathbf{u}_k \\ \text{s.t.} \quad & \mathbf{G}\mathbf{u}_k \geq \mathbf{W} \end{aligned} \tag{2.21}$$

where $\mathbf{F}$ and $\mathbf{H}$ are obtained from (2.14).

The diagonal matrices $\mathbf{Q}$ and $\mathbf{R}$ are 2x2, where $\mathbf{Q} = \mathbf{Diag}[\lambda^{\Sigma\prime}_{\alpha}, \lambda^{\Sigma\prime}_{\beta}]$ and $\mathbf{R} = \mathbf{Diag}[\lambda^{U\prime}_{\alpha}, \lambda^{U\prime}_{\beta}]$. As discussed in [45], if the weights of $\mathbf{R}$ are too small, the CCS-MPC algorithm has a fast dynamic response and high sensitivity to noise (i.e similar to a dead-beat response [45]). Using both $\mathbf{Q}$ and $\mathbf{R}$ the CCS-MPC dynamic and steady-state responses can be tailored for a particular application.

Equation (2.21) yields the voltage vector $\underline{v}^{\Sigma}_{\alpha\beta}$ that optimises the cost function. Due to hardware limitations, the voltages synthesised by each cluster [v^P_a, v^P_b, v^P_c, v^N_a, v^N_b and v^N_c]

are bounded between zero up to the maximum voltage achievable without producing over-modulation [v_{Ca}^P, v_{Cb}^P, v_{Cc}^P, v_{Ca}^N, v_{Cb}^N and v_{Cc}^N]. Using the $\Sigma\Delta\alpha\beta 0$ transform, the cluster voltages are obtained as:

$$\begin{bmatrix} v_a^P \\ v_b^P \\ v_c^P \\ v_a^N \\ v_b^N \\ v_c^N \end{bmatrix} = \begin{bmatrix} v_0^\Sigma + \frac{1}{2}v_0^\Delta + \frac{1}{2}v_\alpha^\Delta + v_\alpha^\Sigma \\ v_0^\Sigma + \frac{1}{2}v_0^\Delta - \frac{1}{4}v_\alpha^\Delta - \frac{1}{2}v_\alpha^\Sigma + \frac{\sqrt{3}}{2}v_\beta^\Sigma + \frac{\sqrt{3}}{4}v_\beta^\Delta \\ v_0^\Sigma + \frac{1}{2}v_0^\Delta - \frac{1}{4}v_\alpha^\Delta - \frac{1}{2}v_\alpha^\Sigma - \frac{\sqrt{3}}{2}v_\beta^\Sigma - \frac{\sqrt{3}}{4}v_\beta^\Delta \\ v_0^\Sigma - \frac{1}{2}v_0^\Delta - \frac{1}{2}v_\alpha^\Delta + v_\alpha^\Sigma \\ v_0^\Sigma - \frac{1}{2}v_0^\Delta + \frac{1}{4}v_\alpha^\Delta - \frac{1}{2}v_\alpha^\Sigma + \frac{\sqrt{3}}{2}v_\beta^\Sigma - \frac{\sqrt{3}}{4}v_\beta^\Delta \\ v_0^\Sigma - \frac{1}{2}v_0^\Delta + \frac{1}{4}v_\alpha^\Delta - \frac{1}{2}v_\alpha^\Sigma - \frac{\sqrt{3}}{2}v_\beta^\Sigma + \frac{\sqrt{3}}{4}v_\beta^\Delta \end{bmatrix} \tag{2.22}$$

Considering the upper and lower limits, (2.22) represents 12 constraints. Using symmetries in the voltages v_x^P and v_x^N of phase "x", $\forall\ x \in \{a, b, c\}$ these 12 constraints can be reduced to 6, yielding:

$$\underbrace{\begin{bmatrix} -1 & 0 \\ \frac{1}{2} & -\frac{\sqrt{3}}{2} \\ \frac{1}{2} & \frac{\sqrt{3}}{2} \\ 1 & 0 \\ -\frac{1}{2} & \frac{\sqrt{3}}{2} \\ -\frac{1}{2} & -\frac{\sqrt{3}}{2} \end{bmatrix}}_{\mathbf{G}} \begin{bmatrix} v_\alpha^\Sigma(k) \\ v_\beta^\Sigma(k) \end{bmatrix} \geq \underbrace{\begin{bmatrix} -\min\left(v_1 + v_{Ca}^P(k), v_4 + v_{Ca}^N(k)\right) \\ -\min\left(v_2 + v_{Cb}^P(k), v_5 + v_{Cb}^N(k)\right) \\ -\min\left(v_3 + v_{Cc}^P(k), v_6 + v_{Cc}^N(k)\right) \\ \max\left(v_1, v_4\right) \\ \max\left(v_2, v_5\right) \\ \max\left(v_3, v_6\right) \end{bmatrix}}_{\mathbf{W}} \tag{2.23}$$

where

$$\begin{bmatrix} v_1 \\ v_2 \\ v_3 \\ v_4 \\ v_5 \\ v_6 \end{bmatrix} = \begin{bmatrix} -v_0^\Sigma(k) - \frac{1}{2}v_0^\Delta(k) - \frac{1}{2}v_\alpha^\Delta(k) \\ -v_0^\Sigma(k) - \frac{1}{2}v_0^\Delta(k) + \frac{1}{4}v_\alpha^\Delta(k) - \frac{\sqrt{3}}{4}v_\beta^\Delta(k) \\ -v_0^\Sigma(k) - \frac{1}{2}v_0^\Delta(k) + \frac{1}{4}v_\alpha^\Delta(k) + \frac{\sqrt{3}}{4}v_\beta^\Delta(k) \\ -v_0^\Sigma(k) + \frac{1}{2}v_0^\Delta(k) + \frac{1}{2}v_\alpha^\Delta(k) \\ -v_0^\Sigma(k) + \frac{1}{2}v_0^\Delta(k) - \frac{1}{4}v_\alpha^\Delta(k) + \frac{\sqrt{3}}{4}v_\beta^\Delta(k) \\ -v_0^\Sigma(k) + \frac{1}{2}v_0^\Delta(k) - \frac{1}{4}v_\alpha^\Delta(k) - \frac{\sqrt{3}}{4}v_\beta^\Delta(k) \end{bmatrix} \tag{2.24}$$

Notice that a well-designed MMC has an adequate voltage margin to synthesise $\underline{v}_{\alpha\beta}^\Sigma$ (see [53]); however, in case the control action has a very high dynamic response the constraints of (2.23) are required in (2.21) to avoid over-modulation during transients.

2.4. HIL and Simulation Results

A HIL platform is used in this section to perform work that requires a good repeatability between tests, or tests that could exceed some ratings in the experimental systems.

2.4.1. System Performance and Constraints Operation for Load Changes

Two PLECS-RT Box-1 HIL platforms are employed to model the MMC and the vector-controlled induction machine with a time step of 6.5 μs. The control system is implemented

using a dSPACE MicroLabBox (see more details in Section 2.5). The HIL model utilises the parameters and weights used in the experimental system (see Table 2.1).

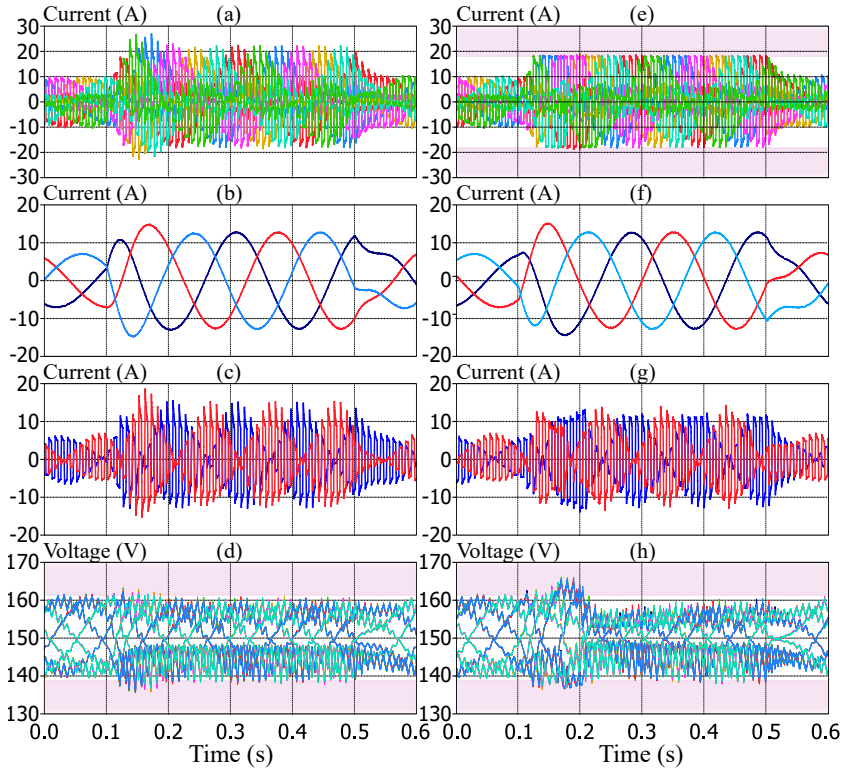

Figure 2.4: HIL results of the saturation limitation of the circulating currents to limit the clusters' currents. Left: without saturation, right: 18 A saturation. (a) and (e) Cluster currents i_a^P, i_b^P, etc. (b) and (f) Machine currents i_a, i_b and i_c. (c) and (g) Circulating currents i_α^Σ and i_β^Σ. (d) and (h) Capacitor voltages v_{Ca1}^P, v_{Ca2}^P, etc.

Two tests were performed for an output frequency of ≈ 4 Hz (≈ 240 rpm). In every test, a predefined maximum limit was used for the arm currents; additionally, for each test, a torque impact between 0 to $\approx 60\,\%$ of the nominal torque is applied to the electrical machine, for 0.1 s $\leq t \leq$ 0.5 s. Note that $v_{Cd}^{\Delta *} = 11.25$ V. Fig. 2.4 shows the experimental results illustrating (from top to bottom) the cluster currents, the machine currents, the circulating currents and the capacitor voltages. The results depicted in Fig. 2.4(a)-(d) correspond to operation without any current constraints. On the other hand Fig. 2.4(e)-(h) shows the performance of the control system for current limits of 18 A. It should be noted that this 18 A limit is arbitrarily selected, to demonstrate the performance of the constraints in the CCS-MPC algorithm, and does not necessarily reflect nominal ratings. Notice that the step torque transient increases the current in the MMC arms, reducing the margin allowed for the circulating currents. For the unconstrained case of Fig. 2.4(a)-(d), the total current in the arms has peaks of ≈ 28 A. However, regulation of the capacitor voltages is very good with all of them maintained well inside the predefined band. Figs 2.4(e)-(h) show the performance of the algorithm when the limit of 18 A is enforced. It is illustrated that the limitation is achieved by reducing the circulating currents $i_{\alpha\beta}^\Sigma$ without affecting the induction machine stator currents. The capacitor voltages are slightly affected by the step change in the torque current, however, after a fast transient, they return to their previous values.

To validate operation with cluster voltage constraints, a trapezoidal v_0 of 202.5 V peak is used; i.e. a relatively high value of v_0 is arbitrarily applied in this test, reducing the voltage margin available for regulating $i_{\alpha\beta}^{\Sigma*}$ and forcing operation with the constraints in (2.21) activated. Fig. 2.5 shows the performance with and without voltage restrictions and with the induction machine operating at 240 rpm ($\approx$ 4 Hz). As before, $v_{Cd}^{\Delta*} = 11.25$ V (see Fig. 2.2) and the torque step transient is imposed for 0.1 s $\leq t \leq$ 0.5 s.

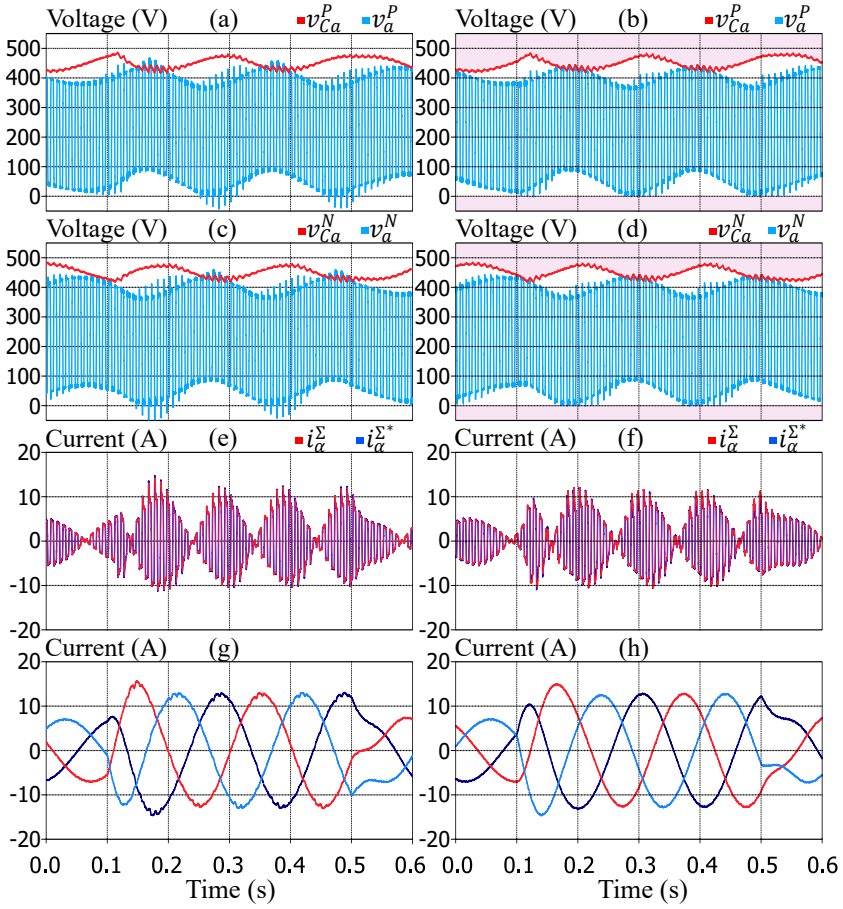

Figure 2.5: HIL results of the clusters output voltages with (right) and without (left) saturation limitation. (a)-(b) Total cluster voltage v_{Ca}^P and cluster output voltage v_a^P, (c)-(d) total cluster voltage v_{Ca}^N and cluster output voltage v_a^N, (e)-(f) circulating current i_α^Σ and its reference $i_\alpha^{\Sigma*}$, (g)-(h) machine currents i_a, i_b and i_c.

From top to bottom, Fig. 2.5 shows the voltages synthesised by leg A, the α-axis circulating current, and the machine currents. Additionally, graphs (a), (b), (c) and (d) include the total cluster voltages in red. Without voltage constraints, the peak voltages synthesised by the arms exceed the total cluster voltages, producing over-modulation and some distortion in the machine currents as shown in Fig. 2.5(g). Conversely, when voltage constraints are included, the voltages synthesised in the arms are limited by the total cluster voltages as shown in Fig. 2.5(b) and Fig. 2.5(d); note that even the low voltage capacitor fluctuations produced in v_{Ca}^{PN} are considered by the inner-CCS algorithm when synthesising the voltages v_a^{PN}. However, the voltage limitations of (2.23), used in the constrained-optimisation problem of (2.19), limit the control effort of the inner CCS-MPC algorithm. Clearly, saturation limitation reduces the tracking performance producing an increased circulating current tracking error ($i_{\alpha\beta}^{\Sigma*} - i_{\alpha\beta}^{\Sigma}$). The

dispersion of the circulating current tracking error increases from $\sigma \approx 0.35$ A (unconstrained case) to $\sigma \approx 0.75$ A (constrained case). Nevertheless, Fig. 2.5(b) and Fig. 2.5(d) show that the capacitor voltages are relatively well regulated, with voltage fluctuations comparable to those obtained for the unconstrained case. When the constraints are enabled, the machine current THD [see Fig. 2.5(h)] is $\approx 0.5\,\%$ whereas, for the case without constraints [see Fig.2.5(g)], the THD increases to $1.8\,\%$ due to over-modulation.

2.4.2. Performance Comparison of Conventional SISO-Based Control System and Proposed two-stage CCS-MPC

The performance of the proposed CCS-MPC is compared to that obtained by the SISO-based control system discussed in [11]. For both cases, it is assumed that the machine stator frequency is 1.7 Hz ($\approx$ 100 rpm). The results are shown in Fig. 2.6 with the CCS-MPC results being shown at the right. The SISO-based control system also includes an allowable capacitor-voltage oscillation band. The same operating conditions and common-mode voltage are used to perform a fair comparison.

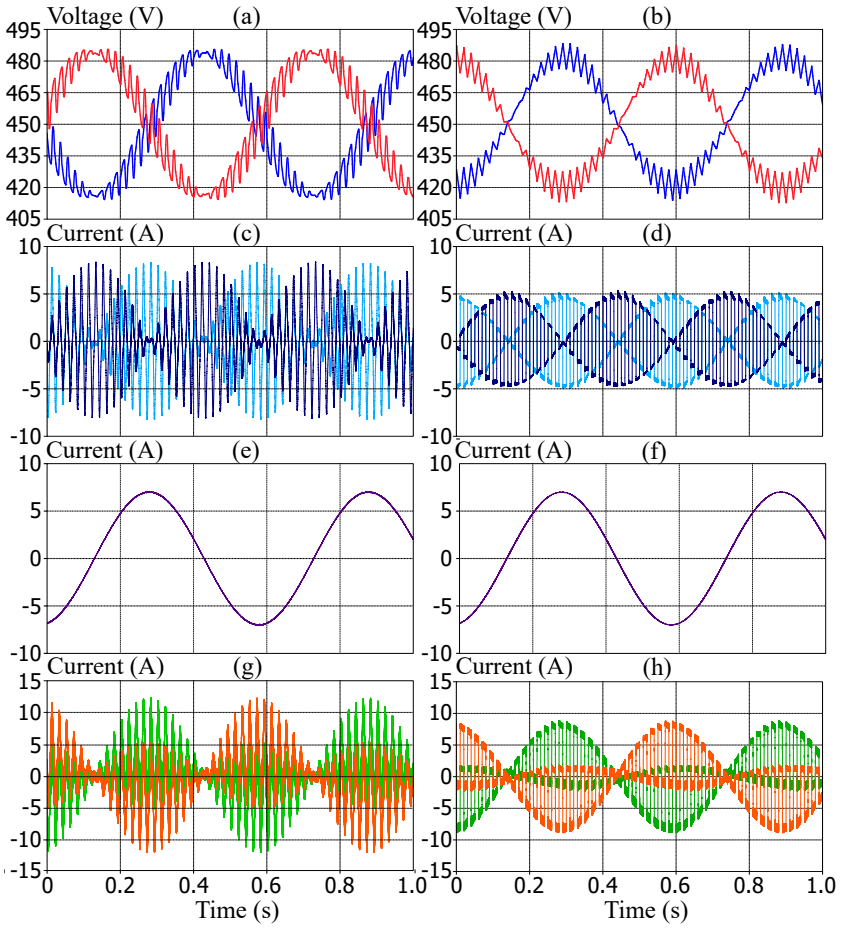

Figure 2.6: MMC static performance at LFM using multiple SISO control loops (left) and proposed two-stage CCS-MPC (right). (a)-(b) Total cluster voltages v_{Ca}^{P} and v_{Ca}^{N}, (c)-(d) Circulating currents i_{α}^{Σ} and i_{β}^{Σ}, (e)-(f) Machine current i_a, (g)-(h) Cluster currents i_a^P and i_a^N.

When analysing Fig. 2.6, the advantages of using the CCS-MPC strategy are clear. The

proposed controller significantly reduces the peak circulating currents at this operating point [see Fig. 2.6(c)-(d)] and also reduces the cluster currents by 30 %. This improvement is due to the much faster dynamic response and higher bandwidth of the predictive controller, and the fact that the shape, frequency, phase and sequence of the circulating currents are automatically and optimally adjusted by the CCS-MPC algorithm of (2.13). According to the results obtained here, the circulating current component, which interacts with v_0 in the term $2v_0\underline{i}^{\Sigma}_{\alpha\beta}$ of (2.7b), has a lower peak than that produced by the SISO implementation proposed in [11] because the CCS-MPC can generate trapezoidal waveforms in the circulating currents allowing for reduced semiconductor current stress. The reduction in the peak circulating currents during LFM could improve the converter efficiency in this operating mode. However, efficiency studies are considered outside the scope of this work. The effects of trapezoidal circulating currents on semiconductor current ratings and capacitor dimensioning are discussed in [40].

As mentioned before, it should be noted that the scheme proposed in [11] does not include globally managed constraints on the circulating currents, unlike the proposed CCS-MPC. Therefore to limit the cluster currents, conventional anti-windup schemes are considered in the SISO-implemented PIs and resonant controllers. Moreover, as stated before, optimal saturation is not simple to achieve in SISO control of MMC. In [11], the circulating currents are regulated by seven independent PI controllers instead of a single MIMO controller. Implementing seven anti-windup schemes to limit the output currents of seven PI controllers leads to sub-optimal solutions (see [16]), compared to those achieved by the CCS-MPC algorithms. This is further discussed in Section 2.1 and demonstrated in [16].

2.5. Experimental Results

Validation of the proposed control scheme is performed using the MMC-based motor drive prototype shown in Fig. 2.7, whose parameters are given in Table 2.1. As mentioned in Section 2.3.1, the weighting factors used in the outer controller are unity (i.e., $\lambda_0^{\Delta} = \lambda_{\alpha}^{\Sigma} = \lambda_{\beta}^{\Sigma} = \lambda_{\alpha}^{U} = \lambda_{\beta}^{U} = 1$) except for $\lambda_{\alpha}^{\Delta}$ and λ_{β}^{Δ}, which are the only ones adjusted by the weighting factor controller (see Section 2.3.2). On the other hand, the weighting factors used in the inner controller are $\lambda_{\alpha}^{\Sigma\prime} = \lambda_{\beta}^{\Sigma\prime} = 1$ and $\lambda_{\alpha}^{U\prime} = \lambda_{\beta}^{U\prime} = 1 \times 10^{-3}$. To control the system, a dSPACE MicroLabBox platform is used, which is composed of a Freescale QorIQ P5020 dual-core 2 GHz processor and a Xilinx Kintex-7 XC7K325T FPGA. In this implementation, the FPGA performs an In-Phase Carrier Disposition (IPD-PWM) modulation scheme and a sorting algorithm. At the same time, the processor executes the optimisations, the active-set solver and the remaining control algorithms. The control platform includes 32 parallel ADCs that are used to simultaneously perform and store all the measurements in FPGA registers.

The MMC drives a 7.5 kW vector-controlled induction machine connected to a permanent magnet synchronous generator (PMSG). A resistor bank has been connected to the PMSG output to provide an electrical load. Hall effect transducers are used to measure the capacitor voltages and cluster currents. A 10, 000 ppr position encoder is fixed to the machine shaft. 18 optical-fibre links transmit the switching signals from the control platform to the gate drivers of the MOSFET switches (model IXFH72N30X3, nominal ratings of 72 A, 300 V, 15 $m\Omega$ On-Resistance). For the 10 kHz switching frequency, a sampling time of 50 μs is used for the implementation of the control algorithms.

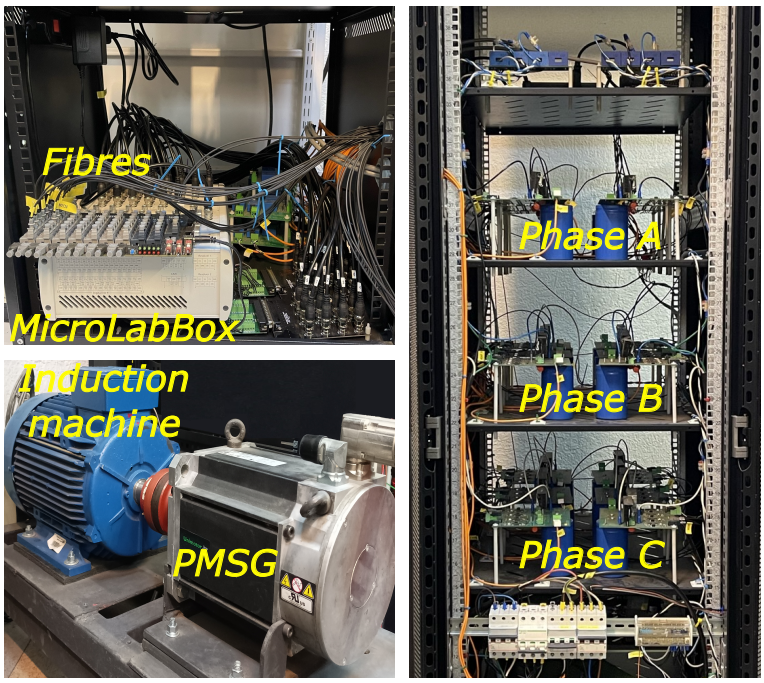

Figure 2.7: Experimental system. At the top left is the dSPACE Microlab-Box connected to an optical-fibre interface board. At the bottom left is the cage machine driving a PMSG. At the right is the 18-cell MMC prototype.

Table 2.1: MMC and Induction machine parameters

Symbol	Parameter	Value	Unit
C	Submodule capacitance	2,200	μF
L	Cluster inductance	2.5	mH
$\overline{v}_C^*$	Submodules DC voltage	150	V
n	Submodules per cluster	3	-
f_s	Carrier frequency	10	kHz
V_{dc}	DC port voltage	450	V
P	Power	7.5	kW
V_m	Machine RMS voltage	380	V
f	Frecuency	50	Hz
p	Pole number	2	-
R_s/R_r	Stator/rotor resistances	367/533	mΩ
$L_s/L_r/L_m$	Stator/Rotor/Mutual inductances	139/139/135	mH

2.5.1. Dynamic Performance of the Control Strategy

Validation of the dynamic performance of the proposed CCS-MPC strategy is tested over a large operating speed range, including operation at standstill ($\omega_e = 0$). Fig. 2.8 shows the experimental results, where a zoom-in on the capacitor voltages and converter currents at LFM and HFM is provided for Figs 2.8(a)-(d). In this test, the different operating regions

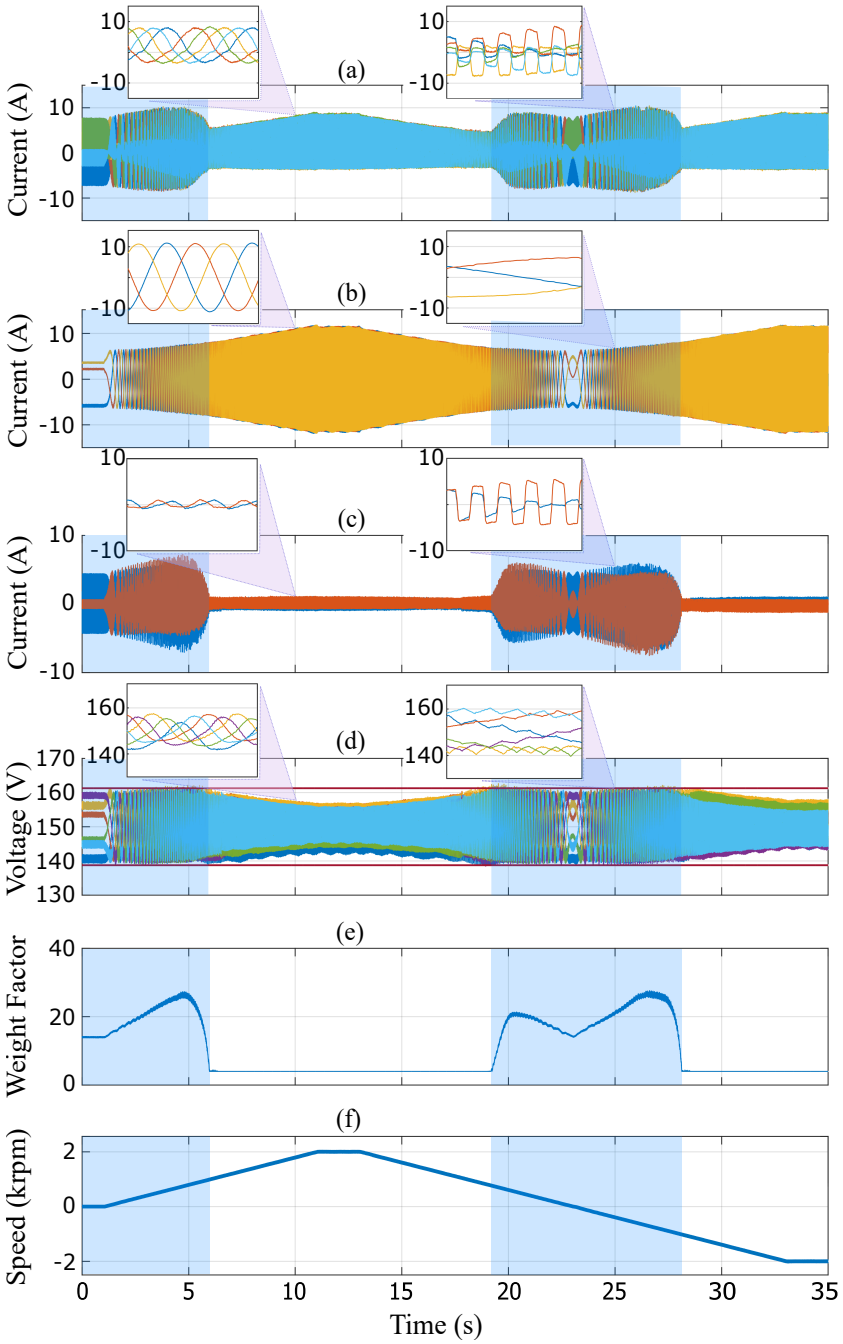

Figure 2.8: System response to a ramp speed variation. (a) Cluster currents i_a^P, i_b^P, etc., (b) Machine currents i_a, i_b and i_c, (c) Circulating currents i_α^Σ and i_β^Σ, (d) Capacitor voltages v_{Ca1}^P, v_{Ca2}^P, etc., (e) Weighting factors λ_α^Δ and λ_β^Δ, and (f) Machine speed ω_r. The zoom-in on the time axis is performed at $t = 10$ s (HFM) and $t = 25$ s (LFM) with a time interval of 50 ms for both cases.

and the behaviour of the system for the LFM-HFM transition can be observed. A tolerance band of $v_{Cd}^{\Delta *} = 11.25$ V (see Fig. 2.2), which represents 7.5 % of the capacitor voltage reference $\overline{v}_C^*$, is used in the variable weight strategy and is illustrated in Fig. 2.8(d) by the red lines. The low-frequency region, where the control strategy operates in LFM, is indicated by a

blue band. As shown in Fig. 2.8(d), the capacitor voltages are maintained inside the 7.5 % tolerance bounds even when the machine operates at a very low frequency during the initial start-up. Notice that during HFM all the capacitor voltages remain well inside the predefined band even when all the $\lambda^{\Delta}_{\alpha\beta}$ are adjusted to the minimum value.

In Fig. 2.8(e) the weighting variations $\lambda^{\Delta}_{\alpha}$ and λ^{Δ}_{β} are analysed. Initially, the weights have a relatively high value because the machine is at standstill with only the magnetising current i_d applied to the stator (i.e. LFM operation with $\omega_e \approx 0$). At $t = 0$, when the torque current is applied, the weighting factors increase [see Figs. 2.8(b) and (e)]. However, when the AC-port frequency is relatively large, the capacitor filtering effect naturally reduces the voltage oscillations. Consequently, the values of the weighting factors [see Fig. 2.8(e)], circulating currents [see Fig. 2.8(c)] and total arm currents [see Fig. 2.8(a)] are also reduced. Moreover, during HFM and in steady state operation (12 s $< t <$ 12.03 s), the THD is only 0.7 %. Regulation of the weighting factors to maintain the capacitor voltages inside a predefined band also allows a seamless transition between LFM and HFM as depicted in Fig. 2.8(e) for $t < 6$ s and between 19.2 s $< t <$ 28.1 s. This is also shown in the scope shot of Fig. 2.9 where an amplified view of the transition between LFM to HFM is depicted. When the weighting factors are reduced from a peak value of ≈ 30 to ≈ 4 the trapezoidal common-mode voltage is eliminated and the HFM mode is enabled.

Notice that the proposed methodology is different to that reported in some previous publications (see [9, 10, 15]), where a stator frequency value (ω_e) is used as a hard limit between LFM and HFM, e.g. $\omega_e = 12$ Hz [9] that is enforced regardless of the magnitudes of the circulating currents and capacitor voltage oscillations. Additionally, the optimal algorithm of (2.13) automatically adjusts all the circulating current parameters to optimise the cost function as shown in Fig. 2.10. The top waveform corresponds to the common mode voltage and the medium and bottom waveforms correspond to the circulating currents i^{Σ}_{α} and i^{Σ}_{β} respectively. Here the machine is operating with a stator frequency of $\approx$ 4 Hz (i.e. LFM operation), and a stator current of 5 A.

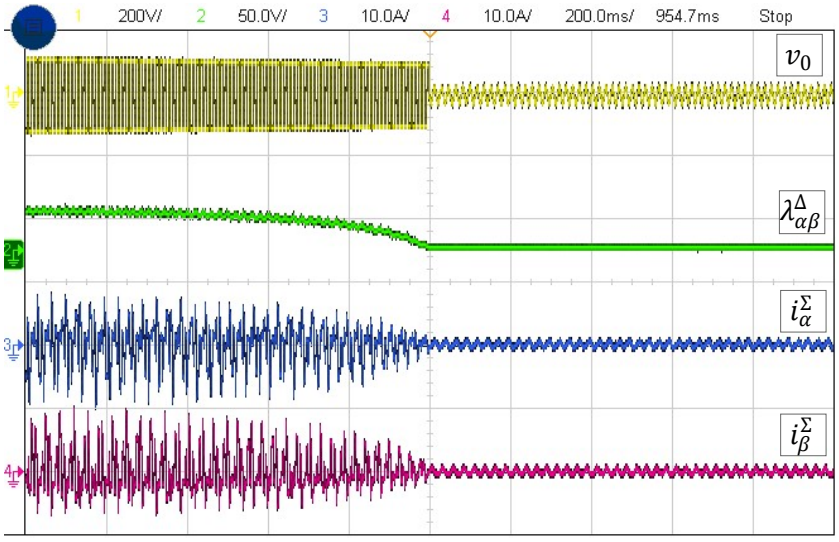

Figure 2.9: Transition region from LFM to HFM. Yellow: common-mode voltage, green: weighting factors, blue and red: circulating currents.

In Fig. 2.10, for $0 \leq t <$ 100 ms a trapezoidal 100 Hz waveform for v_0 is used. This waveform is changed to a 150 Hz sinusoidal waveform by the control algorithm for 100 ms

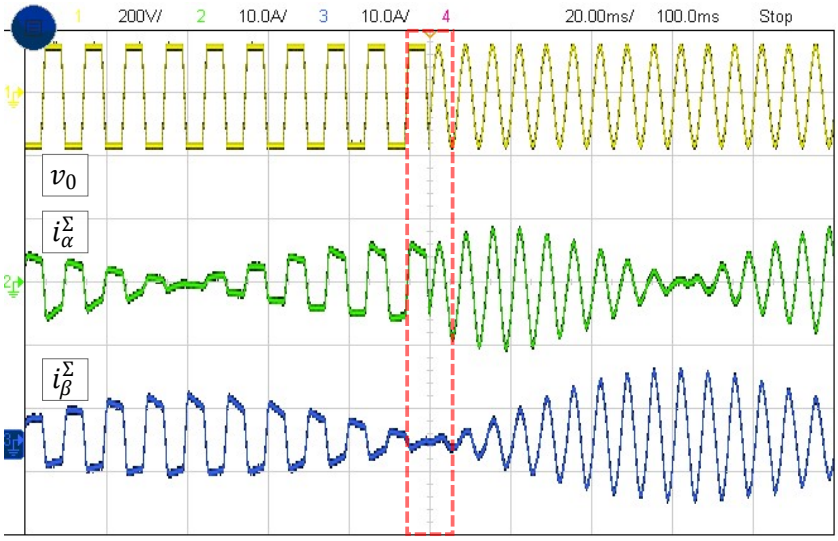

Figure 2.10: Experimental results obtained for an online "on the fly" change of the waveform shape and frequency of the common-mode voltage. Yellow: common-mode voltage, green and blue: circulating currents.

$\leq t \leq 200$ ms. It can be observed that these circulating current components, obtained from (2.19), (2.21), automatically adopt the same phase shift, frequency and waveform shape as the common mode voltage, confirming that predefinition of circulating current parameters is not required in the proposed algorithm. As shown in Fig. 2.10, for a sinusoidal v_0 the circulating current peak value is increased.

Additionally, the execution time was measured during the test shown in Fig. 2.8. This computation time includes the analogue-to-digital conversions and all calculations performed by the QorIQ P5020 processor. The maximum execution time obtained during the test was 15.8 μs, which represents 31.6 % of the total sampling period. Note that the optimisation problems described in Sections 2.3.1 and 2.3.3 do not depend on the number of converter submodules. Therefore, as aforementioned, the computational complexity of the two-stage CCS-MPC does not depend on the number of submodules per cluster, unlike most strategies based on FCS-MPC [4]. In addition, it should be noted that the sorting algorithm can be efficiently implemented in the FPGA taking advantage of its parallel computing capabilities [21]. For example, the modulation and sorting algorithms are executed in less than 10 ns for this implementation. Moreover, to further investigate the computational burden, the conventional SISO strategy proposed in [11] was implemented. The execution time obtained for this control proposal was 14.9 μs. Although the computational burden of the algorithm presented in [11] is lower, this difference is negligible, less than 1 μs, or about 1.8 % of the time period available.

2.6. Conclusions

This paper has presented a two-stage CCS-MPC strategy for regulating the capacitor voltages and the circulating currents of MMC-based drives. As discussed in this paper, saturation of voltages and currents are important tasks which are very difficult to address using conventional linear controllers considering that, in a typical MMC-based drive, each cluster current may have components of several frequencies and positive and negative sequences. However,

saturation of voltages and currents is simple to achieve using the proposed CCS-MPC methodology where the maximum currents allowed in each cluster can be considered as constraints as well as the maximum voltage to be synthesised without producing over-modulation. To solve the intrinsic optimisation problem formulated from the MPC, an Active-Set algorithm, implemented in the dSPACE MicroLabBox, has been integrated into the proposed control methodology.

An important feature of the proposed CCS-MPC is design simplicity because MMC-based drives are MIMO converters. Therefore, designing the control systems using a MIMO-design approach has advantages over the conventional approach of utilising many SISO-designed controllers which are implemented considering simplified models where most of the cross-couplings between the different state variables are neglected. Moreover, for the proposed CCS-MPC algorithm the predefinition of the waveform shape, frequency, electrical sequences, and even phase shifts for the circulating currents are not necessary; all these parameters are automatically obtained when solving the constrained-optimisation methodology proposed in this work. Additionally, the circulating current is optimal and, according to the results obtained in this research effort, for the same common-mode voltage and during LFM operation, the peak values of the circulating currents are usually lower than that obtained using conventional control systems. The effects of the proposed CCS-MPC, on the efficiency achieved at LFM operation, will be addressed in future work.

The experimental results presented in this work show the high performance and good dynamic performance achieved by the proposed two-stage CCS-MPC algorithm for both, LFM and HFM operation. Moreover, a seamless transition between LFM to HFM operation and vice versa has been achieved with the proposed control method.

Chapter 3

A Two-Step Continuous-Control-Set MPC for Modular Multilevel Converters Operating with Variable Output Voltage and Frequency

This chapter is based on the journal paper:

Y. Arias-Esquivel, R. Cárdenas, L. Tarisciotti, M. Díaz, and A. Mora, "A Two-Step Continuous-Control-Set MPC for Modular Multilevel Converters Operating with Variable Output Voltage and Frequency," *IEEE Transactions on Power Electronics*, vol. 38, no. 10, pp. 12091–12103, 2023, doi: 10.1109/TPEL.2023.3288490. Q1 journal paper. Impact Factor: 6.7.

Abstract: This paper presents a new enhanced single-stage two-step Continuous Control Set Model Predictive Control (CCS-MPC) algorithm, for Modular Multilevel Converters (MMCs) operating with variable output frequency at the AC port. The proposed two-step CCS-MPC allows the implementation of feed-forward compensation of the one-step ahead perturbations at the AC side, using an algorithm based on the Moore–Penrose pseudoinverse matrix. Limitations of the current and voltages in the MMC clusters are implemented to avoid overmodulation and overcurrents, being the solution of the constrained CCS-MPC online solved using the active-set method. Without losing generality, the experimental validation of the single-stage CCS-MPC is performed using an 18-cell MMC prototype, driving a 7.5 kW cage induction machine operating in a wide speed range. A dSPACE MicroLabBox platform is used to control the MMC-based drive by implementing the CCS-MPC algorithm, the modulation stage and the active-set method. It is experimentally demonstrated that the compensation of the low-frequency perturbations allows a considerable reduction in the required circulating currents at the low-frequency operation of the drive. Reduction in the capacitor voltage ripple, improved efficiency, and a smaller Total Harmonic Distortion (THD) in the output currents are also achieved with the proposed single-stage two-step CCS-MPC.

3.1. Introduction

Modular multilevel converters have been widely used in medium/high voltage applications due to their prominent features of modularity and scalability [1, 4, 5]. This topology was initially proposed for High-Voltage Direct-Current (HVDC) applications [42, 59]. However, due to its advantages, the applications of MMCs have been extended to low-frequency AC transmission [60], wind-energy systems, variable-speed motor drives [1, 2], etc. Companies such as Siemens and Benshaw offer commercial solutions for MMC-based medium voltage drives: the Sinamics Perfect Harmony GH150 and M2L Series, respectively. The GH150 of Siemens operates in a voltage range from 4 kV to 13.8 kV [35] and the M2L of Benshaw is designed to work in a voltage range from 2.3 kV to 7.2 kV [36]. These converters are typically utilised for compressors, pumps, blowers, fans and other applications related to the oil and gas industry [2]; more information about the commercial solutions for MMC-based drives, already available in the market, is discussed in [2]. One of the possible topologies for an MMC operating with variable output voltage is the MMC-based drive shown in Fig. 3.1, which is composed of a DC port (left-hand side of Fig. 3.1) and an AC port (right-hand side of Fig. 3.1) where the electrical machine is connected.

Although the modularity of the MMC is one of its main advantages, the use of floating capacitors presents an additional control challenge compared to conventional Voltage Source Converters (VSCs). Moreover, the voltages fluctuations in the capacitors are inversely proportional to the operating frequency and proportional to the AC port current [11, 40]. Therefore, two modes of operation are usually defined for the control of MMC-based drives depending on the operating frequency; these modes are the Low-Frequency Mode (LFM) and the High-Frequency Mode (HFM) [9, 10].

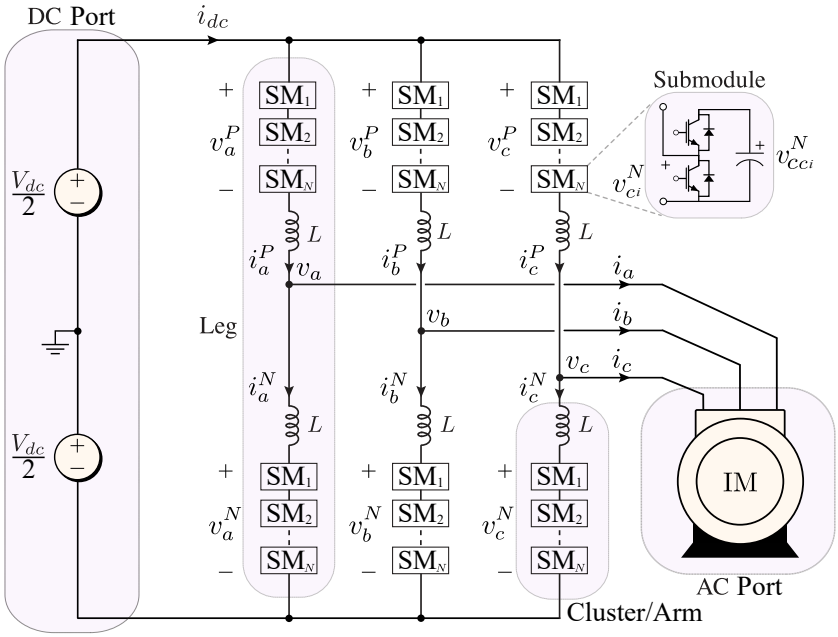

Figure 3.1: Modular Multilevel Converter.

From the control point of view, modular multilevel converters are Multiple-Input Multiple-Output (MIMO) systems [18]. Nevertheless, they are typically controlled assuming Single-Input Single-Output (SISO) control loops [10, 11, 61], which are perfectly decoupled [15, 17,

40]. However, this is an oversimplification, and the control designed using SISO tools produces a suboptimal performance [44, 62, 63]. To improve the control system's performance, MIMO control design techniques have been proposed in [18]. However, with conventional MIMO control systems, handling constraints is not always feasible while it is important for MMC operations [16], for instance, in anti-windup algorithm design.

Recently, Model Predictive Control (MPC) has been proposed as a promising alternative for MMC control [19, 63]. MPC is an ideal multi-variable control method for MIMO systems where constraints can be included in the MPC formulation to ensure that the converter operates within safe operating limits. The most widely used MPC approach in power electronics is Finite Control Set MPC (FCS-MPC), where an external modulation stage is not considered [45, 64]. However, in MMCs, the computational burden of FCS-MPC algorithms grows exponentially with the number of submodules (SMs), making it computationally infeasible [4, 64]. Moreover, the absence of a modulation stage in FCS-MPC produces a variable switching frequency. Conversely, a Continuous Control Set MPC (CCS-MPC) with an external modulator produces a constant switching frequency [48], with a computing burden which is fairly independent of the number of SMs in the converter [19].

There are relatively few publications discussing CCS-MPC algorithms for MMC applications. In [65], the operation of an MMC with variable output frequency is presented and experimentally validated for a CCS-MPC algorithm. However, the dynamics of capacitor voltages are not considered as states but rather as weights in the cost function. This results in a time-variant weight matrix, which is not demonstrated to always be positive semi-definite, as required for a well-defined cost function [45]. In [62], a CCS-MPC algorithm for the control of an MMC driving an induction machine is presented and experimentally validated, considering two separate CCS-MPC algorithms, for the capacitor voltages and circulating current regulations, respectively. However, since the two cost functions are optimised independently, a global optimum is not necessarily achieved by the control system.

In [66], a sequential phase-shifted MPC is presented for MMC driving a RL load at the AC port. In this work, LFM operation at the AC port is not discussed, and currents and voltage restrictions are not considered in the optimisation problem.

This paper proposes an enhanced single-stage CCS-MPC algorithm, where a single cost function is considered to optimally regulate the capacitor voltages and the circulating currents. The proposed algorithm can be used to operate an MMC with variable output frequency, and it is experimentally validated using a prototype composed of an 18-cell MMC driving a 7.5 kW induction machine operating at LFM and HFM. When compared to previous work in the field, the contributions of this work are

- To achieve a single global optimum, a single-stage CCS-MPC is proposed, which combines in a single quadratic cost function capacitor voltages and circulating current regulation. Constant positive semi-definite and positive definite weight matrices are used in the optimal problem, avoiding ill-conditioned cost functions.

- A novel feed-forward disturbance compensation is proposed to reduce the circulating current magnitude at LFM. This algorithm is based on the Moore-Penrose pseudoinverse (see Section 3.3.4) and the input tracking concept [67].

- Unlike most of the previous works in predictive control of MMCs [63, 66, 67], constraints for the capacitor voltages and converter currents, as well as soft constraints, are directly included in the CCS-MPC algorithm (see Appendix 3.1). The constrained optimisation problem is online solved using the active-set method [50].

The rest of this article is organised as follows. In Section 3.2, the model of the MMC is described. The CCS-MPC formulation to regulate the capacitor voltages and circulating currents are provided in Section 3.3. In Section 3.4, experimental work is presented. Finally, Section 3.5 presents the conclusions.

3.2. Mathematical Model of the MMC

Decoupled models of modular multilevel converters have already been published in the literature [10, 12, 68]. For completeness, the model used in this work (based on [10]), is briefly discussed below.

3.2.1. Power-model of the MMC

Referring to Fig.1 and applying Kirchhoff's voltage law, the voltage-current model can be obtained as follows:

$$L\frac{d}{dt}\begin{bmatrix} i_a^P & i_b^P & i_c^P \\ i_a^N & i_b^N & i_c^N \end{bmatrix} = -\begin{bmatrix} v_a^P & v_b^P & v_c^P \\ v_a^N & v_b^N & v_c^N \end{bmatrix} + \frac{V_{dc}}{2}\begin{bmatrix} 1 & 1 & 1 \\ 1 & 1 & 1 \end{bmatrix} + \begin{bmatrix} -v_a & -v_b & -v_c \\ v_a & v_b & v_c \end{bmatrix} \tag{3.1}$$

The power fluctuations in each cluster can be obtained as $p_i^j = v_i^j i_i^j \ \forall \ i \in \{a,b,c\}$ and $j \in \{P,N\}$ (see [12, 13]). If the capacitor voltage oscillations are relatively small, then the capacitor voltages are obtained from (3.2), as:

$$nC\overline{v}_C^*\frac{d}{dt}\begin{bmatrix} v_{Ca}^P & v_{Cb}^P & v_{Cc}^P \\ v_{Ca}^N & v_{Cb}^N & v_{Cc}^N \end{bmatrix} \approx \begin{bmatrix} p_a^P & p_b^P & p_c^P \\ p_a^N & p_b^N & p_c^N \end{bmatrix} \tag{3.2}$$

where $\overline{v}_C^*$ is the DC capacitor voltage reference and v_{Ci}^j are the capacitor voltages.

As shown in (3.1), the converter dynamics are coupled in the natural *abc* frame. In this work, the $\Sigma\Delta\alpha\beta 0$-transformation [10, 12] is used to decouple the state variables dynamics and simplify the MMC control. The transform is defined as:

$$\boldsymbol{X}_{\alpha\beta 0}^{\Sigma\Delta} \doteq \boldsymbol{C}^{\Sigma\Delta} \cdot \boldsymbol{X}_{abc}^{PN} \cdot \boldsymbol{C}_{\alpha\beta 0}^{T} \tag{3.3}$$

where $\boldsymbol{X}_{abc}^{PN}$ is the matrix composed of the *abc*-coordinates variables to be transformed (e.g., cluster currents, capacitor voltages, etc.). The matrices $\boldsymbol{C}^{\Sigma\Delta}$ and $\boldsymbol{C}_{\alpha\beta 0}^{T}$ are defined as:

$$\boldsymbol{C}^{\Sigma\Delta} = \begin{bmatrix} \frac{1}{2} & \frac{1}{2} \\ 1 & -1 \end{bmatrix} \ , \ \boldsymbol{C}_{\alpha\beta 0}^{T} = \begin{bmatrix} \frac{2}{3} & 0 & \frac{1}{3} \\ -\frac{1}{3} & \frac{1}{\sqrt{3}} & \frac{1}{3} \\ -\frac{1}{3} & -\frac{1}{\sqrt{3}} & \frac{1}{3} \end{bmatrix} \tag{3.4}$$

By applying (3.3) to (3.1) the following decoupled model is obtained:

$$\begin{bmatrix} v_\alpha^\Sigma & v_\beta^\Sigma & v_0^\Sigma \\ v_\alpha^\Delta & v_\beta^\Delta & v_0^\Delta \end{bmatrix} = -L\frac{d}{dt}\begin{bmatrix} i_\alpha^\Sigma & i_\beta^\Sigma & \frac{1}{3}i_{dc} \\ i_\alpha & i_\beta & 0 \end{bmatrix} + \frac{V_{dc}}{2}\begin{bmatrix} 0 & 0 & 1 \\ 0 & 0 & 0 \end{bmatrix} - 2\begin{bmatrix} 0 & 0 & 0 \\ v_\alpha & v_\beta & v_0 \end{bmatrix} \tag{3.5}$$

where i_α, i_β, v_α and v_β are the AC port currents and voltages, v_0 is the common-mode voltage, i_{dc} is the DC port current, and i_α^Σ and i_β^Σ are the circulating currents. The voltages on the left-hand side of (3.5) are synthesised by the clusters of the MMC. All these variables are

expressed in $\Sigma\Delta\alpha\beta 0$-coordinates.

The $\Sigma\Delta\alpha\beta 0$-transformation can also be applied to (3.2) to obtain the power-voltage model as follows:

$$nC\overline{v}_C^* \frac{d}{dt} \begin{bmatrix} v_{C\alpha}^{\Sigma} & v_{C\beta}^{\Sigma} & v_{C0}^{\Sigma} \\ v_{C\alpha}^{\Delta} & v_{C\beta}^{\Delta} & v_{C0}^{\Delta} \end{bmatrix} \approx \begin{bmatrix} p_{\alpha}^{\Sigma} & p_{\beta}^{\Sigma} & p_{0}^{\Sigma} \\ p_{\alpha}^{\Delta} & p_{\beta}^{\Delta} & p_{0}^{\Delta} \end{bmatrix} \tag{3.6}$$

After performing some mathematical manipulations (see [10, 12]) and neglecting the voltage drops across cluster inductors, the powers can be expressed as shown in (3.7).

$$p_{\alpha}^{\Delta} = \frac{1}{2}V_{dc}i_{\alpha} - \frac{2}{3}i_{dc}v_{\alpha} - i_{\alpha}^{\Sigma}v_{\alpha} + i_{\beta}^{\Sigma}v_{\beta} - 2i_{\alpha}^{\Sigma}v_0 \tag{3.7a}$$

$$p_{\beta}^{\Delta} = \frac{1}{2}V_{dc}i_{\beta} - \frac{2}{3}i_{dc}v_{\beta} + i_{\beta}^{\Sigma}v_{\alpha} + i_{\alpha}^{\Sigma}v_{\beta} - 2i_{\beta}^{\Sigma}v_0 \tag{3.7b}$$

$$p_{0}^{\Delta} = -i_{\alpha}^{\Sigma}v_{\alpha} - i_{\beta}^{\Sigma}v_{\beta} - \frac{2}{3}i_{dc}v_0 \tag{3.7c}$$

$$p_{\alpha}^{\Sigma} = \frac{1}{2}V_{dc}i_{\alpha}^{\Sigma} - \frac{1}{4}i_{\alpha}v_{\alpha} + \frac{1}{4}i_{\beta}v_{\beta} - \frac{1}{2}i_{\alpha}v_0 \tag{3.7d}$$

$$p_{\beta}^{\Sigma} = \frac{1}{2}V_{dc}i_{\beta}^{\Sigma} + \frac{1}{4}i_{\beta}v_{\alpha} + \frac{1}{4}i_{\alpha}v_{\beta} - \frac{1}{2}i_{\beta}v_0 \tag{3.7e}$$

$$p_{0}^{\Sigma} = \frac{1}{6}V_{dc}i_{dc} - \frac{1}{4}i_{\alpha}v_{\alpha} - \frac{1}{4}i_{\beta}v_{\beta} \tag{3.7f}$$

3.2.2. State equations of the MMC

As shown in (3.6), the relationships between the capacitor voltages can be obtained considering the respective power component. For instance, (3.7)(a) can be rewritten as

$$\frac{dv_{C\alpha}^{\Delta}}{dt} \approx \frac{1}{nC\overline{v}_C^*}\left[\frac{1}{2}V_{dc}i_{\alpha} - \frac{2}{3}i_{dc}v_{\alpha} - i_{\alpha}^{\Sigma}v_{\alpha} + i_{\beta}^{\Sigma}v_{\beta} - 2i_{\alpha}^{\Sigma}v_0\right] \tag{3.8}$$

Inspecting (3.7), it is concluded that five capacitor voltage components can be considered as state variables. Differently, v_{C0}^{Σ}, derived from (3.7)(f), is related to the total energy stored in the capacitors of the converter. Considering that this state variable has a slow dynamic which is not related to the circulating currents, it can be regulated by external PI controllers as shown in Fig. 3.2.

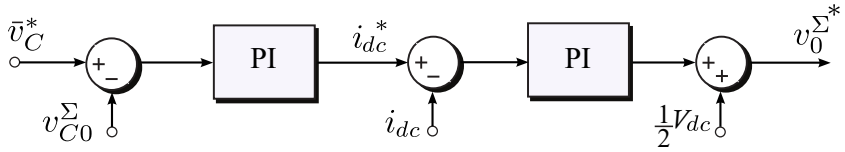

Figure 3.2: DC Port control: capacitor average voltage controller.

The five remaining capacitor voltages derived from (3.7) are decoupled between them and dependent on the circulating currents $\boldsymbol{i}_{\alpha\beta}^{\Sigma} = i_{\alpha}^{\Sigma} + ji_{\beta}^{\Sigma}$, which are also state variables. The state equations of the circulating currents can be derived from (3.5) as

$$\frac{d\boldsymbol{i}_{\alpha\beta}^{\Sigma}}{dt} = \frac{-1}{L} \cdot \boldsymbol{v}_{\alpha\beta}^{\Sigma} \tag{3.9}$$

Finally, the model proposed in this work has seven state variables, i.e. two circulating currents $[i_\alpha^\Sigma \; i_\beta^\Sigma]^T$ [see (3.9)] and five capacitor voltages $[v_{C\alpha}^\Delta \; v_{C\beta}^\Delta \; v_{C0}^\Delta \; v_{C\alpha}^\Sigma \; v_{C\beta}^\Sigma]^T$ [see (3.7)(a)-(e)]. The voltages $v_{\alpha\beta}^\Sigma$ are synthesised by the MMC converter and used to regulate the circulating currents. Notice that for a well-balanced MMC, the five capacitor voltage components, i.e. $v_{C\alpha}^\Delta, v_{C\beta}^\Delta, v_{C0}^\Delta, v_{C\alpha}^\Sigma, v_{C\beta}^\Sigma$ are 0.

In this work, the AC port is separately controlled by an external control law related to the application, e.g., speed control of a mechanical load, using field-orientated control techniques or vector control of a wind generator. Therefore, the AC port output voltages and currents $v_{\alpha\beta}$ and $i_{\alpha\beta}$ are considered as external perturbations in the CCS-MPC algorithm.

Considering the aforementioned state variables and perturbations, the state equations of the MMC in the continuous domain are depicted in (3.10)

$$\dot{\boldsymbol{x}} = \boldsymbol{A}\boldsymbol{x} + \boldsymbol{B}\boldsymbol{u} + \boldsymbol{d} \tag{3.10}$$

where the matrices $\boldsymbol{x}$, $\boldsymbol{A}$, $\boldsymbol{B}$ and $\boldsymbol{u}$ are defined as:

$$\begin{aligned}
\boldsymbol{x} &= \begin{bmatrix} i_\alpha^\Sigma & i_\beta^\Sigma & v_{C\alpha}^\Delta & v_{C\beta}^\Delta & v_{C0}^\Delta & v_{C\alpha}^\Sigma & v_{C\beta}^\Sigma \end{bmatrix}^T \\
\boldsymbol{u} &= \begin{bmatrix} v_\alpha^\Sigma & v_\beta^\Sigma \end{bmatrix}^T \\
\boldsymbol{A} &= \begin{bmatrix} \mathbf{0}_{2\times 2} & \mathbf{0}_{2\times 5} \\ \boldsymbol{B}^v & \mathbf{0}_{5\times 5} \end{bmatrix} \\
\boldsymbol{B} &= \begin{bmatrix} \boldsymbol{B}^i \\ \mathbf{0}_{5\times 2} \end{bmatrix}
\end{aligned} \tag{3.11}$$

The matrix $\boldsymbol{d}$ contains the disturbances or perturbations which can be obtained from (3.7)-(3.9) as shown in (3.12):

$$\boldsymbol{d} = \begin{bmatrix} \mathbf{0}_{2\times 1} \\ \boldsymbol{d}^v \end{bmatrix} \tag{3.12}$$

The sub-matrices $\boldsymbol{B}^v$, $\boldsymbol{B}^i$ and $\boldsymbol{d}^v$ are also obtained from (3.7)-(3.9) as,

$$\boldsymbol{B}^v = \frac{1}{nC\overline{v}_C^*} \begin{bmatrix} -v_\alpha - 2v_0 & v_\beta \\ v_\beta & v_\alpha - 2v_0 \\ -v_\alpha & -v_\beta \\ \frac{V_{dc}}{2} & 0 \\ 0 & \frac{V_{dc}}{2} \end{bmatrix} \tag{3.13}$$

$$\boldsymbol{B}^i = -\frac{1}{L} \begin{bmatrix} 1 & 0 \\ 0 & 1 \end{bmatrix} \tag{3.14}$$

and the matrix with the perturbations $\boldsymbol{d}^v$ is obtained as

$$\boldsymbol{d}^v = \frac{1}{nC\overline{v}_C^*}\begin{bmatrix} \frac{1}{2}V_{dc}i_\alpha - \frac{2}{3}i_{dc}v_\alpha \\ \frac{1}{2}V_{dc}i_\beta - \frac{2}{3}i_{dc}v_\beta \\ -\frac{2}{3}i_{dc}v_0 \\ \frac{1}{4}i_\beta v_\beta - \frac{1}{4}i_\alpha v_\alpha - \frac{1}{2}i_\alpha v_0 \\ \frac{1}{4}i_\beta v_\alpha + \frac{1}{4}i_\alpha v_\beta - \frac{1}{2}i_\beta v_0 \end{bmatrix} \tag{3.15}$$

Notice that the instantaneous power oscillations in the first two rows of (3.15) are very important to compensate during LFM, because the low-frequency voltage and currents may produce large capacitor voltage oscillations [see (3.7)(a)-(3.7)(b)]. Additionally, the matrices $\boldsymbol{B}^v$ and $\boldsymbol{d}^v$ are time variants [see (3.7)] and, for a discrete implementation, their one-step ahead values have to be estimated at each sampling time. Finally, the matrix $\boldsymbol{B}^i$ is time-invariant and obtained from (3.9).

3.2.3. Discrete-time Models

In order to apply the CCS-MPC method to control the capacitor voltage oscillations and circulating currents, a discrete prediction model of these variables is required. Considering the state equations of (3.10) and the matrices and vectors $\boldsymbol{A}$, $\boldsymbol{B}$, $\boldsymbol{x}$ and $\boldsymbol{u}$ of (3.11) some simplifications are possible taking into account the following:

- The only state variables directly dependent on the voltages $\boldsymbol{v}_{\alpha\beta}^{\Sigma}$ are the circulating currents $\boldsymbol{i}_{\alpha\beta}^{\Sigma}$.
- The state variables representing the capacitor voltages $v_{C\alpha}^{\Delta}, v_{C\beta}^{\Delta}, v_{C0}^{\Delta}, v_{C\alpha}^{\Sigma}, v_{C\beta}^{\Sigma}$ are related to the control inputs $\boldsymbol{v}_{\alpha\beta}^{\Sigma}$, through the states representing the circulating currents $\boldsymbol{i}_{\alpha\beta}^{\Sigma}$ [see (3.7)]. Therefore these currents are considered as pseudo 'control inputs' in (3.17).

Therefore, without loss of generality, (3.10) can be rewritten as:

$$\dot{\boldsymbol{x}}^i = \boldsymbol{A}^i\boldsymbol{x}^i + \boldsymbol{B}^i\boldsymbol{u} \tag{3.16}$$

$$\dot{\boldsymbol{x}}^v = \boldsymbol{A}^v\boldsymbol{x}^v + \boldsymbol{B}^v\boldsymbol{x}^i + \boldsymbol{d}^v \tag{3.17}$$

To obtain the discrete-time model of the circulating current dynamics, the forward Euler method is applied to (3.16) with a sampling period of T_s, i.e.:

$$\boldsymbol{x}_{k+1}^i = \boldsymbol{A}_d^i\boldsymbol{x}_k^i + \boldsymbol{B}_k^i\boldsymbol{u}_k^i \tag{3.18}$$

where $\boldsymbol{A}_d^i$ is a 2×2 identity matrix, $\boldsymbol{x}_k^i = [i_\alpha^\Sigma(k)\ i_\beta^\Sigma(k)]^T$, $\boldsymbol{B}_k^i = T_s\boldsymbol{B}^i$ and $\boldsymbol{u}_k^i = [v_\alpha^\Sigma(k)\ v_\beta^\Sigma(k)]^T$. Notice that $\boldsymbol{u}_k^i$ is equal to the k_{th} sample of $\boldsymbol{u}_k$ [see (3.11)], i.e., the $\boldsymbol{v}_{\alpha\beta}^{\Sigma}$ voltages, which are synthesised by the converter.

The discrete-time model of capacitor voltage dynamics is obtained using the forward Euler discretisation method of (3.17), i.e.:

$$\boldsymbol{x}_{k+1}^v \approx \boldsymbol{A}_d^v\boldsymbol{x}_k^v + \boldsymbol{B}_k^v\boldsymbol{x}_k^i + \boldsymbol{d}_k^v \tag{3.19}$$

where A_d^v is a 5×5 identity matrix, $\boldsymbol{B}_k^v = T_s\boldsymbol{B}^v$ and $\boldsymbol{d}_k^v = T_s\boldsymbol{d}^v$. The vectors $\boldsymbol{x}_k^v$ and control input $\boldsymbol{u}_k^v$ are defined as:

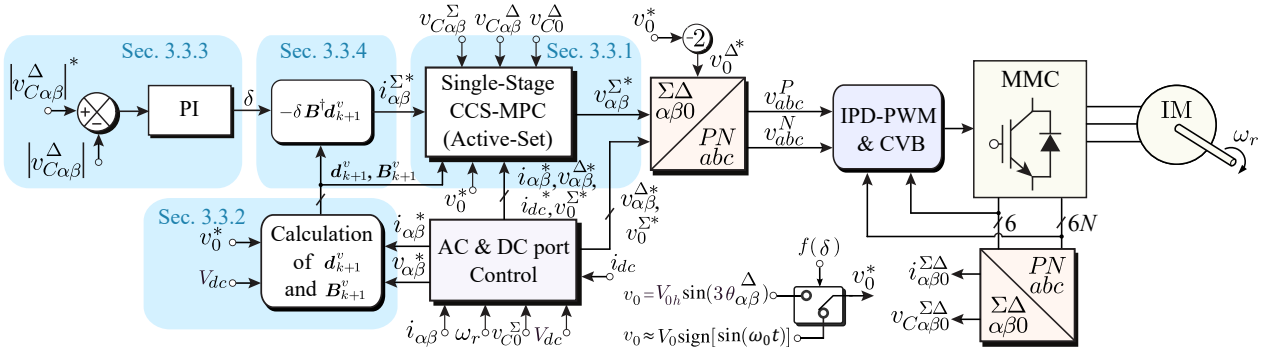

Figure 3.3: Overall Control Scheme for the MMC. The single-stage CCS-MPC is discussed in Section 3.3.1 and utilises an active-set solver. The inputs to the CCS-MPC are the reference currents obtained from the Moore-Penrose-based implementation (discussed in Section 3.3.4). Notice that the band-control system discussed in section 3.3.3, is also required to calculate ${i^{\Sigma}_{\alpha\beta}}^*$. Finally the one-step estimations of $\boldsymbol{d}^v_{k+1}$, $\boldsymbol{B}^v_{k+1}$ and AC/DC port measurements are also required. The common-mode voltage, v_0, is a degree of freedom and typically has a different waveform shape for LFM/HFM operation.

$$\begin{aligned} \boldsymbol{x}^v_k &= \begin{bmatrix} v^{\Delta}_{C\alpha}(k) & v^{\Delta}_{C\beta}(k) & v^{\Delta}_{C0}(k) & v^{\Sigma}_{C\alpha}(k) & v^{\Sigma}_{C\beta}(k) \end{bmatrix}^T \\ \boldsymbol{x}^{\boldsymbol{i}}_{\boldsymbol{k}} &= \boldsymbol{u}^v_k = \begin{bmatrix} i^{\Sigma}_{\alpha}(k) & i^{\Sigma}_{\beta}(k) \end{bmatrix}^T \end{aligned} \tag{3.20}$$

The subscript k denotes discrete-time index in (3.18) and (3.19). Moreover, as aforementioned, the matrices $\boldsymbol{B}^v$ and $\boldsymbol{d}^v$ are time variant, hence $\boldsymbol{B}^v_k \neq \boldsymbol{B}^v_{k+1}$ and $\boldsymbol{d}^v_k \neq \boldsymbol{d}^v_{k+1}$.

3.3. Proposed Continuous Control Set Model Predictive Control

The proposed control system is shown in Fig. 3.3. The use of the PI controller depicted in the left-hand side of the diagram is discussed in Section 3.3.3. The single-stage MPC algorithm is discussed below.

3.3.1. Single-Stage CCS-MPC

To regulate the capacitor voltage fluctuation, a single-stage CCS-MPC is proposed in this paper. This CCS-MPC algorithm combines the circulating currents, capacitor voltage prediction models and restrictions in a single optimisation problem. However, the standard cost function, which is typically based on a single-step prediction algorithm [45, 62, 65], cannot be used in this application because there is not a cause-effect relationship between the capacitor voltage vector $\boldsymbol{x}^v_{k+1}$ and the voltages $\boldsymbol{u}_k = [v^{\Sigma}_{\alpha}(k)\ v^{\Sigma}_{\beta}(k)]^T$ synthesised by the converter. In fact, according to (3.19), the capacitor voltages $\boldsymbol{x}^v_{k+1}$ are already established in the k_{th} time step.

The lack of causality between $\boldsymbol{u}^v_k$ and $\boldsymbol{x}^v_{k+1}$ can be solved using a two-step algorithm for the prediction of the capacitor voltages. Hence, for the proposed single-stage CCS-MPC algorithm, the following cost function is proposed:

$$\min_{\boldsymbol{x}^v_{k+2},\boldsymbol{x}^i_{k+1},\boldsymbol{u}_k,\xi} \quad J = {\boldsymbol{x}^v_{k+2}}^T \boldsymbol{Q}^v \boldsymbol{x}^v_{k+2} \tag{3.21a}$$

$$+ \left(\boldsymbol{x}^i_{k+1} - \boldsymbol{x}^*\right)^T \boldsymbol{Q}^i \left(\boldsymbol{x}^i_{k+1} - \boldsymbol{x}^*\right) \tag{3.21b}$$

$$+ {\boldsymbol{u}_k}^T \boldsymbol{R} \boldsymbol{u}_k + {\xi}^T \lambda^\xi \xi \tag{3.21c}$$

$$\text{s.t.} \quad \boldsymbol{x}^v_{k+2} = \boldsymbol{x}^v_{k+1} + \boldsymbol{B}^v_{k+1} \boldsymbol{x}^i_{k+1} + \boldsymbol{d}^v_{k+1} \tag{3.21d}$$

$$\boldsymbol{x}^i_{k+1} = \boldsymbol{x}^i_k + \boldsymbol{B}^i_k \boldsymbol{u}_k \tag{3.21e}$$

$$\boldsymbol{G}^v \boldsymbol{x}^i_{k+1} \geq \boldsymbol{W}^v - \mathbf{1}^T \xi \tag{3.21f}$$

$$\boldsymbol{G}^i \boldsymbol{u}_k \geq \boldsymbol{W}^i \tag{3.21g}$$

$$\xi \geq 0 \tag{3.21h}$$

In (3.21), superscripts i and v are used to identify the matrices and vectors corresponding to (3.16)-(3.17) respectively. Moreover, as aforementioned, in this formulation vectors $\boldsymbol{u}^v_k$ and $\boldsymbol{x}^i_k$ denote the same variables. Finally, the formulation of the optimisation problem, shown in (3.21), has been simplified by considering that $\boldsymbol{A}^i_d$ and $\boldsymbol{A}^v_d$ are identity matrices.

The first term in the cost function [see (3.21)(a)] is used to penalise the capacitor voltage oscillations at the $(k+2)_{th}$ time step. The second term [see (3.21)(b)] penalises the tracking error of the circulating currents at the $(k+1)_{th}$ time step. Appropriate references of the circulating currents ($\boldsymbol{x}^*$) have to be computed to compensate for the disturbance vector $\boldsymbol{d}^v_{k+1}$. This is further discussed in Section 3.3.4.

The third term at the left-hand side of (3.21)(c) penalises the control actions. Finally, the fourth term of the cost function, at the right of (3.21)(c), penalises the slack variable (ξ) used for softening state constraints. As discussed in several publications, soft constraints are usually utilised in CCS-MPC algorithms for avoiding feasibility issues which can be produced, among other things, by modelling errors and incorrect initialisation of the states [44, 56, 69, 70]. In this work, only one slack variable (ξ) is used for softening the six current constraints. The weighting matrices are diagonal and defined as shown in (3.22),

$$\begin{aligned} \boldsymbol{Q}^v &= diag(\lambda^{\Delta v}_\alpha, \lambda^{\Delta v}_\beta, \lambda^{\Delta v}_0, \lambda^{\Sigma v}_\alpha, \lambda^{\Sigma v}_\beta) \\ \boldsymbol{Q}^i &= diag(\lambda^{\Sigma i}_\alpha, \lambda^{\Sigma i}_\beta) \\ \boldsymbol{R} &= diag(\lambda^{U}_\alpha, \lambda^{U}_\beta) \end{aligned} \tag{3.22}$$

where the $\boldsymbol{Q}$ matrices are positive semi-definite and the $\boldsymbol{R}$ matrix is positive definite. Additionally, $\lambda^{\Delta v}_\alpha, \lambda^{\Delta v}_\beta$, etc., are the weighting factors of the states and control actions, and λ^ξ is the weighting factor of the slack variable. As aforementioned, for the proposed algorithm the weight matrices are constant and not modified according to the AC port operating frequency. Constraints are used to limit the circulating voltages and currents depending on the voltages and currents available in the converter clusters. The constraints imposed on the circulating currents ($i^\Sigma_\alpha, i^\Sigma_\beta$) and control actions ($v^\Sigma_\alpha, v^\Sigma_\beta$) are represented by $\boldsymbol{G}^v$, $\boldsymbol{W}^v$ and $\boldsymbol{G}^i$, $\boldsymbol{W}^i$ [see (3.21)(f) and (3.21)(g)] respectively. These matrices are fully discussed in Appendix 3.1.

In this work, the weighting factors in the matrices $\boldsymbol{Q}^v$, $\boldsymbol{Q}^i$, and $\boldsymbol{R}$ are adjusted using the branch and bound algorithm (refer to [71]). This algorithm enables the rejection of weight factors that do not produce satisfactory performance. The effectiveness of the controller is

assessed by measuring the deviation of the capacitor voltages within the allowable oscillation range and the magnitudes of the circulating currents. Specifically, the weights in the matrices $\boldsymbol{Q}^i$ and $\boldsymbol{R}$ are adjusted to ensure adequate tracking of the reference signal $\boldsymbol{x}^*$, whereas the weights in the $\boldsymbol{Q}^v$ matrix are adjusted to maintain well-regulated voltage oscillations around the reference voltage $\overline{v}_C^*$.

The optimisation problem of (3.21) can be simplified by substituting the voltage equality constraints [see (3.21)(d)] and the current equality constraints [see (3.21)(e)] into the cost function; i.e. in equations (3.21)(a)-(3.21)(c) and equations (3.21)(f)-(3.21)(g)]. After performing the substitutions and considering some algebraic manipulations, the cost function of (3.21) can be written in the compact form shown in (3.23),

$$\begin{aligned} \min_{\boldsymbol{u}_k^i} \quad & \frac{1}{2}{\boldsymbol{u}_k^i}^T \boldsymbol{H} \boldsymbol{u}_k^i + \boldsymbol{c}^T \boldsymbol{u}_k^i + \xi^T \lambda^\xi \xi \\ \text{s.t.} \quad & \boldsymbol{G}^v \boldsymbol{B}_k^i \boldsymbol{u}_k^i \geq \boldsymbol{W}^v - \boldsymbol{G}^v \boldsymbol{x}_k^i - \boldsymbol{1}^T \xi \\ & \boldsymbol{G}^i \boldsymbol{u}_k^i \geq \boldsymbol{W}^i \\ & \xi \geq 0 \end{aligned} \tag{3.23}$$

with

$$\begin{aligned} \boldsymbol{M} &= \left({\boldsymbol{B}_{k+1}^v}^T \boldsymbol{Q}^v \boldsymbol{B}_{k+1}^v + \boldsymbol{Q}^i\right) \boldsymbol{B}_k^i \\ \boldsymbol{F} &= \boldsymbol{Q}^v \boldsymbol{B}_{k+1}^v \boldsymbol{B}_k^i \\ \boldsymbol{H} &= {\boldsymbol{B}^i}^T \boldsymbol{M} + \boldsymbol{R} \\ \boldsymbol{c}^T &= \boldsymbol{M}^T \boldsymbol{x}_k^i + \boldsymbol{F}^T \left(\boldsymbol{x}_{k+1}^v + \boldsymbol{d}_{k+1}^v\right) - {\boldsymbol{B}_k^i}^T {\boldsymbol{Q}^i}^T \boldsymbol{x}^* \end{aligned} \tag{3.24}$$

Equation (3.24) can be further simplified by replacing the vector $\boldsymbol{x}_{k+1}^v$ using (3.19). The prediction of $\boldsymbol{B}_{k+1}^v$ and $\boldsymbol{d}_{k+1}^v$ is also required in (3.24).

3.3.2. Prediction of the Variables Considered in $\boldsymbol{B}_{k+1}^v$ and $\boldsymbol{d}_{k+1}^v$

The time variant matrix $\boldsymbol{B}^v$ is shown in (3.13). Notice that the voltages v_α and v_β are external and depend on the operating point of the AC-output port. These voltages are simple to predict by considering that the voltage magnitude is constant for the next sampling time as shown in (3.25), i.e.:

$$v_\alpha(k+1) + j v_\beta(k+1) = [v_\alpha(k) + j v_\beta(k)] \cdot e^{j\Delta\theta_e} \tag{3.25}$$

where $\Delta\theta_e$ is the one-sample variation of the output electrical angle. This compensation is more important at HFM operation where the output frequency ω_e is higher. Furthermore, $v_0(k+1)$ is known because it is a degree of freedom imposed by the control system. Under these assumptions and considering constant DC port voltage, an estimation of the matrix $\boldsymbol{B}_{k+1}^v$ is obtained.

Regarding the disturbance vector $\boldsymbol{d}^v$, after inspecting (3.15) it is concluded that the estimation of $\boldsymbol{d}_{k+1}^v$ could require to predict the values of the machine currents. However, the impact of the perturbation vector is more critical at LFM operation, where the low-frequency oscillations produced in the first two rows of $\boldsymbol{d}^v$ are difficult to compensate and the variation

of the output current is slow. During HFM operation, the effect of $\boldsymbol{d}^v$ is smaller because it is naturally filtered out by the MMC capacitors.

The performance of the proposed CCS-MPC algorithm can be improved if the estimation of the future disturbance vector $\boldsymbol{d}^v_{k+1}$ is used to obtain the value of $\boldsymbol{x}^*$ of (3.21)(b). This is discussed in Section 3.3.4.

3.3.3. Handling of the Disturbance Vector $\boldsymbol{d}^v$ with Capacitor Voltage Band-Control

By inspecting (3.19) it is concluded that in the absence of circulating currents, the capacitor voltage fluctuations are dependent on the disturbance vector $\boldsymbol{d}^v_k$. Moreover, as discussed in several publications (see [10, 12, 62]), the two first rows of (3.15) may produce capacitor voltage oscillations of high amplitude during LFM operation [9, 11]. Therefore, during LFM, large circulating currents are required if the voltage fluctuations, particularly in the $\boldsymbol{v}^{\Delta}_{C\alpha\beta}$ voltage components [see (3.7)(a)-(b) and [11]] are overcompensated by the control system (see [11, 40]). Nevertheless, regulating the capacitor voltage oscillations to $\approx$ zero is not mandatory since, as reported in the literature, the MMC can operate appropriately if restricted capacitor voltage fluctuations are permitted. For instance allowing voltage oscillations in a band of $\approx \pm 5\,\%$ to $\pm 10\,\%$ around the reference voltage $\overline{v}^*_C$ [9, 11].

This work proposes a simple PI controller to adjust the magnitude of the compensation vector ($\boldsymbol{x}^*$) of (3.21)(b) using a gain δ [see left-hand side of Fig. 3.3 and (3.28)]. The reference to this control system is the maximum magnitude of the oscillating cluster voltages $\boldsymbol{v}^{\Delta\,*}_{C\alpha\beta}$ (see[11]) allowed in the converter at LFM operation. To tune this controller, the dynamic of the $\boldsymbol{v}^{\Delta}_{C\alpha\beta}$ component of the capacitor voltage is considered, and this is thoughtfully discussed and analysed in [11]. Considering the modelling discussed in that publication and using simulation and experimental work, it is relatively simple to tune the controller. Finally, in this work, experimental current steps, as shown in Fig. 3.6, have been used to assess the dynamic response.

Using the aforementioned methodology, the speed of the $|\boldsymbol{v}^{\Delta}_{C\alpha\beta}|$ controller was adjusted until a good dynamic response was obtained in all the operating ranges. Notice that when the output frequency ω_e increases, then the voltage oscillations $\boldsymbol{v}^{\Delta}_{C\alpha\beta}$ decrease due to the filtering action of the capacitors. Hence, the circulating currents are naturally reduced, allowing a simple and seamless transition between HFM to LFM and vice-versa.

3.3.4. Feed-Forward Compensation of the future Disturbance Vector $\boldsymbol{d}^v_{k+1}$

One of the important features of the two-step CCS-MPC algorithm, proposed in this work, is to predict the reference of the circulating current vector $\boldsymbol{i}^{\Sigma*}_{\alpha\beta}$, which will be required in the next sampling time [i.e. the $(k+1)_{th}$ time step] to compensate the variations in the time-variant vector $\boldsymbol{d}^v$. This reference is obtained by assuming that the single-step prediction of the capacitor voltage oscillations is negligible around $\overline{v}^*_C$ (i.e. $\boldsymbol{x}^v_{k+1} \approx \boldsymbol{0}_{5\times 2}$) and it is required to maintain this value for the next step. Therefore, from (3.19), the following expression is obtained:

$$\boldsymbol{0}_{5\times 2} \approx \boldsymbol{B}^v_{k+1}\boldsymbol{x}^{i*}_{k+1} + \boldsymbol{d}^v_{k+1} \tag{3.26}$$

from (3.26) the following is concluded:

$$\left[i_{\alpha}^{\Sigma*}(k+1)\ i_{\beta}^{\Sigma*}(k+1)\right]^{T} = -\left(\boldsymbol{B}_{k+1}^{v}\right)^{-1}\boldsymbol{d}_{k+1}^{v} \tag{3.27}$$

However, $\boldsymbol{B}^{v}$ is a 5×2 non-invertible matrix. Therefore, a Moore–Penrose pseudoinverse matrix is used in this work to calculate $\left[\boldsymbol{B}_{k+1}^{v}\right]^{-1}$. To maintain the capacitor voltages inside a predefined band, the vector of circulating current references is calculated as

$$\left[i_{\alpha}^{\Sigma*}(k+1)\ i_{\beta}^{\Sigma*}(k+1)\right]^{T} = -\delta\boldsymbol{B}^{\dagger}\boldsymbol{d}_{k+1}^{v} \tag{3.28}$$

where $\boldsymbol{B}^{\dagger}$ is the Moore–Penrose pseudoinverse of $\boldsymbol{B}_{k+1}^{v}$, namely, $\boldsymbol{B}^{\dagger} = (\boldsymbol{B}_{k+1}^{vT}\boldsymbol{B}_{k+1}^{v})^{-1}\boldsymbol{B}_{k+1}^{vT}$ and δ is the output of the PI controller regulating the capacitor voltage oscillations inside a predefined band (see Fig. 3.3).

The control methodologies discussed in Sections 3.3.3 and 3.3.4 allow to operate the proposed CCS-MPC without using variable weight matrices in the cost function of (3.21). Previous work in the control of MMC operating in the LFM mode (e.g. see [16, 62, 63]) compensated the capacitor voltage oscillations during HFM by increasing the weight factors. This methodology is effective but has the disadvantage of increasing the high-frequency ripple in the circulating currents and voltages synthesised by the converter.

In summary, the advantages of the one-step ahead feed-forward compensation of the disturbance vector discussed in this section, compared to the adjustable-weight method, are at least three. i) The circulating currents are noticeably reduced at LFM, particularly at steady-state operation. ii) The high-frequency ripple in the capacitor voltages is also reduced, and iii) fast and large variations in the voltage $\boldsymbol{v}_{\alpha\beta}^{\Sigma}$ are avoided reducing the effects of the voltage restrictions used in (3.21)-(3.23).

3.4. Experimental Results

The validation of the proposed CCS-MPC is discussed in this section. In the first subsection, the performance of the proposed control system is compared with that obtained by the adjustable-weight CCS-MPC algorithm discussed in [62] in terms of the magnitude of the circulating currents, THD obtained at the output, etc. In the second subsection, a cage induction machine is connected to the MMC outputs to verify the performance of the proposed control algorithm operating with variable frequency and voltage at the AC port.

The parameters of the experimental system are shown in Table 3.1. The MMC is composed of 18 cells controlled using a dSPACE MicroLabBox platform based on a Freescale QorIQ P5020 dual-core 2 GHz processor and a Xilinx Kintex-7 XC7K325T FPGA. The FPGA performs a modulation scheme based on an In-Phase Carrier Disposition (IPD-PWM) augmented by a sorting algorithm. Meanwhile, the dSPACE processor is used to implement the active-set solver, $\Sigma\Delta\alpha\beta0$ direct and inverse transforms, control algorithms, etc. The control platform includes 32 parallel ADCs that are used to simultaneously perform the measurements.

To verify the performance of the MMC regulating variable frequency and voltage at the AC port, a 7.5 kW vector-controlled induction machine, connected to a permanent magnet synchronous generator (PMSG), is utilised. The experimental system is shown in Fig. 3.4.

A bank of resistors is used to provide an electric load at the output of the PMSG, and Hall effect transducers are used to measure the capacitor voltages and cluster currents. Optical-fibre links are used to transmit the switching signals from the control platform to the gate

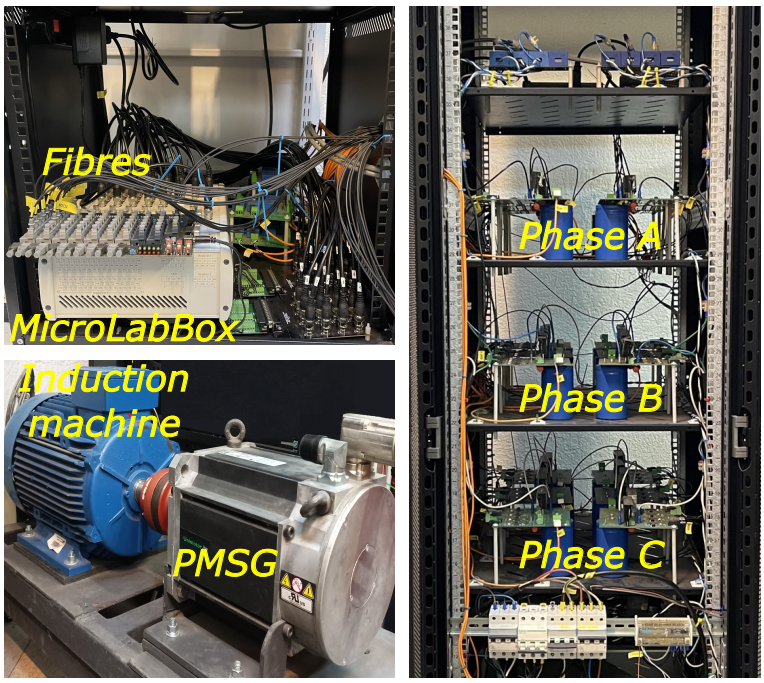

Figure 3.4: Experimental system. At the top left is the dSPACE Microlab-Box connected to an optical-fibre interface board. At the bottom left is the cage machine driving a PMSG. At the right is the 18-cell MMC prototype.

drivers of the MOSFET switches (model IXFH72N30X3, nominal ratings of 72 A, 300 V, 19 $m\Omega$ On-Resistance). For the 10 kHz switching frequency, a sampling time of 50 μs is used for the implementation of the control algorithms. Finally, unless otherwise stated, the common-mode voltage is a square waveform of $\omega_0 = 200$ Hz and a magnetising current of $i_{sd} = 7$ A is utilised in the cage machine.

3.4.1. Performance of the Proposed CCS-MPC Compared to that Obtained in a Previous Work

The performance of the proposed control algorithm operating with low output frequency is experimentally compared with that obtained with the CCS-MPC algorithm reported in [62]. The experimental results obtained with the proposed two-step CCS-MPC algorithm are shown on the two graphics at the left-hand side of Fig. 3.5. Conversely, the results obtained with the adjustable-weight algorithm of [62] are depicted on the right-hand side. Notice that the proposed CCS-MPC algorithm reduces the effective values of the circulating currents from 5.14 A to 3.15 A [see Figs.3.5(c)-(i) respectively] for the same low-frequency perturbation power vector. The reduction in the circulating current magnitudes is significant at this operating point ($\approx 40\,\%$), and it is mainly produced by the feed-forward compensation of the low-frequency power perturbation (see Section 3.3.4), using the values of $[i_{\alpha}^{\Sigma *}(k+1)\ i_{\beta}^{\Sigma *}(k+1)]^T$ calculated from (3.28). Moreover, the control system presented in [62] is based on solving two quadratic cost functions and the global optimum is not necessarily achieved. Conversely, a single-stage control function is performed in the proposed CCS-MPC and a single global optimum is obtained. Notice also the substantial reduction in the high frequency (200 Hz) ripple in the capacitor voltages, as shown in Figs. 3.5(a)-(g). From Figs. 3.5(d)-(j) can be appreciated that the predictive control algorithm proposed in this work

Table 3.1: Induction machine, MMC and CCS-MPC parameters

Description	Variable	Value
Rated output power	P	7.5 kW
Line-to-line RMS voltage	V_m	380 V
Rated frequency	f	50 Hz
Pole number	p	2
Stator/Rotor resistances	R_s/R_r	367/533 mΩ
Stator/Rotor inductances	L_s/L_r	139/139 mH
Mutual inductance	L_m	135 mH
Number of SMs per cluster	n	3
Cluster inductance	L	2.5 mH
SM capacitance	C	2.2 mF
SM DC voltage	$\overline{v}_C^*$	150 V
DC port voltage	V_{dc}	450 V
Carrier frequency	f_s	10 kHz
Weighting factors ($\boldsymbol{Q}^v$)	$\lambda_\alpha^{\Delta v}/\lambda_\beta^{\Delta v}/\lambda_0^{\Delta v}/\lambda_\alpha^{\Sigma v}/\lambda_\beta^{\Sigma v}$	5/5/10/10/10
Weighting factors ($\boldsymbol{Q}^i$)	$\lambda_\alpha^{\Sigma i}/\lambda_\beta^{\Sigma i}$	1/1
Weighting factors ($\boldsymbol{R}$)	$\lambda_\alpha^{U}/\lambda_\beta^{U}$	0.001/0.001
Weighting factor (slack)	λ^{ξ}	100,000

achieves a THD reduction of $\approx 1\,\%$ (in the AC currents) compared to the one obtained by the adjustable-weight CCS-MPC algorithm discussed in [62], thanks to the capacitor voltage ripple reduction. Additionally, using (3.28) a reduction in the amplitude variation of the voltages $\boldsymbol{u}_k = [v_\alpha^\Sigma(k)\ v_\beta^\Sigma(k)]^T$ synthesised by the converter is produced which increases the voltage margin available in the MMC.

As aforementioned, the reduction in the THD of the AC currents is an advantage of the proposed CCS-MPC. However, the proposed CCS-MP also delivers improved efficiency. To evaluate the power losses, a Hioki PW6001 power analyser has been used to perform power measurements for both control strategies. The measurements are obtained using the operating conditions described in Fig. 5, i.e. AC frequency of 10 Hz, $\omega_r = 600$ rpm, machine currents $i_{sd} = 7$ A and $i_{sq} \approx 7.1$ A. The experimental measurements are shown in Table 3.2 with the proposed CCS-MPC strategy delivering a 7.5 % of improvement in the converter efficiency, compared to the strategy reported in [62].

Notice that the efficiency values shown in Table 3.2 consider all the losses, e.g. switching/conducting losses in the MOSFETs, the losses in the parasitic resistances of the six cluster inductors ($\approx 0.1\Omega$ each) and also iron losses in the inductor cores. Because the proposed CCS-MPC reduces the effective currents in the clusters (by reducing the circulating currents) the losses in the parasitic resistances are also reduced.

To estimate only the switching and conduction losses of the 36 MOSFET switches used in the experimental system, the methodology discussed in [72] was implemented in a PLECS model and simulated for the same operating point discussed above. For the control strategy reported in [62] the total losses, in the 18 half-bridge cells, were 147.6 W meanwhile the losses for the proposed algorithm were 97.2 W. Therefore the two-step CCS-MPC algorithm

produces a reduction in switching/conduction losses of ≈ 34.1 %. These results are in broad agreement with the experimental results discussed above.

Table 3.2: Efficiency Comparison of Power Loss Measurements for Control Strategies using Hioki PW6001 Power Analyser

	Adjustable-weight CCS-MPC [62]	Proposed CCS-MPC
Input power	893.7 W	812.7 W
Output power	684.9 W	683.8 W
Total power loss	208.9 W	128.9 W
Efficiency	76.63 %	84.14 %
AC port frequency	10.3 Hz	10.3 Hz

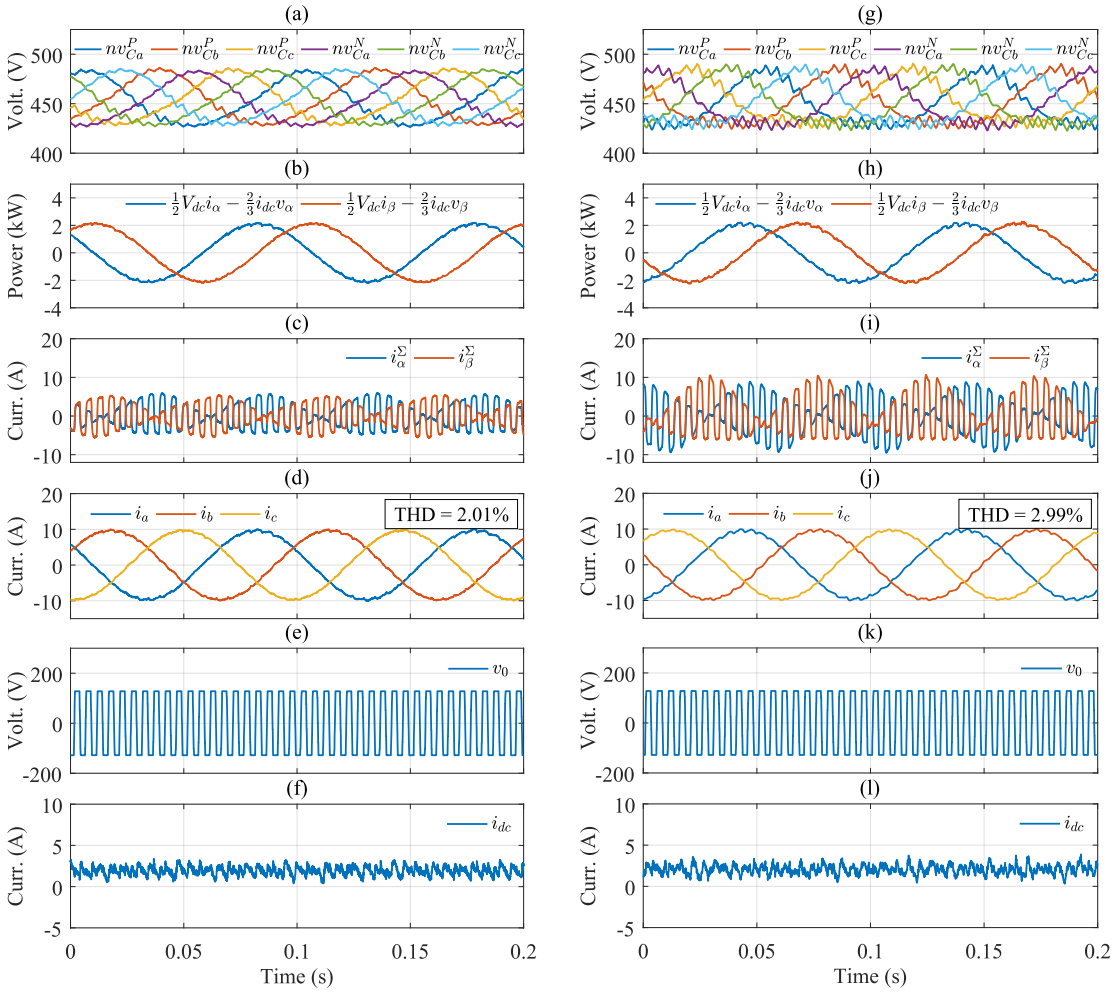

Figure 3.5: Steady state performance of CCS-MPC algorithm at LFM operation (≈ 10 Hz). Proposed compensation method (left). Performance of the adjustable-weight CCS-MPC proposed in [62] (right). Notice that the reduction in the circulating current magnitude is about 39 % with the method proposed in this work [see (c) and (i) above]. (a)-(g) Cluster capacitor voltages. (b)-(h) First two rows of the perturbation vector of (3.15). (c)-(i) Circulating currents. (d)-(j) AC port currents (e)-(k) Common-mode voltages (f)-(l) DC port currents.

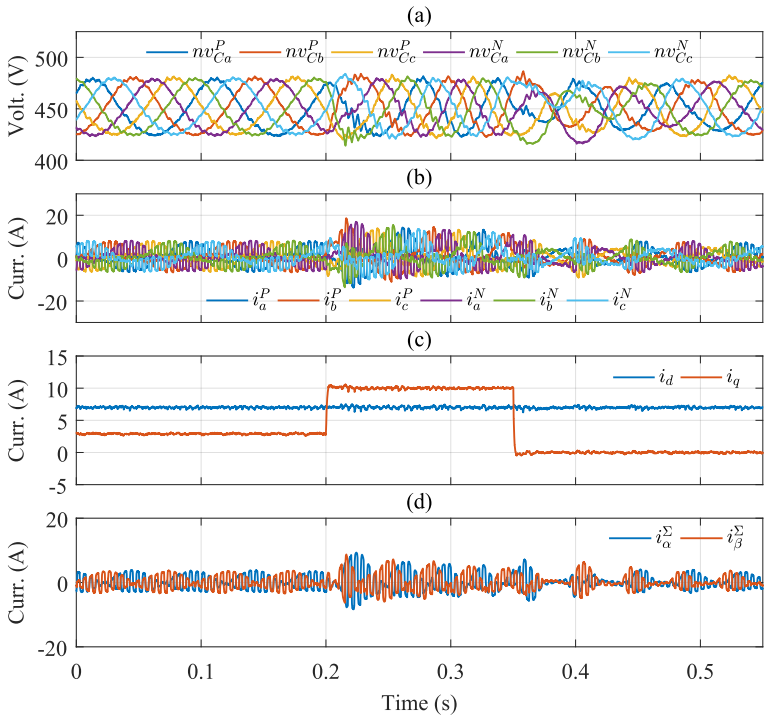

Figure 3.6: Performance of the proposed compensation method for a step change in the machine torque current from 2.7 A to 10 A and from 10 A to 0 A. a) Cluster capacitor voltages. b) Cluster currents. c) Torque and magnetising currents. d) Circulating currents.

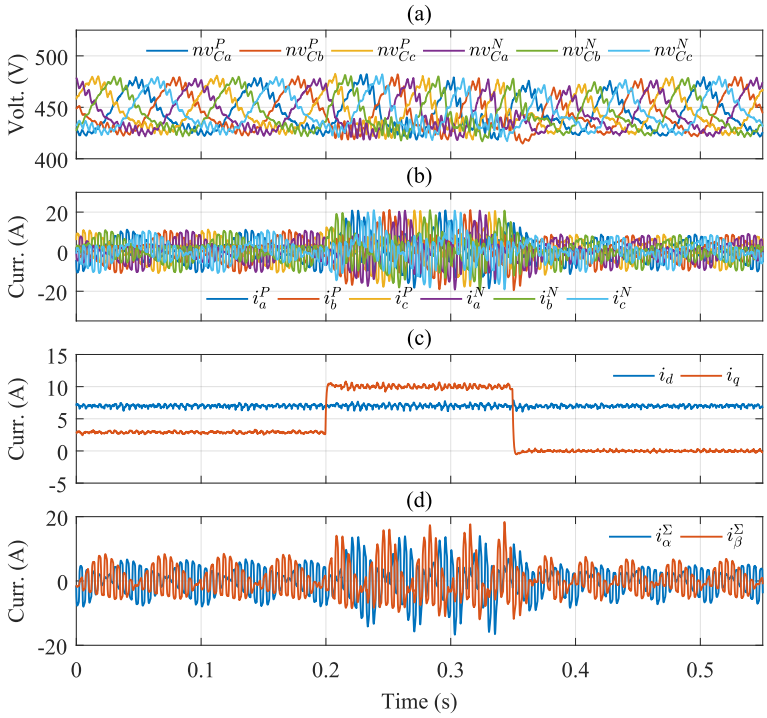

Figure 3.7: Performance of the adjustable-weight compensation method proposed in [62], for a step change in the machine torque current from 2.7 A to 10 A and from 10 A to 0 A.

Figs. 3.6 and 3.7 show the performance when the cage machine is operating at 10 Hz with a magnetising current of 7 A peak, when step changes in the torque current from 2.7 A to 10 A and from 10 A to 0 are produced at $t = 0.2$ s and $t = 0.35$ s respectively. The results depicted in Fig. 3.6 correspond to the proposed control strategy; meanwhile, the results depicted in Fig. 3.7 correspond to the strategy reported in [62]. The peak value of the circulating currents in Fig. 3.6 is 9.3 A with an effective value of 5.4 A in the cluster currents. Conversely, for the test shown in Fig. 3.7, the peak of the circulating current is 18.34 A with an effective value of 7.7 A in the cluster currents. Therefore, the proposed control strategy achieves a reduction of about 50 % in the peak value of the circulating current during the transient. Again, this noticeable current reduction is partly due to the compensation of the perturbation vector $\boldsymbol{d}^{v}_{k+1}$ at the $(k+1)_{th}$ sample. Moreover, as aforementioned, the proposed single-stage CCS-MPC utilised constant weight matrices without increasing some of the weights of the cost function during LFM operation.

3.4.2. Operation of the Proposed CCS-MPC in Drive Applications

The proposed control system can be used for variable speed drives and other applications. This is experimentally validated in this section. The cage machine is operated with $i_{sd} = 7$ A for the test discussed below. The processing time for the proposed CCS-MPC, including the rotor flux-orientated vector control of the cage machine, is 13.42 μs. This processing time represents 26.84 % of the total sampling period, which is lower than both the 31.6 % observed for the CCS-MPC reported in [62] and the 29.8 % recorded for a conventional SISO strategy based on linear controllers (see [17]). Moreover, unlike FCS-MPC-based strategies [64], it should be noted that the execution time of the proposed CCS-MPC algorithm does not depend on the number of submodules in each cluster, thus maintaining a constant computational complexity. Additionally, in applications where a higher number of submodules are required, the sampling frequency could be reduced to minimise switching losses [66]. This allows for more time to execute the control strategy, making it feasible to implement the control strategy on platforms with lower performance capabilities.

Fig. 3.8 shows the performance of the proposed CCS-MPC considering a speed reversal between ±2000 rpm [see Fig. 3.8(a)]. The cluster currents [Fig. 3.8(b)], cage stator currents [Fig. 3.8(c)], circulating currents [Fig. 3.8(d)], capacitor voltages [Fig. 3.8(e)] and the δ value of (3.28) [see Fig. 3.8(e)] are also shown in this graphic. The stator machine's peak current is about 13A at the maximum rotational speed and it is decreased when the rotational speed approaches zero. Conversely, when the rotational speed decreases (for $t > 7$ s), the circulating currents increase to mitigate the low-frequency capacitor voltage pulsations produced in (3.7)(a) and (b). As expected, the maximum amplitude of the circulating currents is produced when the rotational speed is around 0 rpm.

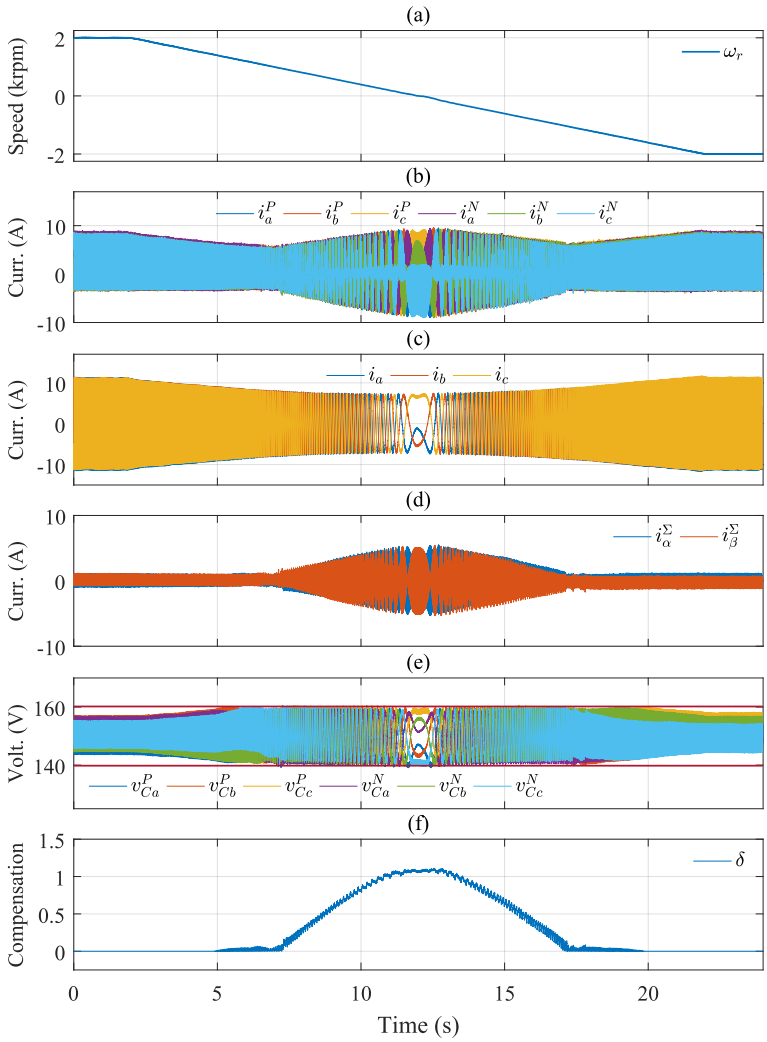

Figure 3.8: System response to a ramp speed variation (from 2 krpm to -2 krpm). a) Rotational speed. b) Cluster currents. c) Machine currents. d) Circulating currents e) Capacitor voltages and 7.5 % voltage-band. e) Value of δ used in (3.28).

Fig. 3.8(e) shows the good regulation of the capacitor voltages around the reference value (150 V) and considering a maximum voltage band of 7.5 %. The capacitor voltages are regulated using the value of δ [see Fig. 3.8(e).] which is obtained from the PI controller shown at the top of the left-hand side of Fig. 3.3. As discussed in this work, when the AC port output frequency is relatively high, the capacitor voltage oscillations are naturally filtered out by the capacitance and the square/trapezoidal common-mode voltage is not necessary, because the machine is operating at HFM. When the AC port frequency is relatively low, a value of $\delta > 0$ is utilised in (3.7) to compensate for the low-frequency perturbation in $\boldsymbol{d}^v$.

The performance of the proposed CCS-MPC, limiting the cluster current, is shown in Figs. 3.9 and 3.10. For these experimental tests, a ramp variation between 0 to 10 A is applied to the torque current i_{sq} maintaining the rotor blocked. The ramp starts at $t = 0$ s reaching 10 A in $t \approx 11.4$ s. The cluster currents have components of AC (cage-machine slip frequency), DC and the variable frequency component (mainly 200 Hz) in the circulating current. For this test, the cluster currents are limited to ± 17 A.

Fig. 3.9(a) shows the cluster currents and the current limits of ± 17 A. It is concluded that

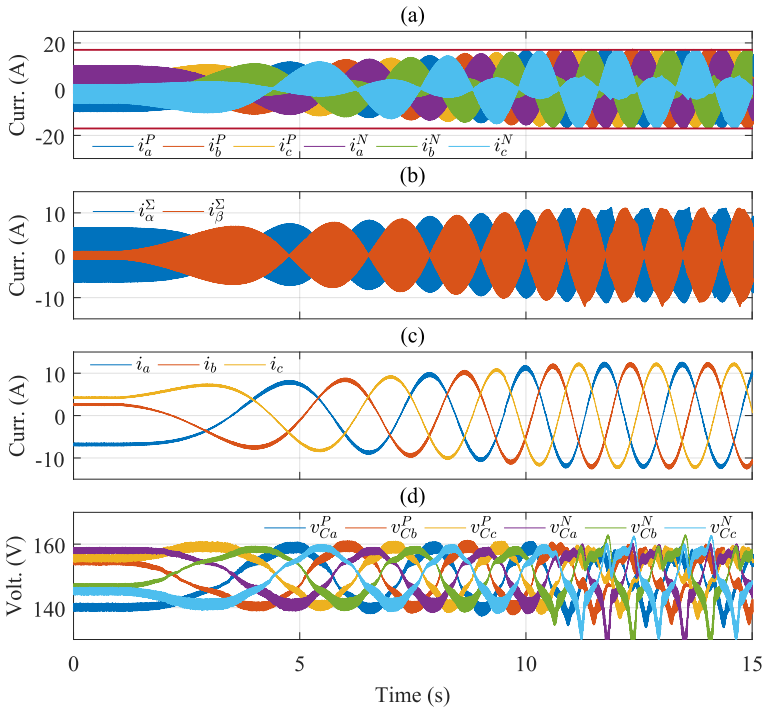

Figure 3.9: Performance of the proposed CCS-MPC including total cluster current limiting at 17 A. A torque current ramp (from 0 A to 10 A) is applied with rotor blocked and a magnetising current of $i_{sd} = 7$ A. (a) Cluster currents. (b) Circulating currents. (c) Machine currents. (d) Capacitor voltages.

the solution of the optimal problem with restrictions [see (3.21)-(3.23)] effectively limits the cluster currents. However, after $t \approx 11.4$ s, the capacitor voltages have excursions outside the voltage band; these excursions are produced because the maximum circulating current synthesised in each cluster is insufficient to maintain the capacitor voltages inside the predefined band. However, any current limitation algorithm, i.e. the proposed one or otherwise, will have problems regulating the capacitor voltages, because the current limits used for the experimental results depicted in Fig. 3.9 are below the required minimum.

An enlarged view of a section of Fig. 3.9 is shown in Fig. 3.10. Notice the trimming in the cluster current [see Fig. 3.10(a)], which is produced by the limitation of the circulating currents $\boldsymbol{i}_{\alpha\beta}^{\Sigma}$ [see Fig. 3.10(b)] in the optimal problem of (3.21). Even when the capacitor voltages have some relatively small excursions outside the predefined band, as shown in Fig. 3.10(d), the AC port currents depicted in Fig. 3.10(c) are well-regulated with a reduced Total Harmonic Distortion (THD) of 2.61 %. Therefore, because of the relatively small capacitor voltage variations, the current limitation algorithm does not affect the current waveform quality much.

Fig. 3.11 shows the performance of the proposed CCS-MPC considering the same test but without limiting the cluster currents [see Fig. 3.11(a)]. As a result, the capacitor voltages are well regulated, without excursions outside the predefined band [see Fig. 3.11(d)], and the THD of the AC port currents, shown in Fig. 3.11(c) decreases to 2.41 %. Moreover, as shown in Fig. 3.11(b), the circulating currents are no longer constrained.

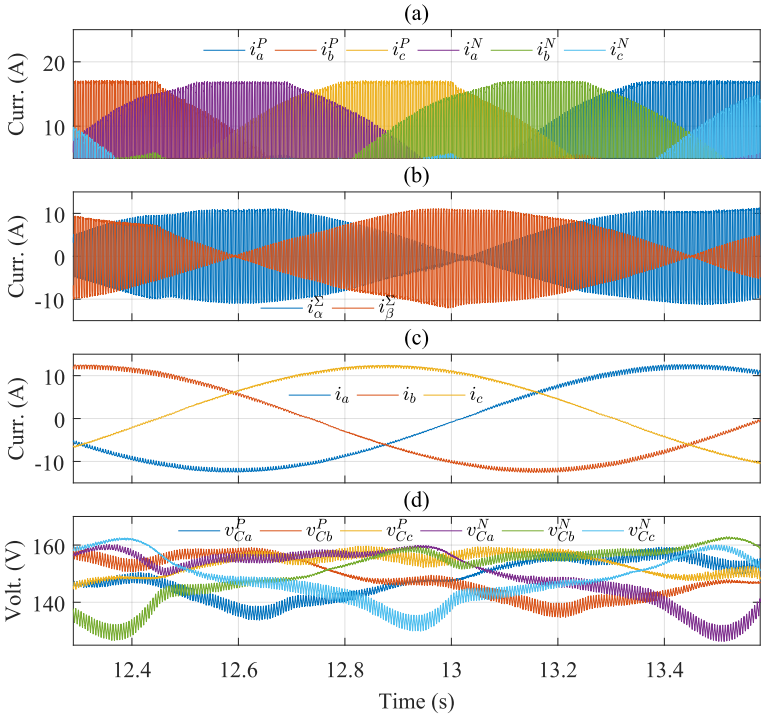

Figure 3.10: Enlarged view of Fig. 3.9.

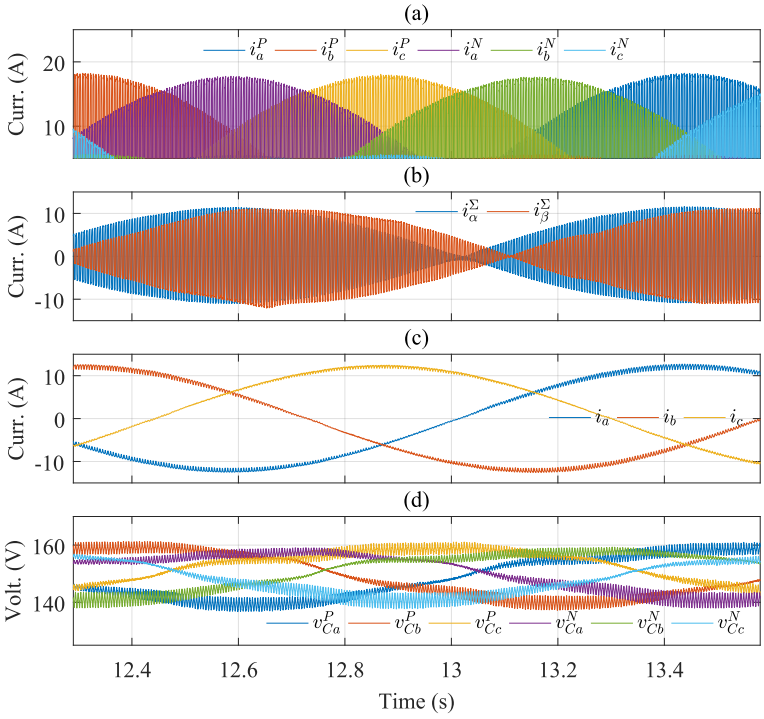

Figure 3.11: Performance of the proposed CCS-MPC, for the same test depicted in Fig. 3.10, but without considering restrictions in the total cluster currents. (a) Cluster currents. (b) Circulating currents. (c) Machine currents. (d) Capacitor voltages.

3.5. Conclusions

This work has presented a new enhanced single-stage two-step CCS-MPC algorithm, for Modular Multilevel Converters operating with variable output frequency in the AC port. The control algorithm is based on a two-step predictive control strategy for the regulation of the capacitor voltages and a single-step prediction of the circulating current required to balance the capacitor energy in the converter. A single cost function, involving the seven states of the MMC and including constraints, is utilised in the proposed CCS-MPC. Therefore, the solution of the optimal problem with restrictions leads to a single global optimum.

A novel methodology to compensate for the future perturbations has been shown to be very effective when the AC port is operating at LFM. This compensating algorithm is based on the Moore-Penrose pseudoinverse matrix, which produces a reference input for the required circulating currents. It has been experimentally demonstrated that the proposed compensation achieves a noticeable reduction in the circulating currents as well as a significant increase in the efficiency of the MMC-based drive, without jeopardising the good dynamic performance typically achieved with CCS-MPC algorithms. An additional advantage of the control methodologies discussed in Sections 3.3.3 and 3.3.4 is their ability to allow the operation of the proposed CCS-MPC with fixed weight-cost matrices during LFM and HFM.

Experimental validation of the proposed CCS-MPC considering variable frequency and voltage at the AC port has been performed using an 18-cell MMC prototype driving a 7.5 kW-cage induction machine operating in a wide speed range. A dSPACE MicroLabBox platform is used to control the MMC-based drive, implementing the CCS-MPC algorithm, the modulation stage, and the active-set method required to solve the quadratic problem with constraints, all that implemented with a reduced computational burden of 13.42 μs. For all the tests performed, i.e. step changes in the currents, cage machine speed reversal, rotor blocked operation, etc., the dynamic and steady-state performance of the proposed CCS-MPC, has been very good.

Appendix

3.1. Current and Voltage Constraints

The voltage that each cluster can synthesise is bounded between zero and the maximum voltage available in each cluster (nv_{Ca}^{P}, nv_{Cb}^{P}, nv_{Cc}^{P}, nv_{Ca}^{N}, nv_{Cb}^{N} and nv_{Cc}^{N}). These boundaries produce a total of 12 constraints, two for each cluster. However, the constraints can be reduced to six, taking advantage of the symmetries between the upper and lower clusters of the converter [16, 62]. Therefore, the matrices $\boldsymbol{G}^{v}$ and $\boldsymbol{W}^{v}$ are given by :

$$\boldsymbol{G}^{v} = \begin{bmatrix} -1 & 0 \\ \frac{1}{2} & -\frac{\sqrt{3}}{2} \\ \frac{1}{2} & \frac{\sqrt{3}}{2} \\ 1 & 0 \\ -\frac{1}{2} & \frac{\sqrt{3}}{2} \\ -\frac{1}{2} & -\frac{\sqrt{3}}{2} \end{bmatrix} \quad , \quad \boldsymbol{W}^{v} = \begin{bmatrix} -\min\left(v_1 + nv_{Ca}^{P}(k), v_4 + nv_{Ca}^{N}(k)\right) \\ -\min\left(v_2 + nv_{Cb}^{P}(k), v_5 + nv_{Cb}^{N}(k)\right) \\ -\min\left(v_3 + nv_{Cc}^{P}(k), v_6 + nv_{Cc}^{N}(k)\right) \\ \max\left(v_1, v_4\right) \\ \max\left(v_2, v_5\right) \\ \max\left(v_3, v_6\right) \end{bmatrix} \tag{3.1}$$

where the voltage required to synthesise the common-mode voltage and to control the AC and DC ports is given by,

$$\begin{bmatrix} v_1 \\ v_2 \\ v_3 \\ v_4 \\ v_5 \\ v_6 \end{bmatrix} = \begin{bmatrix} -v_0^{\Sigma}(k) - \frac{1}{2}v_0^{\Delta}(k) - \frac{1}{2}v_{\alpha}^{\Delta}(k) \\ -v_0^{\Sigma}(k) - \frac{1}{2}v_0^{\Delta}(k) + \frac{1}{4}v_{\alpha}^{\Delta}(k) - \frac{\sqrt{3}}{4}v_{\beta}^{\Delta}(k) \\ -v_0^{\Sigma}(k) - \frac{1}{2}v_0^{\Delta}(k) + \frac{1}{4}v_{\alpha}^{\Delta}(k) + \frac{\sqrt{3}}{4}v_{\beta}^{\Delta}(k) \\ -v_0^{\Sigma}(k) + \frac{1}{2}v_0^{\Delta}(k) + \frac{1}{2}v_{\alpha}^{\Delta}(k) \\ -v_0^{\Sigma}(k) + \frac{1}{2}v_0^{\Delta}(k) - \frac{1}{4}v_{\alpha}^{\Delta}(k) + \frac{\sqrt{3}}{4}v_{\beta}^{\Delta}(k) \\ -v_0^{\Sigma}(k) + \frac{1}{2}v_0^{\Delta}(k) - \frac{1}{4}v_{\alpha}^{\Delta}(k) - \frac{\sqrt{3}}{4}v_{\beta}^{\Delta}(k) \end{bmatrix} \tag{3.2}$$

In the case of currents, 12 constraints are also required to limit the maximum and minimum current $\pm i_{max}$ of six clusters. This maximum value is selected considering the thermal issues related to the maximum peak current allowed in the clusters (see [16]). Using a similar methodology that is used to derive (3.1)-(3.2), current constraints can also be reduced to six using the symmetries between the upper and the lower clusters of the converter. Therefore the matrices that include the current limitations are,

$$\boldsymbol{G}^i = \begin{bmatrix} -1 & 0 \\ \frac{1}{2} & -\frac{\sqrt{3}}{2} \\ \frac{1}{2} & \frac{\sqrt{3}}{2} \\ 1 & 0 \\ -\frac{1}{2} & \frac{\sqrt{3}}{2} \\ -\frac{1}{2} & -\frac{\sqrt{3}}{2} \end{bmatrix} \quad , \quad \boldsymbol{W}^i = \begin{bmatrix} -i_{max} - \min(i_1, i_4) \\ -i_{max} - \min(i_2, i_5) \\ -i_{max} - \min(i_3, i_6) \\ -i_{max} + \max(i_1, i_4) \\ -i_{max} + \max(i_2, i_5) \\ -i_{max} + \max(i_3, i_6) \end{bmatrix} \tag{3.3}$$

where

$$\begin{bmatrix} i_1 \\ i_2 \\ i_3 \\ i_4 \\ i_5 \\ i_6 \end{bmatrix} = \begin{bmatrix} -\frac{1}{3}i_{dc}(k) - \frac{1}{2}i_\alpha(k) \\ -\frac{1}{3}i_{dc}(k) + \frac{1}{4}i_\alpha(k) - \frac{\sqrt{3}}{4}i_\beta(k) \\ -\frac{1}{3}i_{dc}(k) + \frac{1}{4}i_\alpha(k) + \frac{\sqrt{3}}{4}i_\beta(k) \\ -\frac{1}{3}i_{dc}(k) + \frac{1}{2}i_\alpha(k) \\ -\frac{1}{3}i_{dc}(k) - \frac{1}{4}i_\alpha(k) + \frac{\sqrt{3}}{4}i_\beta(k) \\ -\frac{1}{3}i_{dc}(k) - \frac{1}{4}i_\alpha(k) - \frac{\sqrt{3}}{4}i_\beta(k) \end{bmatrix} \tag{3.4}$$

Notice that the currents must be limited at instant $k+1$ [see (3.21)]. However, in this work, as discussed in Section 3.3.2, it is assumed that the AC and DC port current measured in $t = kT$ have the same values in $t = (k+1)T$. This approximation is reasonable when the time constants of the port dynamics are high compared to the sampling time (see [16]). Nevertheless, if a low sampling rate is used, the modelling of the AC and DC ports can be required to obtain better current predictions.

Chapter 4

Continuous Control Set Model Predictive Control of a Hybrid-MMC for Wind Energy Applications

This chapter is based on the journal paper:

Y. Arias-Esquivel, R. Cárdenas, M. Díaz, and L. Tarisciotti, "Continuous Control Set Model Predictive Control of a Hybrid-MMC for Wind Energy Applications," *IEEE Transactions on Industrial Electronics*, 2023.

which is currently under review in the journal IEEE Transactions on Industrial Electronics (Q1 journal paper. Impact Factor: 7.7)

Abstract: This paper discusses a continuous control set model predictive control system of a hybrid modular multilevel converter, driving a direct drive permanent magnet synchronous generator, for variable-speed wind energy applications. The hybrid converter enables operation at a reduced DC-link voltage without the need for circulating currents, even during low-frequency operation in the AC port. To further reduce cluster currents, the capacitor voltages are allowed to oscillate inside predefined voltage limits. The control system is based on a single-step predictive control algorithm, whose outputs are the DC-link and common-mode voltages required to balance the converter energy. Furthermore, it is demonstrated in this work that the reference for the common-mode voltage, obtained using an algorithm based on the Moore-Penrose pseudo-inverse matrix, is a third harmonic waveform which can be used to balance the capacitor voltages, as well as increase the modulation index. The proposed control system is validated using a Hardware-in-the-Loop platform and an experimental system consisting of a 5 kW back-to-back hybrid modular multilevel converter, controlled using dSPACE MicroLabBox platforms. The generator is emulated using a programmable power supply.

4.1. Introduction

Renewable energy sources, particularly wind energy, have received significant attention in the last decades due to the growing concern about environmental issues and the depletion of fossil fuels [73]. As a result, there is a trend in developing multi-MW Wind Energy Conversions Systems (WECSs) [74, 75], based on direct-drive Permanent Magnet Synchronous Generators [75–77]. One key component of multi-MW WECSs is the power electronics converters, which are required to interface the high-power WECS to the grid.

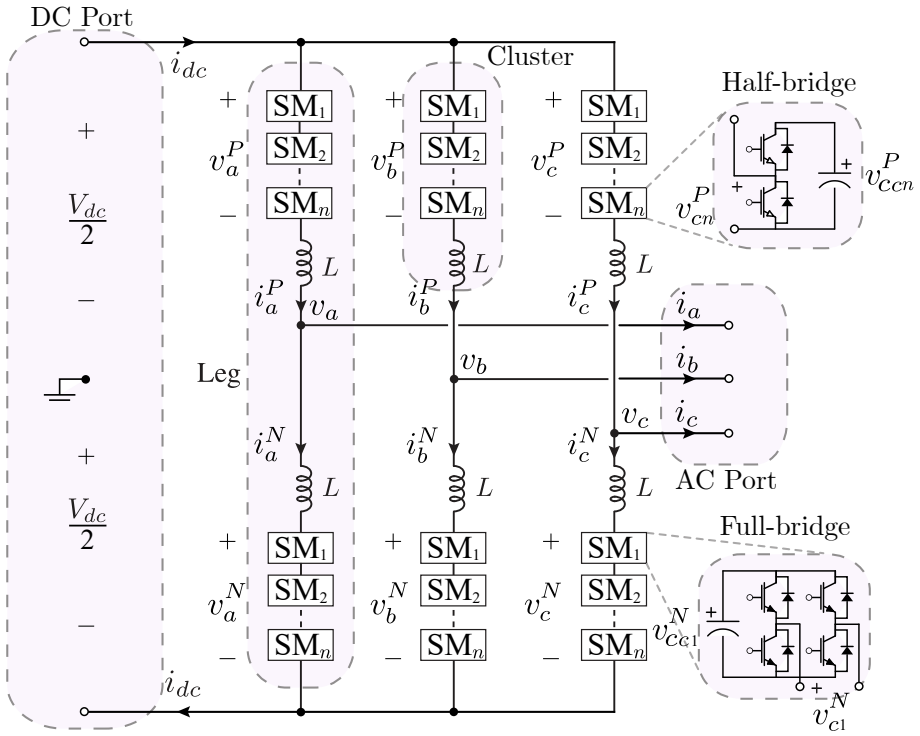

Figure 4.1: Circuit configuration of a hybrid-MMC: The DC port is located on the left-hand side, while the electrical generator is connected to the AC port on the right-hand side. It is important to note that each cluster consists of both half and full SMs.

In recent years, Modular Multilevel Converters (MMCs) have emerged as a new solution for large wind turbine systems due to their high efficiency, scalability, and low harmonic distortion [3, 6]. Nevertheless, despite the advantages of MMCs [1], the required control system is complex and entails various challenges, such as balancing capacitor voltages, maintaining regulated AC port current/voltage, and controlling circulating currents [10, 12, 62]. Moreover, high-power multipole Permanent Magnet Synchronous Generators (PMSGs) used for direct-drive WECSs, are usually designed to operate with a relatively low nominal electrical frequency, which is even lower in the region near the WECS cut-in wind speed [75, 76]. This could produce an operating problem because, for an MMC-based drive, the magnitude of the Capacitor Voltage Oscillations (CVOs) is inversely proportional to the AC port operating frequency [10, 12]. Therefore, a good control system has to be implemented to avoid large voltage oscillations in the floating capacitors during low-frequency operation.

In an MMC, the CVOs are typically mitigated using circulating currents and common-mode voltage [10, 62, 78]. Nonetheless, using large circulating currents increases the converter

losses and reduces the current capacity available in the switches. Therefore, to reduce or eliminate the circulating currents in MMC-based drives, several papers have proposed the utilisation of hybrid topologies, i.e. MMCs implemented using a combination of full-bridge and half-bridge Sub-Modules (SMs) in each cluster [79–81], allowing to reduce the DC-link voltage (see the left side of Fig. 4.1) without jeopardising the control of the electrical generator currents.

Fig. 4.1 depicts the hybrid Modular Multilevel Converter (hybrid-MMC)-based drive topology proposed in this work. For the experimental work discussed in Section 4.4, the back-to-back hybrid-MMC topology shown in Fig. 4.2 is used, where a grid-side hybrid-MMC regulates the DC-link voltage. Notice that this grid-side converter could be replaced with another topology [80, 81]. However, exploring these alternatives and their control mechanisms is considered outside the scope of this work.

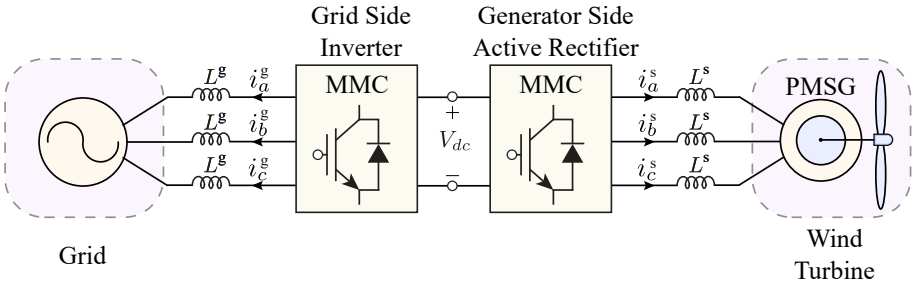

Figure 4.2: Scheme of the BTB-MMC direct-drive PMSG wind turbine system.

As discussed in several papers [19, 62], an MMC is a Multiple-Input, Multiple-Output (MIMO) system; therefore, SISO-designed control systems, as those discussed in [10, 12, 79], can hardly compensate all the cross-coupling between state variables and deliver sub-optimal performance. For this reason, this paper proposes a novel control strategy, based on a MIMO-designed Continuous Control Set Model Predictive Control (CCS-MPC) algorithm, to regulate the CVOs in the generator-side MMC of Fig. 4.2, utilising only the DC-link voltage and common-mode voltage as control actions. Furthermore, as shown in this work, better performance is obtained when the generator-side CVOs are allowed to operate within predefined limits, such as 5 % to 10 % around the voltage reference value [62, 78]. Additionally, as discussed in Section 4.3.3, this methodology enables the operation of the converter with lower cluster current, as circulating currents are not required, and the DC component is reduced.

To the best of the authors' knowledge, this is the first work where the DC-link and common-mode voltages are used to balance the capacitor voltages of the machine-side hybrid-MMC, without requiring circulating currents. Moreover, the absence of circulating currents significantly simplifies the power model of the MMC, thereby streamlining the converter control. Additionally, the proposed control strategy, based on CCS-MPC, can be solved without the need for an online solver, simplifying the implementation of the strategy.

The rest of this paper is organised as follows. Section 4.2 provides a brief overview of the MMC modelling. The CCS-MPC formulation for regulating the capacitor voltages is presented in Section 4.3. Section 4.4 discusses the experimental results. Finally, Section 4.5 presents the conclusions.

4.2. Modular Multilevel Converter

The MMC modelling utilised in this work has been extensively discussed in the literature [10, 12, 62]. However, for completeness, a brief introduction to the $\Sigma\Delta\alpha\beta 0$-transform is provided in this section. This transform is defined by [12]:

$$\boldsymbol{X}_{\alpha\beta 0}^{\Sigma\Delta} \doteq \begin{bmatrix} \frac{1}{2} & \frac{1}{2} \\ 1 & -1 \end{bmatrix} \cdot \boldsymbol{X}_{abc}^{PN} \cdot \begin{bmatrix} \frac{2}{3} & 0 & \frac{1}{3} \\ -\frac{1}{3} & \frac{1}{\sqrt{3}} & \frac{1}{3} \\ -\frac{1}{3} & -\frac{1}{\sqrt{3}} & \frac{1}{3} \end{bmatrix} \tag{4.1}$$

where $\boldsymbol{X}_{abc}^{PN}$ is a matrix with the instantaneous abc variables and $\boldsymbol{X}_{\alpha\beta 0}^{\Sigma\Delta}$ is the matrix with the transformed values. The current-voltage model that describes the dynamics of the currents is obtained using Fig. 4.1 as

$$\frac{V_{dc}}{2}\begin{bmatrix} 1 & 1 & 1 \\ 1 & 1 & 1 \end{bmatrix} = \begin{bmatrix} v_a^P & v_b^P & v_c^P \\ v_a^N & v_b^N & v_c^N \end{bmatrix} + L\frac{d}{dt}\begin{bmatrix} i_a^P & i_b^P & i_c^P \\ i_a^N & i_b^N & i_c^N \end{bmatrix} + \begin{bmatrix} v_a & v_b & v_c \\ -v_a & -v_b & -v_c \end{bmatrix} \tag{4.2}$$

then by applying (4.1) to (4.2) yields

$$\frac{1}{2}\begin{bmatrix} 0 & 0 & V_{dc} \\ 0 & 0 & 0 \end{bmatrix} = \begin{bmatrix} v_\alpha^\Sigma & v_\beta^\Sigma & v_0^\Sigma \\ v_\alpha^\Delta & v_\beta^\Delta & v_0^\Delta \end{bmatrix} + L\frac{d}{dt}\begin{bmatrix} i_\alpha^\Sigma & i_\beta^\Sigma & \frac{1}{3}i_{dc} \\ i_\alpha & i_\beta & 0 \end{bmatrix} + 2\begin{bmatrix} 0 & 0 & 0 \\ v_\alpha & v_\beta & v_0 \end{bmatrix} \tag{4.3}$$

where the terms $\boldsymbol{i}_{\alpha\beta}^\Sigma$ refer to the circulating currents ($\boldsymbol{i}_{\alpha\beta}^\Sigma = i_\alpha^\Sigma + j i_\beta^\Sigma$), while i_{dc} denotes the DC port current, and v_0 represents the common-mode voltage. Additionally, the variables $\boldsymbol{v}_{\alpha\beta}$ and $\boldsymbol{i}_{\alpha\beta}$ correspond to the machine voltages and currents, and are expressed in $\alpha\beta 0$-coordinates.

The voltages and currents in the clusters can be utilised to derive the instantaneous power fluctuations [12, 13]. These powers can be expressed as $p_i^j = v_i^j i_i^j \;\forall\; i \in \{a, b, c\}$ and $j \in \{P, N\}$. When the voltage of the capacitors is close to the reference voltage $\overline{v}_C^*$, the power can be approximated as a function of the capacitor voltage, i.e.:

$$\begin{bmatrix} p_a^P & p_b^P & p_c^P \\ p_a^N & p_b^N & p_c^N \end{bmatrix} \approx n_T C \overline{v}_C^* \frac{d}{dt}\begin{bmatrix} v_{Ca}^P & v_{Cb}^P & v_{Cc}^P \\ v_{Ca}^N & v_{Cb}^N & v_{Cc}^N \end{bmatrix} \tag{4.4}$$

where n_T and C represent the numbers of SMs per cluster ($n_T = n_F + n_H$) and the capacitance, respectively. The term n_H represents the number of half-bridges, and n_F represents the number of full-bridges. Additionally, v_{Ci}^j are the capacitor voltages. Applying the $\Sigma\Delta\alpha\beta 0$-transformation to (4.4), yields

$$\begin{bmatrix} p_\alpha^\Sigma & p_\beta^\Sigma & p_0^\Sigma \\ p_\alpha^\Delta & p_\beta^\Delta & p_0^\Delta \end{bmatrix} \approx n_T C \overline{v}_C^* \frac{d}{dt}\begin{bmatrix} v_{C\alpha}^\Sigma & v_{C\beta}^\Sigma & v_{C0}^\Sigma \\ v_{C\alpha}^\Delta & v_{C\beta}^\Delta & v_{C0}^\Delta \end{bmatrix} \tag{4.5}$$

By neglecting both the voltage drops in the inductors and the circulating currents, the powers of (4.5) are obtained after some mathematics manipulations (see [10, 12]). The results are shown in (4.6), where the symbol "$\circ$" denotes the dot product, $k = n_T C \overline{v}_C^*$ [see (4.5)] and the superscript "c" represents the complex conjugate operator.

$$k \cdot \frac{dv^{\Sigma}_{C\alpha\beta}}{dt} \approx \boldsymbol{p}^{\Sigma}_{\alpha\beta} = -\frac{1}{4}\left(\boldsymbol{i}_{\alpha\beta}\boldsymbol{v}_{\alpha\beta}\right)^{c} - \frac{1}{2}v_0\boldsymbol{i}_{\alpha\beta} \tag{4.6a}$$

$$k \cdot \frac{dv^{\Delta}_{C\alpha\beta}}{dt} \approx \boldsymbol{p}^{\Delta}_{\alpha\beta} = \frac{1}{2}V_{dc}\boldsymbol{i}_{\alpha\beta} - \frac{2}{3}i_{dc}\boldsymbol{v}_{\alpha\beta} \tag{4.6b}$$

$$k \cdot \frac{dv^{\Delta}_{C0}}{dt} \approx p^{\Delta}_{0} = -\frac{2}{3}i_{dc}v_0 \tag{4.6c}$$

$$k \cdot \frac{dv^{\Sigma}_{C0}}{dt} \approx p^{\Sigma}_{0} = \frac{1}{6}V_{dc}i_{dc} - \frac{1}{4}\left(\boldsymbol{v}_{\alpha\beta} \circ \boldsymbol{i}_{\alpha\beta}\right) \tag{4.6d}$$

The MMC converter is balanced when the five capacitor voltage components, $[\boldsymbol{v}^{\Sigma}_{C\alpha\beta}, \boldsymbol{v}^{\Delta}_{C\alpha\beta}, v^{\Delta}_{C0}]$ are driven to ≈ 0. The control strategy proposed in this work for the regulation of these capacitor voltages, is based on CCS-MPC and is discussed in Section 4.3.

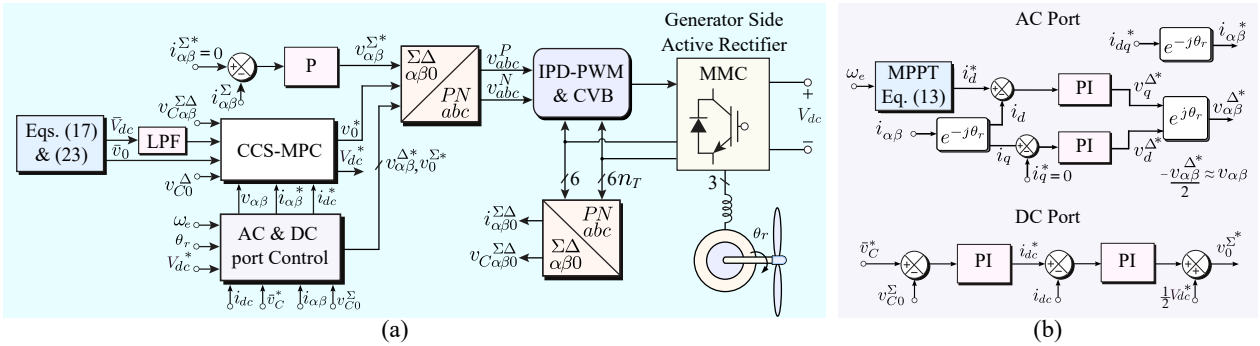

Figure 4.3: Proposed CCS-MPC algorithm for the control of a hybrid-MMC driving a PMSG-based WECS. (a) CCS-MPC, (b) Control system for the currents and voltages in the AC and DC ports.

4.3. Proposed CCS-MPC

To balance the voltage of the capacitors, a discrete-time state model is obtained by discretising (4.6a) - (4.6c) using the forward Euler method [58]. The resulting model is expressed in terms of the sampling time T_s.

$$\boldsymbol{x}_{k+1} \approx \boldsymbol{A}\boldsymbol{x}_k + \boldsymbol{B}_k\boldsymbol{u}_k + \boldsymbol{d}_k \tag{4.7}$$

with the matrices

$$
\begin{aligned}
\boldsymbol{x}_k &= \begin{bmatrix} v_{C\alpha}^{\Delta}(k) & v_{C\beta}^{\Delta}(k) & v_{C0}^{\Delta}(k) & v_{C\alpha}^{\Sigma}(k) & v_{C\beta}^{\Sigma}(k) \end{bmatrix}^T \\
\boldsymbol{u}_k &= \begin{bmatrix} V_{dc}(k) & v_0(k) \end{bmatrix}^T \\
\boldsymbol{B}_k &= \frac{T_s}{2k} \begin{bmatrix} i_\alpha(k) & i_\beta(k) & 0 & 0 & 0 \\ 0 & 0 & -\frac{4}{3} i_{dc}(k) & -i_\alpha(k) & -i_\beta(k) \end{bmatrix}^T \\
\boldsymbol{d}_k &= \frac{T_s}{k} \begin{bmatrix} -\frac{2}{3} i_{dc}(k) v_\alpha(k) \\ -\frac{2}{3} i_{dc}(k) v_\beta(k) \\ 0 \\ \frac{1}{4} i_\beta(k) v_\beta(k) - \frac{1}{4} i_\alpha(k) v_\alpha(k) \\ \frac{1}{4} i_\beta(k) v_\alpha(k) + \frac{1}{4} i_\alpha(k) v_\beta(k) \end{bmatrix}
\end{aligned}
\tag{4.8}
$$

Additionally, the matrix $\boldsymbol{A}$ is a 5×5 identity matrix. Notice that the term (4.6d) is not considered in the discrete-time model since this term represents the total energy stored in the generator-side MMC capacitors. Therefore, (4.6d) is a slow dynamic term that can be effectively regulated using a simple PI controller (see Fig. 2.2b).

The proposed control system is shown in Fig. 2.2. The CCS-MPC to regulate the generator-side Hybrid-MMC capacitor voltages is shown in Fig. 2.2(a). The control of the PMSG, as well as the regulation of (4.6d) is shown in Fig. 2.2(b).

4.3.1. Control of the CVOs

As shown in (4.8), V_{dc} is the control input for the states $v_{C\alpha}^{\Delta}$ and $v_{C\beta}^{\Delta}$. Additionally, the states v_{C0}^{Δ}, $v_{C\alpha}^{\Sigma}$, and $v_{C\beta}^{\Sigma}$ are regulated using v_0. To control the states ($\boldsymbol{x}_k$), a one-step prediction CCS-MPC is proposed. The proposed cost function is as follows, where the one-step delay compensation algorithm, discussed in [58], is considered.

$$
\begin{aligned}
\min_{\boldsymbol{x}_{k+1}, \boldsymbol{u}_k} \quad & J = \left(\boldsymbol{x}_{k+1} - \boldsymbol{x}^*\right)^T \boldsymbol{Q} \left(\boldsymbol{x}_{k+1} - \boldsymbol{x}^*\right) \\
& \quad + \left(\boldsymbol{u}_k - \boldsymbol{u}^*\right)^T \boldsymbol{R} \left(\boldsymbol{u}_k - \boldsymbol{u}^*\right) \\
\text{s.t.} \quad & \boldsymbol{x}_{k+1} = \boldsymbol{A}\boldsymbol{x}_k + \boldsymbol{B}_k \boldsymbol{u}_k + \boldsymbol{d}_k \\
& \boldsymbol{G}\boldsymbol{u}_k \geq \boldsymbol{W}
\end{aligned}
\tag{4.9}
$$

where (4.9) represents a quadratic cost function, with the objective of minimising the difference between the next state $\boldsymbol{x}_{k+1}$ and the desired state $\boldsymbol{x}^*$, weighted by matrix $\boldsymbol{Q}$, as well as minimising the control input difference $(\boldsymbol{u}_k - \boldsymbol{u}^*)$, weighted by matrix $\boldsymbol{R}$. The constraints of the optimisation problem are the equality constraints, i.e. $\boldsymbol{x}_{k+1}$ as a function of the current state $\boldsymbol{x}_k$ and the control input $\boldsymbol{u}_k$. Moreover, the control input $\boldsymbol{u}_k$ has to fulfill the inequality constraint $\boldsymbol{G}\boldsymbol{u}_k \geq \boldsymbol{W}$. The weighting factor matrices, $\boldsymbol{Q}$ and $\boldsymbol{R}$, are given by

$$
\begin{aligned}
\boldsymbol{Q} &= diag(\lambda_\alpha^{\Delta}, \lambda_\beta^{\Delta}, \lambda_0^{\Delta}, \lambda_\alpha^{\Sigma}, \lambda_\beta^{\Sigma}) \\
\boldsymbol{R} &= diag(\lambda_{V_{dc}}, \lambda_{v_0})
\end{aligned}
\tag{4.10}
$$

where $\lambda_{\alpha}^{\Delta}, \lambda_{\beta}^{\Delta}$, etc., represent the weighting factors of the states. The terms $\lambda_{V_{dc}}$ and λ_{v_0} represent the weighting factors of the control actions. As discussed below (4.6), the reference states $\boldsymbol{x}^*$ are set to zero (i.e., $\boldsymbol{x}^* = 0$). The vector $\boldsymbol{u}^*$ is discussed in Section 4.3.3.

4.3.2. Control of the PMSG

The direct-drive PMSG is controlled using a synchronous rotating $d-q$ frame that rotates at $\omega_e t$, where ω_e is the angular frequency of the MMC AC port. The vector control system is orientated along the back-emf of the generator. This is achieved by measuring or estimating (see [82]) the back-emf position. Moreover, in this work the PMSG torque is regulated using a simple Maximum Power Point Tracking (MPPT) algorithm, where the electrical torque and power are proportional to ω_e^2 and ω_e^3 respectively [83–85]. Therefore,

$$T_e = K_{opt}\omega_e^2 \tag{4.11}$$

where the value of K_{opt} is a function of the blade aerodynamics, number of poles, etc. A simplified model of the electrical torque can be obtained as [82]:

$$T_e = \frac{3}{2} p \psi_m i_d \tag{4.12}$$

Where, i_d represents the direct stator current, ψ_m denotes the permanent magnet flux linkage, and p stands for the number of pole pairs. Therefore, the generator reference current for MPPT is given by

$$i_d^* = \frac{2}{3}\frac{K_{opt}\omega_e^2}{p\psi_m} = K_t \omega_e^2 \tag{4.13}$$

Therefore, the active current reference is obtained from (4.13), while the reactive power is defined as zero (i.e., $i_q^* = 0$). These currents are regulated using linear controllers (see Fig. 2.2b).

4.3.3. Calculation of $\boldsymbol{u}^*$

As widely discussed in [62, 78], the peak magnitude value of the CVOs is approximately equivalent to $|\boldsymbol{v}_{C\alpha\beta}^{\Delta}|$. Therefore, from (4.6b), the relationship between the required DC port voltage value in terms of a given value of $|\boldsymbol{v}_{C\alpha\beta}^{\Delta}|$ can be obtained by using some simplifications. This is discussed below.

4.3.3.1. DC-link voltage reference

Integrating (4.6b), and assuming steady state operation, the voltage $\boldsymbol{v}_{C\alpha\beta}^{\Delta}$ is given by

$$\boldsymbol{v}_{C\alpha\beta}^{\Delta} \approx \frac{-j}{\omega_e n_T C \overline{v}_C^*}\left(\frac{1}{2}V_{dc}\boldsymbol{i}_{\alpha\beta} - \frac{2}{3}i_{dc}\boldsymbol{v}_{\alpha\beta}\right) \tag{4.14}$$

where $\boldsymbol{v}_{\alpha\beta} \approx -\boldsymbol{v}_{\alpha\beta}^{\Delta}/2$, with $\boldsymbol{v}_{\alpha\beta}$ as the voltage synthesised by the MMC in the AC port, i.e. at the Point of Common Coupling (PCC) between the MMC and PMSG [see right side of Fig. 2.2(b)]. Referring (4.14) into a synchronous rotating $d-q$ reference frame, the magnitude of the CVOs can be obtained as

$$\left|\boldsymbol{v}_{Cdq}^{\Delta}\right| \approx \frac{1}{|\omega_e|\, n_T C \overline{v}_C^*} \cdot \sqrt{\frac{1}{4}{V_{dc}}^2 \left|\boldsymbol{i}_{dq}\right|^2 - \frac{2}{3} V_{dc} i_{dc} \left(\boldsymbol{v}_{dq} \circ \boldsymbol{i}_{dq}\right) + \frac{4}{9}{i_{dc}}^2 \left|\boldsymbol{v}_{dq}\right|^2} \tag{4.15}$$

As mentioned earlier, the control system proposed for the PMSG regulates the quadrature component of the output current to $i_q = 0$. Furthermore, for simplicity, the quadrature component of the voltage $\boldsymbol{v}_{dq}$ is approximated to zero (i.e., $v_q \approx 0$) in (4.15). By considering these simplifications, the DC-link voltage can be obtained as follows:

$$V_{dc1,2} \approx \frac{\frac{2}{3} i_{dc} v_d i_d \pm |i_d|\, |\omega_e|\, |\boldsymbol{v}_{Cdq}^{\Delta}| n_T C \overline{v}_C^*}{\frac{1}{2} i_d^2} \tag{4.16}$$

In this work, the use of a DC-link voltage reference ($\bar{V}_{dc}$) that regulates $|\boldsymbol{v}_{Cdq}^{\Delta}|$ to a non-zero value between 5 %-10 % of the reference value is proposed, based on the fact that, for a given operating power, increasing the DC-link voltage reduces the current in the clusters. Moreover, to minimise power losses in the converter by reducing the DC cluster current (see [78]), the larger value of (4.16) is used as the reference voltage V_{dc} to be regulated by the grid-side hybrid-MMC, i.e.:

$$\bar{V}_{dc} = \frac{\frac{2}{3} i_{dc} v_d i_d + |i_d|\, |\omega_e|\, |\boldsymbol{v}_{Cdq}^{\Delta}| n_T C \overline{v}_C^*}{\frac{1}{2}{i_d}^2} \tag{4.17}$$

4.3.3.2. Variation of the DC port voltage vs. ω_e

To calculate the variation of the DC port voltage with respect to the operating frequency ω_e, (4.18) is utilised. This equation is derived from (4.17) by assuming that the power losses in the converter are negligible, resulting in $V_{dc} i_{dc} = 3 v_d i_d / 2$. Moreover, the current i_d from (4.13) is replaced in (4.17) yielding:

$$V_{dc} \approx \frac{|\boldsymbol{v}_{Cdq}^{\Delta}| n_T C \overline{v}_C^*}{|K_t \omega_e|} + \sqrt{\left(\frac{|\boldsymbol{v}_{Cdq}^{\Delta}| n_T C \overline{v}_C^*}{|K_t \omega_e|}\right)^2 + 2{v_d}^2} \tag{4.18}$$

Note that (4.18) is an approximation because the converter losses have been neglected. Fig. 4.4 shows the relationship between V_{dc} and ω_e, obtained from (4.18) and considering the characteristics of the 10 MW direct-drive PMSG reported in [75]. This machine has 160 pole pairs, $v_{dmax} \approx 5.97$ kV(phase-neutral), cut-in frequency of ≈ 10.67 Hz and nominal power is reached at ≈ 26.67 Hz. The simple MPPT algorithm discussed in Section 4.3.2 has been considered to obtain Fig. 4.4 where five values of $|\boldsymbol{v}_{Cdq}^{\Delta}|$ are shown. It is worth noting that after reaching a minimum value, the required DC-link voltage starts to increase at low frequencies, particularly when the value of $|\boldsymbol{v}_{Cdq}^{\Delta}|$ is relatively large, for instance, the 10 % curve in Fig.4.4. If $|\boldsymbol{v}_{Cdq}^{\Delta}| \approx 0$, then $V_{dc} = \sqrt{2} v_d$, for the whole operating range.

4.3.3.3. Common-mode voltage reference

Unlike the determination of the DC-link voltage reference, the common-mode voltage reference calculation is performed by analysing the disturbance vector $\boldsymbol{d}_k$ [see (4.8)]. For this purpose, the control action that compensates for disturbances, i.e., the $\boldsymbol{u}_k^*$ that satisfies: $\boldsymbol{x}_{k+1} = \boldsymbol{A}\boldsymbol{x}_k + \boldsymbol{B}_k \boldsymbol{u}_k^* + \boldsymbol{d}_k$ in steady state, that is with $\boldsymbol{x}_{k+1} = \boldsymbol{x}_k$, is calculated. Considering that $\boldsymbol{A}$ is the identity matrix, yields

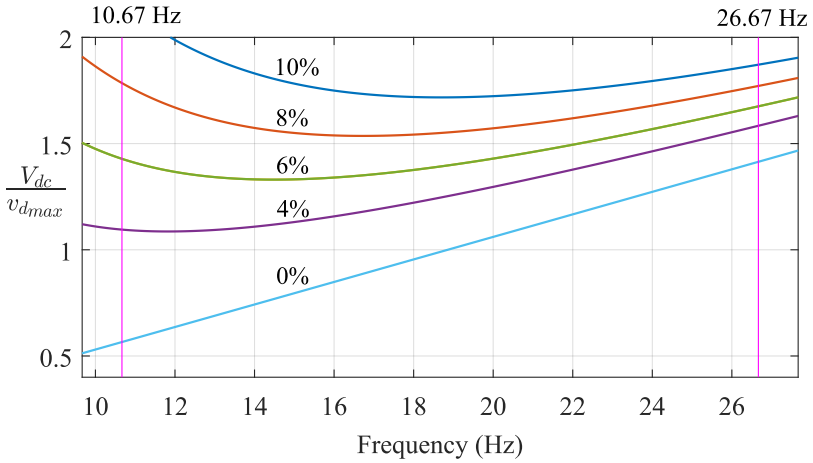

Figure 4.4: Behaviour of the DC-link to generator maximum voltage ratio with respect to frequency for different capacitor oscillation-band percentages.

$$\boldsymbol{u}_k^* = -\boldsymbol{B}_k^{-1}\boldsymbol{d}_k \tag{4.19}$$

However, because matrix $\boldsymbol{B}_k$ is non-invertible, the Moore-Penrose pseudoinverse is used in (4.19),

$$\boldsymbol{u}_k^* = -\boldsymbol{B}_k{}^{\dagger}\boldsymbol{d}_k, \quad \boldsymbol{B}_k{}^{\dagger} = (\boldsymbol{B}_k^T\boldsymbol{B}_k)^{-1}\boldsymbol{B}_k^T \tag{4.20}$$

Notice that solving (4.20) provides solutions for both $\bar{V}_{dc}$ and $\bar{v}_0$. It can be easily demonstrated that the solution for $\bar{V}_{dc}$ is equal to (4.18) when $|\boldsymbol{v}_{Cdq}^{\Delta}| = 0$, that is, $\bar{V}_{dc} = \sqrt{2}v_d$. For the common-mode voltage, after some manipulations and assuming that $v_q \approx 0$ and $i_q \approx 0$, the solution obtained from (4.20) is given by:

$$\bar{v}_0 = \frac{9\, v_d {i_d}^2 \sin(3\theta + 3\pi/2)}{18\, {i_d}^2 + 32\, {i_{dc}}^2} \tag{4.21}$$

where θ is the angle of the $\boldsymbol{v}_{\alpha\beta}$ vector. If the DC-link voltage $\bar{V}_{dc}$ obtained from (4.20) is considered (i.e. $V_{dc} = \sqrt{2}v_d$), power conservation between the DC-link port and the AC port yields,

$$V_{dc} \cdot i_{dc} = \frac{3}{2} v_d \cdot i_d \Rightarrow i_{dc}^2 = \frac{9}{8} i_d^2 \tag{4.22}$$

Replacing (4.22) in (4.21), the common mode voltage obtained is equivalent to that typically used in zero-sequence voltage injection to enhance the modulation index. Therefore, in this work, a third harmonic with an amplitude equal to one-sixth of the generator voltage amplitude is used as a reference [see (4.23)]. Notice that this third harmonic is the one typically used to achieve a modulation index of $m = 1.1547$[86].

$$\bar{v}_0 = \frac{v_d \sin(3\theta + 3\pi/2)}{6} \tag{4.23}$$

In this work, the common-mode voltage $\bar{v}_0$ of (4.23) and the DC-link voltage $\bar{V}_{dc}$ of (4.17)

are used in $\boldsymbol{u}_k^* = [\bar{V}_{dc} \;\; \bar{v}_0]^T$ [see (4.9) and (4.28)]. Note that θ is not the angle corresponding to the PMSG back-emf position. It is the angle of the voltage vector synthesised by the MMC at the PCC.

4.3.4. Calculation of the Number of SMs

A straightforward solution for the number of full and half bridges in each cluster can be obtained when $|\boldsymbol{v}_{Cdq}^{\Delta}| = 0$. In this case and assuming third harmonic injection [see (4.23)], the following relationships have to be fulfilled to avoid overmodulation:

$$n_T \overline{v}_C^* - \frac{\sqrt{3}}{2} v_d \geq \frac{V_{dc}}{2} \geq \frac{\sqrt{3}}{2} v_d - n_F \overline{v}_C^* \tag{4.24}$$

By replacing $V_{dc} \approx \sqrt{2} v_d$ into (4.24), the following expressions are obtained:

$$n_F \geq k_F \frac{v_{d_{max}}}{\overline{v}_C^*} \frac{\sqrt{3} - \sqrt{2}}{2} \tag{4.25}$$

$$n_T \geq k_T \frac{v_{d_{max}}}{\overline{v}_C^*} \frac{\sqrt{3} + \sqrt{2}}{2} \tag{4.26}$$

where the number of half-bridges is calculated as $n_H = n_T - n_F$. The maximum generator voltage, $v_{d_{max}}$, is used as it represents the worst-case scenario. When the voltage band $|\boldsymbol{v}_{Cdq}^{\Delta}| \neq 0$, the total number of modules, n_T and n_F is obtained by using iteratively both (4.18) and (4.24), until both expressions are fulfilled. Moreover, to provide an adequate voltage margin during transients, safety factors ($k_T, k_F \geq 1$) could be considered when calculating n_T and n_F[53].

A similar analysis can be carried out for the grid-side hybrid-MMC. However, such analysis, as well as the discussion of the control system required in that power converter, is considered beyond the scope of this work.

4.3.5. Unconstrained Solution

The unconstrained solution of the optimal problem of (4.9), can be obtained by replacing (4.7) in the cost $\boldsymbol{J}$ and calculating $\boldsymbol{u}_k^{opt}$ from:

$$\frac{d\boldsymbol{J}}{d\boldsymbol{u}_k} = 0 \tag{4.27}$$

Using (4.27) and after some manipulation, the optimal control action is obtained as,

$$\boldsymbol{u}_k^{opt} = -\left(\boldsymbol{B}_k^T \boldsymbol{Q} \boldsymbol{B}_k + \boldsymbol{R}\right)^{-1} \left[\boldsymbol{B}_k^T \boldsymbol{Q} \left(\boldsymbol{A}\boldsymbol{x}_k + \boldsymbol{d}_k\right) - \boldsymbol{R}\boldsymbol{u}^*\right] \tag{4.28}$$

where $\boldsymbol{u}_k^{opt}$ represents the unconstrained optimal control action. This approach provides an analytic solution to the optimisation problem, without needing a solver, which reduces the computational complexity of the proposed control strategy.

The control action $\boldsymbol{u}_k^{opt}$ has two components: the optimal common mode voltage v_0 and the optimal DC-link voltage V_{dc}. Constraints on the voltage v_0, obtained from (4.28), are not necessary because the optimal common-mode voltage closely matches the third harmonic of (4.23), which improves the modulation index rather than causing overmodulation. On the

other hand, the DC-link voltage synthesised by the grid-side converter is bounded between maximum and minimum values of voltages, i.e. $V_{dcmin} \leq V_{dc} \leq V_{dcmax}$, which are dependant on (4.25)-(4.26). Saturation is achieved by limiting, when necessary, the value of $\bar{V}_{dc}$ obtained from (4.17). This is because directly constraining the control action V_{dc} would hinder achieving the balance of voltage $\boldsymbol{v}^{\Delta}_{C\alpha\beta}$.

4.4. Experimental Results

The experimental setup used in this work consists of two identical hybrid-MMCs, each one implemented with 18 SMs, specifically 12 half-bridge cells and 6 full-bridge cells. Control of the power converters is achieved using two dSPACE MicroLabBox platforms equipped with Xilinx Kintex-7 XC7K325T FPGAs. In each FPGA, a modulation scheme based on In-Phase Carrier Disposition (IPD-PWM) and a sorting algorithm are implemented. The number crunching tasks, such as solving the optimisation problems, $\Sigma\Delta\alpha\beta 0$ direct and inverse transforms, control of the AC ports, etc., are performed by the dSPACE processor.

Each hybrid-MMC control platform is equipped with 32 parallel ADCs, enabling simultaneous measurements. The switching signals generated by the control platforms are transmitted to the gate drivers of the MMC switches through optical-fibre links. The switches are MOSFET transistors of 72 A, 300 V, and 19 mΩ on-resistance. For implementing the control algorithms, a sampling time of 50 μs is used, corresponding to a switching frequency of 10 kHz. The parameters of the experimental system are presented in Table 4.1; it is important to note that the voltage-band is set at 6 % of $\bar{v}^{*}_{C}$.

Fig. 4.5 shows the experimental setup, where one of the MMCs is connected to the grid, while the other MMC is connected to a power supply that emulates a PMSG-based direct-drive variable-speed WECS. The emulation is achieved using an Ametek MX45 power supply, which incorporates a pre-stored two-dimensional frequency-voltage profile. This profile is obtained by simulating the WECS model and PMSG design discussed in [75, 87], and then scaling down the results to values which can be handled by the experimental prototype.

Table 4.1: Experimental and HIL Setup Parameters

Description	Variable	Value
Rated power	P	5 kW
HBSMs per cluster	n_H	2
FBSMs per cluster	n_F	1
Cluster inductance	L	2.5 mH
SM capacitance	C	2.2 mF
SM DC voltage	$\bar{v}^{*}_{C}$	117 V
Capacitor voltage oscillations	$\lvert\boldsymbol{v}^{\Delta}_{Cdq}\rvert$	7 V
Carrier frequency	f_s	10 kHz

4.4.1. Testing of the 6 % voltage Band for $|\boldsymbol{v}^{\Delta}_{C\alpha\beta}|$

The programmable Ametek power supply cannot operate below 16 Hz. Therefore, to verify the 6 % limit for $\bar{v}^{*}_{c}$, from 10.67 Hz to 26.67 Hz, Hardware In the Loop (HIL) emulation of the

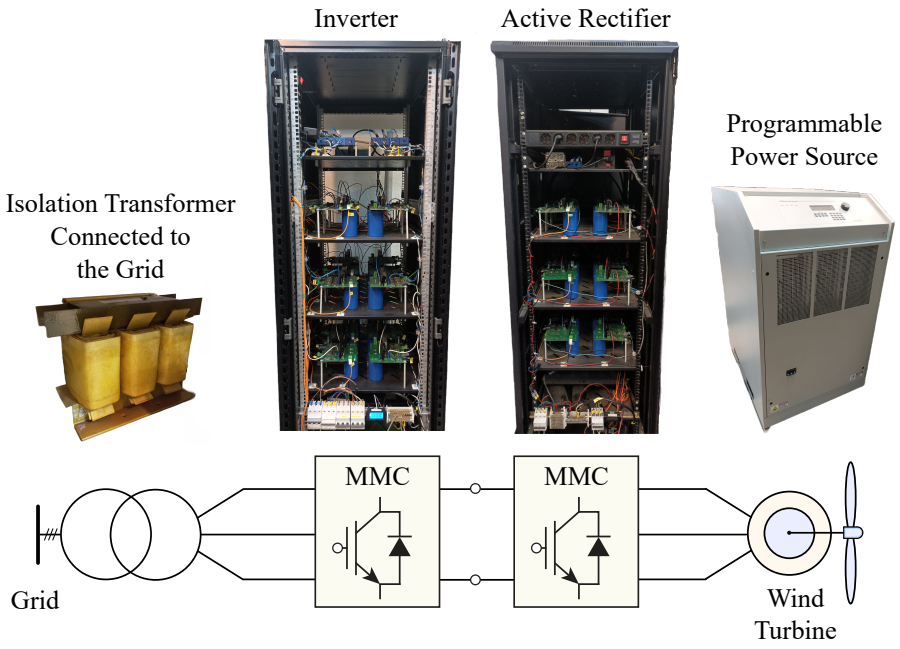

Figure 4.5: Experimental setup.

experimental prototype is performed (including converter losses), using a PLECS-RT system controlled by the dSPACE MicroLabBox platform. The HIL results are shown in Fig. 4.6. Further details regarding the HIL methodology are discussed in [62, 88].

For $t < 1$ s the PMSG is operated at 10.67 Hz, with an output of 300 W. Between 1 s $\leq t \leq$ 8.5 s a ramp variation in the generator speed is produced and the power output is increased to 5 kW when the frequency reaches 26.67 Hz. The DC-link voltage changes from 312 V to 340 V. Notice that at low frequencies the CVOs are slightly reduced. This reduction is a result of the approximations realised to obtain (4.17)-(4.18), (see Section 4.3.3), where losses are neglected. However, this small reduction in $|\boldsymbol{v}^{\Delta}_{C\alpha\beta}|$ is not considered important in this work because it does not affect much the performance of the proposed CCS-MPC algorithm.

4.4.2. Variable-Speed Operation

To emulate the operation of a PMSG-based variable-speed wind turbine, the 180-second wind speed profile shown in Fig. 4.7 is used to obtain the frequency and voltage profiles of the 10 MW direct-drive PMSG of the WECS reported in [75]. As mentioned earlier, the results are scaled down and stored in the programmable power supply that emulates the PMSG.

Fig. 4.8(a) illustrates the CVOs for the six clusters of the grid-side MMC. The reference $\bar{v}_c^* \approx 350$ V for each cluster and the 6 % is ≈ 21 V. Notice that the CVOs are well within the 6 % voltage range (around 330 V to 370 V). This performance is made possible by the proposed CCS-MPC, which effectively regulates the CVOs using the DC-link voltage [see Fig. 4.8(b)] and the common-mode voltage [see Fig. 4.8(c)], without the need for circulating currents, as demonstrated in Fig. 4.8(d). These control features have been extensively discussed in Sections 4.3.3.1 and 4.3.3.3.

Fig. 4.8(e) shows the currents in each cluster, which consist of the generator currents shown in Fig. 4.8(f) and the DC port current in Fig. 4.8(g). Notice that the total current in the cluster is small during low-frequency operation due to the lack of circulating currents,

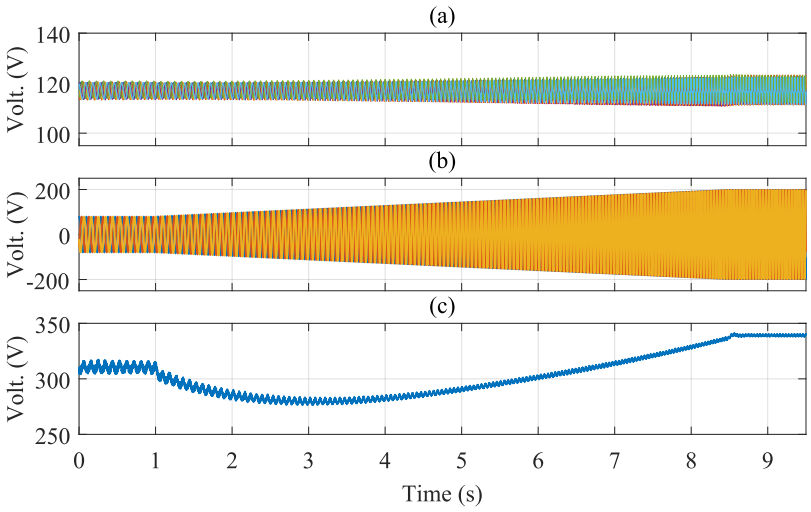

Figure 4.6: Hardware-in-the-Loop results of voltage and frequency ramp testing on the generator from minimum power (≈ 300 W) to rated power, with a 6 % capacitor oscillation band. (a) Capacitor Voltages v_{Ca1}^{P}, v_{Ca2}^{P}, etc., (b) Generator Voltages, and (c) DC-link Voltage.

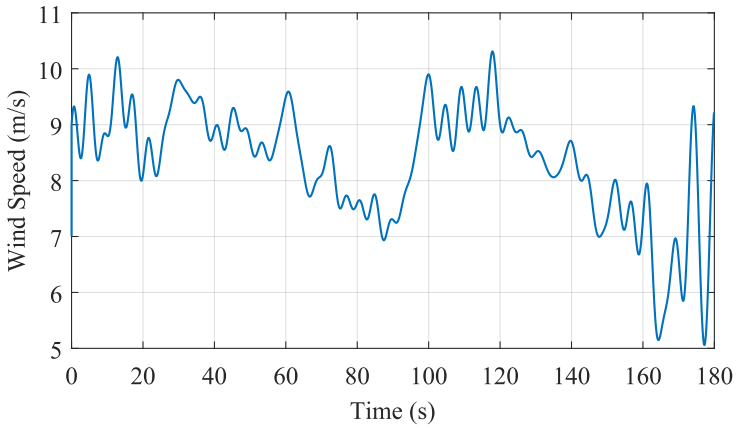

Figure 4.7: Wind profile used in the experimental test.

which are usually large in conventional control methods[10, 12], when compensating large low-frequency CVOs. The direct current at the PCC, between the hybrid-MMC and the PMSG, is regulated using (4.13), as depicted in Fig. 4.8(f), where a peak current of 17 A and unity power factor are achieved. The PMSG generated power is illustrated in Fig. 4.8(h), reaching a peak power of 5 kW at $t = 120$ s, which corresponds to the moment when the maximum stator electrical frequency of 26.67 Hz is attained. Additionally, the peak voltage v_{dmax} [see Fig. 4.8(i)] is also reached at $t = 120$ s.

4.4.3. Fixed-Speed Operation

To demonstrate the performance of the proposed CCS-MPC algorithm, an experimental test is conducted, emulating a significant power perturbation at the lowest achievable frequency using the programmable power supply. The experimental results are depicted in Fig. 4.9.

At $t < 3$ s the emulated PMSG operates with an output power of 1 kW, an electrical

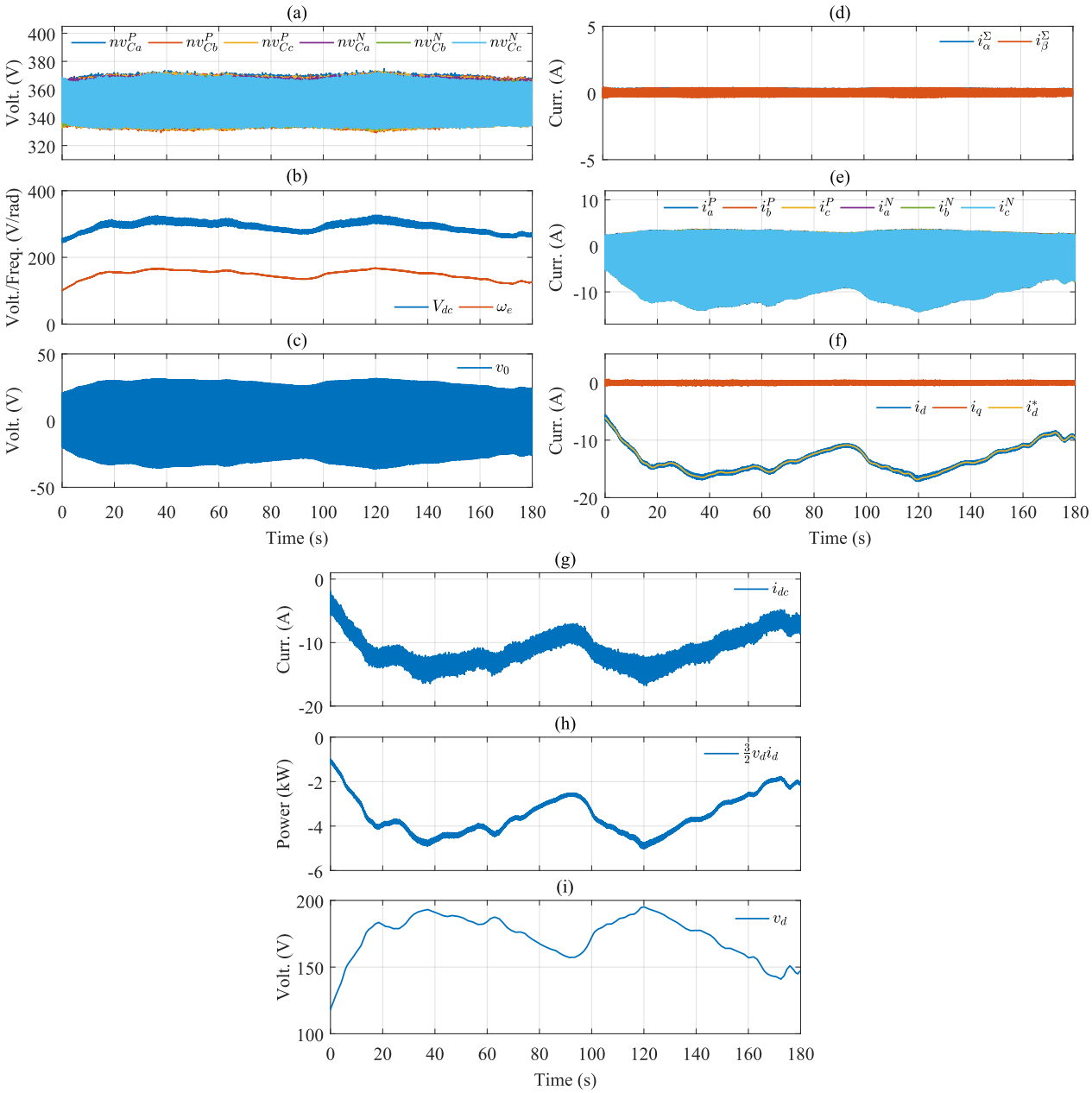

Figure 4.8: Experimental results for variable speed operation. (a) Cluster capacitor voltages, (b) DC-link voltage and generator frequency, (c) Common-mode voltage, (d) Circulating currents, (e) Cluster currents, (f) Generator currents, (g) DC port current, (h) Generated Active Power, and (i) Generator voltage.

frequency of 16 Hz, a voltage of $v_d \approx 118$ V at the PCC, and a 6 % for $|\boldsymbol{v}_{C\alpha\beta}^{\Delta}|$. At $t = 0.3$ s, a step of ≈ 1 kW is applied [see Fig. 4.9(f)] to the power generated by the PMSG, while maintaining the same operating frequency. As depicted in Fig. 4.9(a), after a short transient, the capacitor voltages remain within the 6 % voltage oscillation band before and after the power step. Additionally, the magnitude of the DC link current increases [see Fig. 4.9(b)] as a consequence of the step-up change in the peak generator current [see Fig. 4.9(c)]. However, as indicated by (4.17), the higher magnitude of i_d, reduces the value of $\bar{V}_{dc}$ used as a reference in the vector $\boldsymbol{u}^*$ utilised in the cost function [see (4.9)] and in (4.28). Consequently, the CCS-

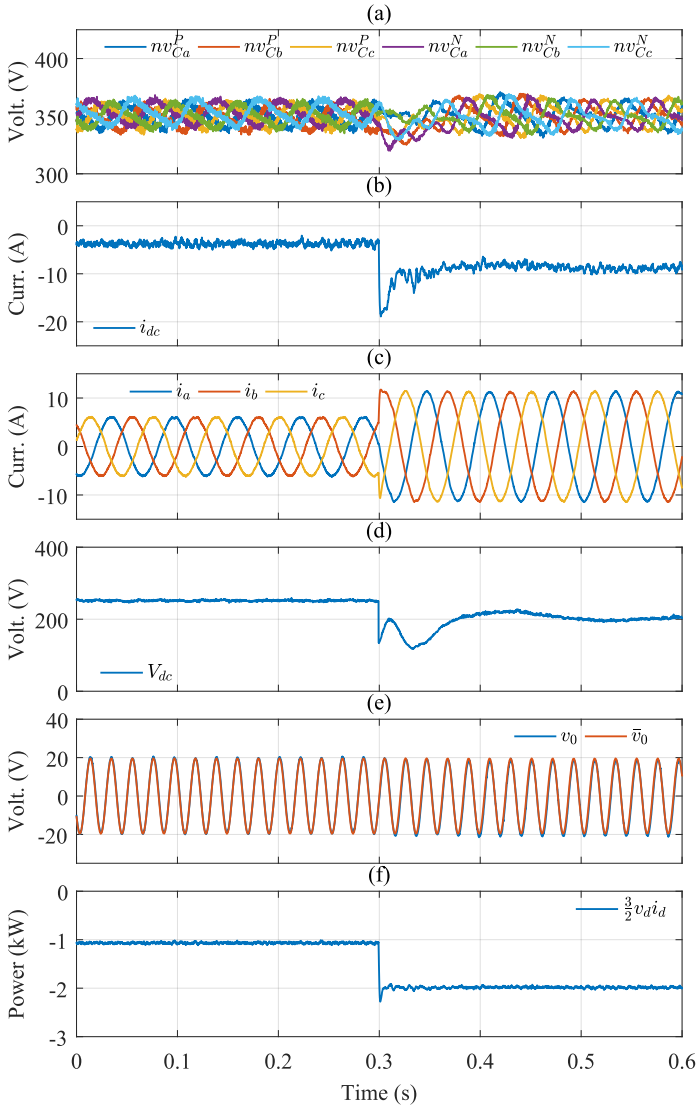

Figure 4.9: Experimental results for active power step when the generator operates at constant frequency and voltage. (a) Cluster capacitor voltages, (b) DC port current, (c) Generator currents, (d) DC-link voltage, (e) Common-mode voltage, and (f) Generated Active Power.

MPC algorithm lowers the DC-link voltage, leading to a new steady-state operating point after a brief transient, with a new output power of 2 kW. Fig. 4.9(e) presents the tracking of the common-mode voltage and its reference $\bar{v}_0$ [see (4.23)]. The tracking is almost perfect with a very small difference after the power step. This feature is one of the advantages of the proposed CCS-MPC, as it improves the modulation index throughout the entire operating range.

Fig. 4.10 shows the frequency spectrum of the voltage v_0 synthesised by the generator-side converter in steady-state, after the power step. As aforementioned, the largest component is the third harmonic, which is required to compensate the CVOs produced by the term $(\boldsymbol{v}_{\alpha\beta}\boldsymbol{i}_{\alpha\beta})^c$ in (4.6)(a). However, there are two smaller frequency components. A dc component, which is produced by the CCS-MPC algorithm, to compensate the capacitor voltage drift in (4.6)(c) and also a fundamental frequency component which is required to compensate the capacitor voltage drift in (4.6)(a). Notice that the last two components are automatically introduced by the CCS-MPC. Unlike linear control system of MMCs[10, 12, 79], in the

proposed CCS-MPC, it is not necessary to predefine the shape, frequency and phase-shift of the required control actions.

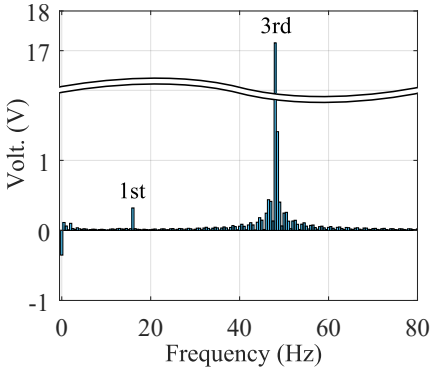

Figure 4.10: FFT analysis of the common-mode voltage synthesised by the proposed CCS-MPC control actions for steady state operation.

4.5. Conclusions

This paper has discussed a Continuous Control Set Model Predictive Control of a hybrid Modular Multilevel Converter driving a direct drive Permanent Magnet Synchronous Generator for variable speed wind energy applications. The outputs of the CCS-MPC algorithm are the common-mode and the dc-link voltages. The control system enables the operation of the CVOs within a predetermined range, facilitating the grid-side converter to function at a higher DC-link voltage and thereby reducing the required DC-link current. Furthermore, it has been experimentally demonstrated in this work that the reference for the common-mode voltage, obtained using an algorithm based on the Moore-Penrose pseudo-inverse matrix, is a third harmonic waveform which can be used to balance the capacitor voltages, as well as increasing the modulation index.

The proposed control system has been validated experimentally using an experimental system composed of two 5 kW hybrid-MMCs in a back-to-back configuration. Using a direct-drive PMSG emulated using a programmable power supply, the CCS-MPC algorithm discussed in this work has been tested considering variable-speed operation, using a wind profile, and also considering fixed-speed operation. Moreover, hardware in the loop validation has been used to verify the performance of the control system at frequencies lower than that achievable with the Ametek power supply. The CCS-MPC algorithm demonstrated excellent performance across all the conducted tests and considering the whole operating range.

Chapter 5

Conclusions

5.1. General Conclusions and Future Work

The following section presents a set of comprehensive conclusions derived from an extensive doctoral project focused on the development and implementation of control strategies for MMC-based drives. Throughout this research, several papers have been produced, addressing various challenges and advancements in MMC control methodologies. The conclusions encompass key findings related to the effectiveness of the proposed two-stage CCS-MPC strategy for regulating capacitor voltages and circulating currents, achieving optimal saturation, and the automatic determination of circulating current characteristics. Additionally, the analysis covers the successful regulation of capacitor voltages under different frequency conditions, the potential for one-stage CCS-MPC implementation, and the possibility of voltage balancing and oscillation mitigation without the use of circulating currents.

These findings offer valuable insights into the control of MMC-based systems, suggesting potential avenues for further research and advancements in this area of study. Moreover, the section will also discuss potential avenues for future work in exploring and refining the presented control strategies, aiming to further enhance the performance and efficiency of MMC-based drives in diverse applications.

5.1.1. Conclusions

1. The two-stage CCS-MPC strategy developed in this work (Chapter 2) demonstrates that the power-voltage and voltage-current models of the MMC can be effectively used to regulate capacitor voltages and circulating current references, while considering current and voltage constraints. This supports hypothesis 1, indicating that the power-voltage and voltage-current models are utilised to develop the CCS-MPC for regulating capacitor voltages and circulating currents with constraints.

2. The proposed CCS-MPC algorithm simplifies saturation control and achieves optimal saturation of currents and voltages in the MMC, as evidenced by experimental results in the context of Chapter 2. This result supports hypothesis 2, which suggests that CCS-MPC can achieve optimal saturation that is challenging with SISO-based anti-windup algorithms, as independent limiting of components may not fully exploit or properly limit the cluster current or voltage.

3. The CCS-MPC algorithm presented in Chapter 2 automatically determines the waveform, phase, and sequence of circulating currents without predefined parameters. This

conclusion confirms hypothesis 3, stating that the algorithm can adjust circulating currents automatically in response to changes in the common-mode voltage waveform or output port frequency, without modifying the control system.

4. By using an external controller to modify the weighting factors associated with the CCS-MPC controlling capacitor oscillations, it is possible to regulate capacitor voltages within an acceptable range, even at low frequencies. Additionally, the weight factor controller enables the same control strategy to be applied for both high and low frequencies without requiring a predefined transition method between regions. This aligns with hypothesis 4, highlighting the capability of the CCS-MPC to regulate capacitor voltage fluctuations and provide a smooth transition between different frequency regions.

5. The enhanced single-stage CCS-MPC algorithm developed in Chapter 3 shows that it is feasible to implement a one-stage CCS-MPC that handles capacitor voltages and circulating currents in a single optimisation problem. This reduces the computational burden compared to the two-stage CCS-MPC approach. Thus, this conclusion supports hypothesis 5, which suggests that the one-stage CCS-MPC is capable of handling both dynamics and constraints in a single cost function.

6. The CCS-MPC approach proposed for a hybrid-MMC driving a direct-drive PMSG in variable speed wind energy applications (Chapter 4) indicates that voltage balancing and voltage oscillation mitigation in capacitors can be achieved without using circulating currents. This conclusion directly supports hypothesis 6, which states that it is feasible to achieve voltage balancing and mitigate voltage oscillations without relying on circulating currents in the MMC control strategy.

5.1.2. Future Work

Based on the results obtained in this thesis, the following are some interesting topics for further research that can expand the scope of this doctoral project. These topics were partially explored during the doctoral project but still require more work or have not been fully explored yet.

1. Develop a power model for the converter that allows including common-mode voltage as a control action along with the circulating currents within the MPC. This enhancement aims to optimise the utilisation of available voltages in the MMC clusters effectively.

2. Since it is possible to obtain an unconstrained solution to the optimisation problems posed in this thesis, conducting an analysis of the closed-loop transfer function could be beneficial. In this analysis, the weighting factors of the cost function can be treated as unknowns, allowing for tuning these weights based on the closed-loop response.

3. Similarly, the placement of poles in the closed-loop transfer function can be used to ensure system stability when employing a CCS-MPC-based strategy, particularly when the constraints are inactive.

4. Analyse how the proposed control strategy for the hybrid-MMC impacts the design and performance of the converter connected to the grid.

5. Increase the number of controlled states by the CCS-MPC and incorporate integral control to achieve zero steady-state error for AC and DC port currents while maintaining the use of constraints, which is one of the principal advantages of MPC.

6. Increase the prediction horizon of the CCS-MPC and evaluate the computational burden and performance improvement of the control strategies.

Addressing these areas of future research can further advance the field of MMC-based drives, leading to improved control strategies and enhancing the overall performance and efficiency of MMC systems in various applications.

Bibliography

[1] Perez, M. A., Ceballos, S., Konstantinou, G., Pou, J., y Aguilera, R. P., "Modular multilevel converters: Recent achievements and challenges," IEEE Open Journal of the Industrial Electronics Society, vol. 2, pp. 224–239, 2021.

[2] Akagi, H., "Multilevel converters: Fundamental circuits and systems," Proceedings of the IEEE, vol. 105, no. 11, pp. 2048–2065, 2017.

[3] Guo, G., Song, Q., Zhao, B., Rao, H., Xu, S., Zhu, Z., y Liu, W., "Series-connected-based offshore wind farms with full-bridge modular multilevel converter as grid- and generator-side converters," IEEE Transactions on Industrial Electronics, vol. 67, no. 4, pp. 2798–2809, 2020.

[4] Dekka, A., Wu, B., Yaramasu, V., Fuentes, R. L., y Zargari, N. R., "Model Predictive Control of High-Power Modular Multilevel Converters - An Overview," IEEE Journal of Emerging and Selected Topics in Power Electronics, vol. 7, pp. 168–183, 2019.

[5] Soto-Sanchez, D. E., Pena, R., Cardenas, R., Clare, J., y Wheeler, P., "A cascade multilevel frequency changing converter for high-power applications," IEEE Transactions on Industrial Electronics, vol. 60, no. 6, pp. 2118–2130, 2013.

[6] Sun, P., Tian, Y., Pou, J., y Konstantinou, G., "Beyond the mmc: Extended modular multilevel converter topologies and applications," IEEE Open Journal of Power Electronics, vol. 3, pp. 317–333, 2022.

[7] Rojas, F., Jerez, C., Hackl, C. M., Kalmbach, O., Pereda, J., y Lillo, J., "Faults in modular multilevel cascade converters-part ii: Fault tolerance, fault detection and diagnosis, and system reconfiguration," IEEE Open Journal of the Industrial Electronics Society, vol. 3, pp. 594–614, 2022.

[8] Dekka, A., Wu, B., Fuentes, R. L., Perez, M., y Zargari, N. R., "Evolution of Topologies, Modeling, Control Schemes, and Applications of Modular Multilevel Converters," IEEE Journal of Emerging and Selected Topics in Power Electronics, vol. 5, pp. 1631–1656, 2017.

[9] Hagiwara, M., Hasegawa, I., y Akagi, H., "Start-up and low-speed operation of an electric motor driven by a modular multilevel cascade inverter," IEEE Transactions on Industry Applications, vol. 49, no. 4, pp. 1556–1565, 2013.

[10] Espinoza, M., Cárdenas, R., Díaz, M., y Clare, J. C., "An Enhanced dq-Based Vector Control System for Modular Multilevel Converters Feeding Variable-Speed Drives," IEEE Transactions on Industrial Electronics, vol. 64, pp. 2620–2630, 2017.

[11] Espinoza-B, M., Cardenas, R., Clare, J., Soto-Sanchez, D., Diaz, M., Espina, E., y Hackl, C. M., "An integrated converter and machine control system for MMC-based high-power

drives," IEEE Transactions on Industrial Electronics, vol. 66, pp. 2343–2354, 2019.

[12] Kammerer, F., Gommeringer, M., Kolb, J., y Braun, M., "Energy balancing of the modular multilevel matrix converter based on a new transformed arm power analysis," en 2014 16th European Conference on Power Electronics and Applications, pp. 1–10, 2014.

[13] Hagiwara, M., Nishimura, K., y Akagi, H., "A medium-voltage motor drive with a modular multilevel pwm inverter," IEEE Transactions on Power Electronics, vol. 25, pp. 1786–1799, 2010.

[14] Korn, A. J., Winkelnkemper, M., y Steimer, P., "Low output frequency operation of the Modular Multi-Level Converter," en 2010 IEEE Energy Conversion Congress and Exposition, pp. 3993–3997, 2010.

[15] Kolb, J., Kammerer, F., Gommeringer, M., y Braun, M., "Cascaded control system of the modular multilevel converter for feeding variable-speed drives," IEEE Transactions on Power Electronics, vol. 30, no. 1, pp. 349–357, 2015.

[16] Urrutia, M., Cardenas, R., Clare, J., y Watson, A., "Circulating Current Control for the Modular Multilevel Matrix Converter Based on Model Predictive Control," IEEE Journal of Emerging and Selected Topics in Power Electronics, vol. 9, pp. 6069–6085, 2021.

[17] Espinoza, M., Cárdenas, R., Díaz, M., Mora, A., y Soto, D., "Modelling and control of the modular multilevel converter in back to back configuration for high power induction machine drives," en IECON 2016 - 42nd Annual Conference of the IEEE Industrial Electronics Society, pp. 5046–5051, 2016.

[18] Münch, P., Görges, D., Izák, M., y Liu, S., "Integrated current control, energy control and energy balancing of modular multilevel converters," en IECON 2010 - 36th Annual Conference on IEEE Industrial Electronics Society, pp. 150–155, 2010.

[19] Fuchs, S., Jeong, M., y Biela, J., "Long Horizon, Quadratic Programming Based Model Predictive Control (MPC) for Grid Connected Modular Multilevel Converters (MMC)," IECON Proceedings (Industrial Electronics Conference), pp. 1805–1812, 2019.

[20] Kouro, S., Perez, M. A., Rodriguez, J., Llor, A. M., y Young, H. A., "Model predictive control: Mpc's role in the evolution of power electronics," IEEE Industrial Electronics Magazine, vol. 9, pp. 8–21, 2015.

[21] Mora, A., Urrutia, M., Cárdenas, R., Angulo, A., Espinoza, M., Díaz, M., y Lezana, P., "Model-predictive-control-based capacitor voltage balancing strategies for modular multilevel converters," IEEE Transactions on Industrial Electronics, vol. 66, no. 3, pp. 2432–2443, 2019.

[22] Du, S., Dekka, A., Wu, B., y Zargari, N., Modular multilevel converters: analysis, control, and applications. John Wiley & Sons, 2018.

[23] Poorfakhraei, A., Narimani, M., y Emadi, A., "A Review of Modulation and Control Techniques for Multilevel Inverters in Traction Applications," IEEE Access, vol. 9, pp. 24187–24204, 2021.

[24] Papafotiou, G. A., Demetriades, G. D., y Agelidis, V. G., "Technology readiness assessment of model predictive control in medium- and high-voltage power electronics," IEEE Transactions on Industrial Electronics, vol. 63, pp. 5807–5815, 2016.

[25] Mirsaeidi, S., Tzelepis, D., He, J., Dong, X., Said, D. M., y Booth, C., "A Controllable Thyristor-Based Commutation Failure Inhibitor for LCC-HVDC Transmission Systems," IEEE Transactions on Power Electronics, vol. 36, no. 4, pp. 3781–3792, 2021.

[26] Stan, A., Costinaș, S., y Ion, G., "Overview and Assessment of HVDC Current Applications and Future Trends," Energies, vol. 15, no. 3, 2022, https://www.mdpi.com/1996-1073/15/3/1193.

[27] Lee, Y., Cui, S., Kim, S., y Sul, S.-K., "Control of hybrid HVDC transmission system with LCC and FB-MMC," en 2014 IEEE Energy Conversion Congress and Exposition (ECCE), pp. 475–482, 2014.

[28] Wu, B., Pontt, J., Rodriguez, J., Bernet, S., y Kouro, S., "Current-Source Converter and Cycloconverter Topologies for Industrial Medium-Voltage Drives," IEEE Transactions on Industrial Electronics, vol. 55, no. 7, pp. 2786–2797, 2008.

[29] Luan, K., Li, Y., Li, Z., Xia, B., Zhao, C., Xu, F., Gao, F., y Wang, P., "Analysis and Design of PWM-CSC for HVDC Transmission Systems," en IECON 2019 - 45th Annual Conference of the IEEE Industrial Electronics Society, vol. 1, pp. 4773–4777, 2019.

[30] Torres-Olguin, R. E., Molinas, M., y Undeland, T., "Offshore Wind Farm Grid Integration by VSC Technology With LCC-Based HVDC Transmission," IEEE Transactions on Sustainable Energy, vol. 3, no. 4, pp. 899–907, 2012.

[31] Xue, Y., Zhang, X.-P., y Yang, C., "AC Filterless Flexible LCC HVDC With Reduced Voltage Rating of Controllable Capacitors," IEEE Transactions on Power Systems, vol. 33, no. 5, pp. 5507–5518, 2018.

[32] Sharifabadi, K., Harnefors, L., Nee, H.-P., Norrga, S., y Teodorescu, R., Design, control, and application of modular multilevel converters for HVDC transmission systems. John Wiley & Sons, 2016.

[33] Nakanishi, T. y Itoh, J.-I., "High Power Density Design for a Modular Multilevel Converter With an H-Bridge Cell Based on a Volume Evaluation of Each Component," IEEE Transactions on Power Electronics, vol. 33, no. 3, pp. 1967–1984, 2018.

[34] Diaz, M., Cárdenas Dobson, R., Ibaceta, E., Mora, A., Urrutia, M., Espinoza, M., Rojas, F., y Wheeler, P., "An Overview of Applications of the Modular Multilevel Matrix Converter," Energies, vol. 13, no. 21, 2020, https://www.mdpi.com/1996-1073/13/21/5546.

[35] Siemens, "Sinamics perfect harmony gh150." https://new.siemens.com/global/en/products/drives/sinamics/medium-voltage-converters/sinamics-perfect-harmony-gh150.html, 2019. Accessed: July 2023.

[36] Benshaw, "M2l series." https://www.benshaw.com/, 2019. Accessed: July 2023.

[37] Okazaki, Y., Kawamura, W., Hagiwara, M., Akagi, H., Ishida, T., Tsukakoshi, M., y Nakamura, R., "Experimental comparisons between modular multilevel dscc inverters and tsbc converters for medium-voltage motor drives," IEEE Transactions on Power Electronics, vol. 32, no. 3, pp. 1805–1817, 2017.

[38] Antonopoulos, A., Ängquist, L., Norrga, S., Ilves, K., Harnefors, L., y Nee, H.-P., "Modular Multilevel Converter AC Motor Drives With Constant Torque From Zero to Nominal Speed," IEEE Transactions on Industry Applications, vol. 50, no. 3, pp. 1982–1993, 2014.

[39] Debnath, S., Qin, J., y Saeedifard, M., "Control and Stability Analysis of Modular Multilevel Converter Under Low-Frequency Operation," IEEE Transactions on Industrial Electronics, vol. 62, no. 9, pp. 5329–5339, 2015.

[40] Li, B., Zhou, S., Xu, D., Yang, R., Xu, D., Buccella, C., y Cecati, C., "An Improved Circulating Current Injection Method for Modular Multilevel Converters in Variable-Speed Drives," IEEE Transactions on Industrial Electronics, vol. 63, pp. 7215–7225, 2016.

[41] Gao, X., Tian, W., Pang, Y., y Kennel, R., "Model Predictive Control for Modular Multilevel Converters Operating at Wide Frequency Range with a Novel Cost Function," IEEE Transactions on Industrial Electronics, pp. 1–1, 2021.

[42] Lesnicar, A. y Marquardt, R., "An innovative modular multilevel converter topology suitable for a wide power range," en 2003 IEEE Bologna PowerTech - Conference Proceedings, vol. 3, pp. 6–11, 2003.

[43] Perez, M. A., Bernet, S., Rodriguez, J., Kouro, S., y Lizana, R., "Circuit Topologies, Modeling, Control Schemes, and Applications of Modular Multilevel Converters," IEEE Transactions on Power Electronics, vol. 30, pp. 4–17, 2015.

[44] Geyer, T., Model predictive control of high power converters and industrial drives. Wiley & Sons, 1 ed., 2016.

[45] Quevedo, D. E., Aguilera, R. P., y Geyer, T., Predictive Control in Power Electronics and Drives: Basic Concepts, Theory, and Methods, cap. 5, pp. 181–226. Cham: Springer International Publishing, 2014.

[46] Liu, P., Wang, Y., Cong, W., y Lei, W., "Grouping-sorting-optimized model predictive control for modular multilevel converter with reduced computational load," IEEE Transactions on Power Electronics, vol. 31, pp. 1896–1907, 2016.

[47] Guo, P., He, Z., Yue, Y., Xu, Q., Huang, X., Chen, Y., y Luo, A., "A novel two-stage model predictive control for modular multilevel converter with reduced computation," IEEE Transactions on Industrial Electronics, vol. 66, pp. 2410–2422, 2019.

[48] Yin, J., Leon, J. I., Perez, M. A., Franquelo, L. G., Marquez, A., y Vazquez, S., "Model predictive control of modular multilevel converters using quadratic programming," IEEE Transactions on Power Electronics, vol. 36, pp. 7012–7025, 2021.

[49] Wang, J., Liu, X., Xiao, Q., Zhou, D., Qiu, H., y Tang, Y., "Modulated model predictive control for modular multilevel converters with easy implementation and enhanced steady-state performance," IEEE Transactions on Power Electronics, vol. 35, pp. 9107–9118, 2020.

[50] Nocedal, J. y Wright, S., Numerical Optimization. New York, NY: Springer, 2. ed. ed., 2006.

[51] Li, B., Zhou, S., Xu, D., Xu, D., y Wang, W., "Comparative study of the sinusoidal-wave and square-wave circulating current injection methods for low-frequency operation of the modular multilevel converters," en 2015 IEEE Energy Conversion Congress and Exposition (ECCE), pp. 4700–4705, 2015.

[52] Xu, J., Zhao, C., Xiong, Y., Li, C., Ji, Y., y An, T., "Optimal design of mmc levels for electromagnetic transient studies of mmc-hvdc," IEEE Transactions on Power Delivery, vol. 31, no. 4, pp. 1663–1672, 2016.

[53] Oates, C., "Modular multilevel converter design for vsc hvdc applications," IEEE Journal of Emerging and Selected Topics in Power Electronics, vol. 3, no. 2, pp. 505–515, 2015.

[54] Ferreau, H. J., Bock, H. G., y Diehl, M., "An online active set strategy to overcome the limitations of explicit mpc," International Journal of Robust and Nonlinear Control, vol. 18, no. 8, pp. 816–830, 2008.

[55] Cimini, G. y Bemporad, A., "Exact complexity certification of active-set methods for quadratic programming," IEEE Transactions on Automatic Control, vol. 62, no. 12, pp. 6094–6109, 2017.

[56] Cimini, G., Bernardini, D., Levijoki, S., y Bemporad, A., "Embedded model predictive control with certified real-time optimization for synchronous motors," IEEE Transactions on Control Systems Technology, vol. 29, no. 2, pp. 893–900, 2021.

[57] Kouvaritakis, B. y Cannon, M., Model Predictive Control: Classical, Robust and Stochastic. Springer International Publishing, 1 ed., 2015.

[58] Cortes, P., Rodriguez, J., Silva, C., y Flores, A., "Delay compensation in model predictive current control of a three-phase inverter," IEEE Transactions on Industrial Electronics, vol. 59, pp. 1323–1325, 2012.

[59] Marquardt, R., "Modular multilevel converter: An universal concept for hvdc-networks and extended dc-bus-applications," en The 2010 International Power Electronics Conference, pp. 502–507, 2010.

[60] Sehloff, D. y Roald, L. A., "Low frequency ac transmission upgrades with optimal frequency selection," IEEE Transactions on Power Systems, vol. 37, no. 2, pp. 1437–1448, 2022.

[61] Zhao, F., Xiao, G., Zhu, T., Zheng, X., Wu, Z., y Zhao, T., "A Coordinated Strategy of Low-Speed and Start-Up Operation for Medium-Voltage Variable-Speed Drives With a Modular Multilevel Converter," IEEE Transactions on Power Electronics, vol. 35, no. 1, pp. 709–724, 2020.

[62] Arias-Esquivel, Y., Cárdenas, R., Urrutia, M., Diaz, M., Tarisciotti, L., y Clare, J. C., "Continuous control set model predictive control of a modular multilevel converter for drive applications," IEEE Transactions on Industrial Electronics, vol. 70, no. 9, pp. 8723–8733, 2023.

[63] Gao, X., Tian, W., Pang, Y., y Kennel, R., "Model-predictive control for modular multilevel converters operating at wide frequency range with a novel cost function," IEEE Transactions on Industrial Electronics, vol. 69, no. 6, pp. 5569–5580, 2022.

[64] Rodriguez, J., Garcia, C., Mora, A., Davari, S. A., Rodas, J., Valencia, D. F., Elmorshedy, M., Wang, F., Zuo, K., Tarisciotti, L., Flores-Bahamonde, F., Xu, W., Zhang, Z., Zhang, Y., Norambuena, M., Emadi, A., Geyer, T., Kennel, R., Dragicevic, T., Khaburi, D. A., Zhang, Z., Abdelrahem, M., y Mijatovic, N., "Latest advances of model predictive control in electrical drives—part ii: Applications and benchmarking with classical control methods," IEEE Transactions on Power Electronics, vol. 37, no. 5, pp. 5047–5061, 2022.

[65] Gao, X., Pang, Y., Xia, J., Chai, N., Tian, W., Rodriguez, J., y Kennel, R., "Modulated model predictive control of modular multilevel converters operating in a wide frequency range," IEEE Transactions on Industrial Electronics, pp. 1–12, 2022.

[66] Poblete, P., Neira, S., Aguilera, R. P., Pereda, J., y Pou, J., "Sequential phase-shifted model predictive control for modular multilevel converters," IEEE Transactions on Energy Conversion, vol. 36, no. 4, pp. 2691–2702, 2021.

[67] Cuzmar, R. H., Pereda, J., y Aguilera, R. P., "Phase-shifted model predictive control to achieve power balance of chb converters for large-scale photovoltaic integration," IEEE Transactions on Industrial Electronics, vol. 68, no. 10, pp. 9619–9629, 2021.

[68] Karwatzki, D. y Mertens, A., "Generalized control approach for a class of modular multilevel converter topologies," IEEE Transactions on Power Electronics, vol. 33, no. 4, pp. 2888–2900, 2018.

[69] Rawlings, J. B., Mayne, D. Q., y Diehl, M. M., Model Predictive Control: Theory, Computation, and Design 2nd Edition. Nob Hill Publishing, LLC, 2 ed., 2017, http://www.nobhillpublishing.com.

[70] Askari, M., Moghavvemi, M., Almurib, H. A. F., y Haidar, A. M. A., "Stability of soft-constrained finite horizon model predictive control," IEEE Transactions on Industry Applications, vol. 53, no. 6, pp. 5883–5892, 2017.

[71] Cortes, P., Kouro, S., La Rocca, B., Vargas, R., Rodriguez, J., Leon, J. I., Vazquez, S., y Franquelo, L. G., "Guidelines for weighting factors design in model predictive control of power converters and drives," en 2009 IEEE International Conference on Industrial Technology, pp. 1–7, 2009.

[72] Graovac, D., "Mosfet power losses calculation using the datasheet parameters. infineon application note." https://application-notes.digchip.com/070/70-41484.pdf, 2019. Accessed: July 2023.

[73] REN21, "Renewables 2022 global status report." https://www.ren21.net/gsr-2022/, 2022. Accessed: July 2023.

[74] Debnath, S. y Saeedifard, M., "A new hybrid modular multilevel converter for grid connection of large wind turbines," IEEE Transactions on Sustainable Energy, vol. 4, no. 4, pp. 1051–1064, 2013.

[75] Polinder, H., Bang, D., van Rooij, R., McDonald, A., y Mueller, M., "10 mw wind turbine direct-drive generator design with pitch or active speed stall control," en 2007 IEEE International Electric Machines & Drives Conference, vol. 2, pp. 1390–1395, 2007.

[76] Htet, T. Z., Zhao, Z., y Gu, Q., "Design analysis of direct-driven pmsg in wind turbine application," en 2016 International Conference on System Reliability and Science (ICSRS), pp. 7–11, 2016.

[77] Basak, R., Bhuvaneswari, G., y Pillai, R. R., "Low-voltage ride-through of a synchronous generator-based variable speed grid-interfaced wind energy conversion system," IEEE Transactions on Industry Applications, vol. 56, no. 1, pp. 752–762, 2020.

[78] Arias-Esquivel, Y., Cárdenas, R., Tarisciotti, L., Díaz, M., y Mora, A., "A two-step continuous-control-set mpc for modular multilevel converters operating with variable output voltage and frequency," IEEE Transactions on Power Electronics, pp. 1–12, 2023.

[79] Kumar, Y. S. y Poddar, G., "Control of Medium-Voltage AC Motor Drive for Wide Speed Range Using Modular Multilevel Converter," IEEE Transactions on Industrial Electronics, vol. 64, pp. 2742–2749, 2017.

[80] Li, B., Zhou, S., Xu, D., Finney, S. J., y Williams, B. W., "A Hybrid Modular Multilevel Converter for Medium-Voltage Variable-Speed Motor Drives," IEEE Transactions on Power Electronics, vol. 32, pp. 4619–4630, 2017.

[81] Zhou, S., Li, B., Guan, M., Zhang, X., Xu, Z., y Xu, D., "Capacitance Reduction of the Hybrid Modular Multilevel Converter by Decreasing Average Capacitor Voltage in Variable-Speed Drives," IEEE Transactions on Power Electronics, vol. 34, pp. 1580–1594, 2019.

[82] Cárdenas, R., Espina, E., Clare, J., y Wheeler, P., "Self-tuning resonant control of a seven-leg back-to-back converter for interfacing variable-speed generators to four-wire loads," IEEE Transactions on Industrial Electronics, vol. 62, no. 7, pp. 4618–4629, 2015.

[83] Kumari, S., Kushwaha, V., y Gupta, T. N., "A maximum power point tracking for a pmsg based variable speed wind energy conversion system," en 2018 International Conference on Power Energy, Environment and Intelligent Control (PEEIC), pp. 789–794, 2018.

[84] Alzayed, M., Chaoui, H., y Farajpour, Y., "Maximum power tracking for a wind energy conversion system using cascade-forward neural networks," IEEE Transactions on Sustainable Energy, vol. 12, no. 4, pp. 2367–2377, 2021.

[85] Cardenas, R. y Pena, R., "Sensorless vector control of induction machines for variable-speed wind energy applications," IEEE Transactions on Energy Conversion, vol. 19, no. 1, pp. 196–205, 2004.

[86] Wu, B. y Narinami, M., High-Power Converters and AC Drives. USA: Wiley-IEEE Press, 2 ed., 2017.

[87] Bulder, B. H., Hendriks, H. B., Langen, P. v., Lindenburg, C., Snel, H., Bauer, P., Polinder, H., Rooij, R. v., Subroto, H., y Zaayer, M. B., "The icorass feasibility study," 2007.

[88] Burgos-Mellado, C., Zuñiga Bauerle, C., Muñoz Carpintero, D., Arias-Esquivel, Y., Cárdenas-Dobson, R., Dragičević, T., Donoso, F., y Watson, A., "Reinforcement learning-based method to exploit vulnerabilities of false data injection attack detectors in modular multilevel converters," IEEE Transactions on Power Electronics, vol. 38, no. 7, pp. 8907–8921, 2023.

[89] Lau, M. S. K., Yue, S. P., Ling, K. V., y Maciejowski, J. M., "A comparison of interior point and active set methods for FPGA implementation of model predictive control," en 2009 European Control Conference (ECC), pp. 156–161, 2009.

[90] Wu, B. y Narimani, M., Cascaded H-Bridge Multilevel Inverters, pp. 119–141. Wiley-IEEE Press, 2017.

Annexes

Annex A. Optimisation problem simplification

To clarify the simplifications made to the cost functions described in this thesis, this section presents the development of the substitutions of the equality constraints in the cost functions. The MPC formulation incorporates perturbations in the system dynamics and considers an equilibrium point different from zero to maintain generality. Additionally, the formulation is designed with a one-step prediction horizon, but it can be easily extended for longer horizons.

A.1. MPC Formulation

The complete MPC formulation is shown in (A.1), where $\mathbf{x}^*$ is the reference state and $\mathbf{u}^*$ is the equilibrium control action that brings the system to $\mathbf{x}^*$.

$$\begin{aligned} \min_{\mathbf{x}_{k+1},\mathbf{u}_k} \quad & (\mathbf{x}_{k+1}-\mathbf{x}^*)^T \mathbf{Q} (\mathbf{x}_{k+1}-\mathbf{x}^*) + (\mathbf{u}_k-\mathbf{u}^*)^T \mathbf{R} (\mathbf{u}_k-\mathbf{u}^*) \\ \text{s.t.} \quad & \mathbf{x}_{k+1} = \mathbf{A}\mathbf{x}_k + \mathbf{B}_k\mathbf{u}_k + \mathbf{d}_k \\ & \mathbf{G}\mathbf{u}_k \geq \mathbf{W} \end{aligned} \tag{A.1}$$

Substituting the equality constraint into the cost function yields the following optimisation problem:

$$\begin{aligned} \min_{\mathbf{u}_k} \quad & (\mathbf{A}x_k + \mathbf{B}_k\mathbf{u}_k + \mathbf{d}_k - \mathbf{x}^*)^T \mathbf{Q} (\mathbf{A}x_k + \mathbf{B}_k\mathbf{u}_k + \mathbf{d}_k - \mathbf{x}^*) + (\mathbf{u}_k-\mathbf{u}^*)^T \mathbf{R} (\mathbf{u}_k-\mathbf{u}^*) \\ \text{s.t.} \quad & \mathbf{G}\mathbf{u}_k \geq \mathbf{W} \end{aligned} \tag{A.2}$$

which can be simplified to

$$
\begin{aligned}
\min_{\mathbf{u}_k} \quad & \mathbf{u}_k^T \mathbf{B}_k^T \mathbf{Q} \mathbf{B}_k \mathbf{u}_k + \mathbf{u}_k^T \mathbf{R} \mathbf{u}_k + 2\left(\mathbf{d}_k^T \mathbf{Q} \mathbf{B}_k \mathbf{u}_k + \mathbf{x}_k^T \mathbf{A}^T \mathbf{Q} \mathbf{B}_k \mathbf{u}_k - \mathbf{x}^{*T} \mathbf{Q} \mathbf{B}_k \mathbf{u}_k - \mathbf{u}_k^{*T} \mathbf{R} \mathbf{u}_k\right) \\
& + \mathbf{x}_k^T \mathbf{A}^T \mathbf{Q} \mathbf{A} \mathbf{x}_k + \mathbf{d}_k^T \mathbf{Q} \mathbf{d}_k + \mathbf{x}^{*T} \mathbf{Q} \mathbf{x}^* + \mathbf{u}_k^{*T} \mathbf{R} \mathbf{u}_k^* + 2\left(\mathbf{d}_k^T \mathbf{Q} \mathbf{A} \mathbf{x}_k - \mathbf{x}_k^T \mathbf{A}^T \mathbf{Q} \mathbf{x}^* - \mathbf{d}_k^T \mathbf{Q} \mathbf{x}^*\right) \\
\text{s.t.} \quad & \mathbf{G} \mathbf{u}_k \geq \mathbf{W}
\end{aligned}
\tag{A.3}
$$

Note that (A.3) contains seven terms that are independent of the optimisation variable $\mathbf{u}_k$ (remarked in gray). Since these terms are constant for optimisation, they can be omitted in the cost function without affecting the result of the optimisation problem.

Annex B. Active-Set method

The active-set method has been widely utilised since the 1970s to address quadratic optimisation problems subject to linear constraints, which encompass both equality and inequality constraints. Generally, active-set methods demonstrate high efficiency when dealing with problems involving a limited number of optimisation variables and constraints. This distinguishes them from interior-point methods, which are often better suited for broader problems but can be more computationally intensive [50, 89]. Essentially, active-set methods offer significant advantages when addressing problems with a smaller number of variables and constraints.

This computational efficiency makes active-set methods particularly attractive for embedded model predictive control applications, as is the case with this thesis [55, 56]. Their computational performance aligns well with real-time implementations, where calculation speed is of utmost importance. This aspect has been evidenced in the research cited in the thesis, where the effectiveness of active-set methods in real-time scenarios has been highlighted.

A general quadratic optimisation problem can be written as follows:

$$
\begin{aligned}
\min_{u} \quad & \frac{1}{2} u^T H u + u^T f \\
\text{s.t.} \quad & Gu = W \\
& Gu \geq W
\end{aligned}
\tag{B.1}
$$

where H is a symmetric $n \times n$ positive semidefinite matrix, u and f are vectors in $\mathbb{R}^n$, G is a vector in $\mathbb{R}^m$, and W is an $m \times n$ matrix. In this optimisation problem, a value of u must be found such that the cost function is minimised and the equality and inequality constraints are satisfied.

The active-set method detailed in this proposal is an iterative algorithm that solves a quadratic subproblem at each iteration. This subproblem considers all the equality constraints and some of the inequality constraints. The inequality constraints are imposed as equalities in the optimisation subproblem. This subset of constraints is known as the working set ($\mathcal{V}_i$)

and must be updated at each iteration (i).

The active-set algorithm begins with an initial feasible solution u_0 (a solution vector that satisfies all the constraints), which does not necessarily have to be optimal. This initial solution is usually calculated by solving a linear optimisation; however, it can be obtained more easily depending on the problem's constraints. Additionally, although the initial working set can be created by evaluating which restrictions are active for u_0, this set is generally defined as $\mathcal{V}_0 = \emptyset$ by simplicity.

To solve the optimisation subproblem, the Karush–Kuhn–Tucker (KKT) matrix shown in equation (B.2) is used.

$$\begin{bmatrix} H & -G'^T \\ G' & 0 \end{bmatrix} \begin{bmatrix} \Delta p_i \\ \lambda_i \end{bmatrix} = \begin{bmatrix} -Hu_i - f \\ 0 \end{bmatrix} \tag{B.2}$$

where u_i is some estimate of the solution, Δp_i is a solution of this subproblem, λ_i is the vector of Lagrange multipliers, and G' are the constraints $\in \mathcal{V}_i$.

After solving the KKT matrix, it must be verified whether u_i is the solution to the global problem (B.1). Otherwise, equation (B.3) is used to compute a step-length parameter α_i that is chosen to be the largest value in the range [0, 1] for which all no-active constraints are satisfied.

$$\alpha_i = \min\left(1, \min_{\forall\, \{G,W\} \notin \mathcal{V}_i,\, G^T \Delta p_i < 0} \frac{W - G^T u_i}{G^T \Delta p_i}\right) \tag{B.3}$$

For each iteration, if $\Delta p_i = 0$ and $\lambda_i \geq 0$, it means that u_i is an optimal solution of (B.1) and the execution ends. Moreover, if $\Delta p_i \neq 0$ or $\lambda_i < 0$, u_i is not a global minimum and a new algorithm iteration has to be executed. When $\Delta p_i = 0$ and $\lambda_i < 0$, the next step is to remove the active constraint with a minimum Lagrange multiplier from $\mathcal{V}_i$ (to obtain $\mathcal{V}_{i+1}$) and start a new iteration using the same initial solution. If, on the contrary, $\Delta p_i \neq 0$, it is necessary to calculate a new estimated solution as follows:

$$u_{i+1} = u_i + \alpha_i \Delta p_i \tag{B.4}$$

Finally, $\mathcal{V}_{i+1}$ is obtained by adding the new active constraint (for u_{i+1}) to $\mathcal{V}_i$. A detailed description of the active-set algorithm is presented below, where u^* is the optimal solution.

Algorithm 1 High-level pseudo-code representation of the active-set algorithm [50].

Compute a feasible initial point u_0.
Set $\mathcal{V}_0 = \emptyset$.
$i \leftarrow 0$.
while *true* **do**
  Solve the KKT system (B.2).
  if $\Delta p_i = 0$ **then**
    if all the elements of $\lambda_i \geq 0$ **then**
      $u^* \leftarrow u_i$.
      break.
    else
      Remove from $\mathcal{V}_i$ the constraint corresponding to the minimum λ_i.
      $u_{i+1} \leftarrow u_i$.
      $\mathcal{V}_{i+1} \leftarrow \mathcal{V}_i$.
    end if
  else
    Compute α_i from (B.3).
    $u_{i+1} \leftarrow u_i + \alpha_i \Delta p_i$.
    Create $\mathcal{V}_{i+1}$ by adding the new active constraint.
  end if
  $i \leftarrow i + 1$.
end while

Annex C. Tuning the PI controller for online adaptation of cost function weights

Although there is not a strictly analytical relationship regarding how the weights λ_α^Δ and λ_β^Δ affect the magnitude of oscillations in the capacitors, some insights can be gained from the following equation:

$$nCv_C^* \frac{d\underline{v}_{C\alpha\beta}^\Delta}{dt} \approx \frac{1}{2} V_{dc} \underline{i}_{\alpha\beta} - \frac{2}{3} i_{dc} \underline{v}_{\alpha\beta} - 2v_0 \underline{i}_{\alpha\beta}^\Sigma \tag{C.1}$$

Or, in $d-q$ frame rotating at the frequency of the AC port (ω_e) and orientated along the voltage vector $\underline{v}_{C\alpha\beta}^\Delta$,

$$nCv_C^* \frac{dv_{Cd}^\Delta}{dt} \approx \frac{1}{2} V_{dc} i_d - \frac{2}{3} i_{dc} v_d - 2v_0 i_d^\Sigma \tag{C.2}$$

with this orientation, the imaginary component v_{Cq}^Δ can be neglected. Referring to (C.1), it can be observed that the magnitude of oscillations in the capacitors is directly influenced by the magnitude of the circulating current. Increasing the weights λ_α^Δ and λ_β^Δ, which penalise the oscillations in the capacitors, consequently leads to an increase in the circulating current.

Based on the analysis described above, tests were conducted as illustrated in Fig. C.1. These tests involved evaluating the overshoot and response time of the closed-loop system when applying current steps at the AC port, a scenario known for its demanding operational conditions. Through these comprehensive analyses, gains of Kp = 175 and Ki = 15600 were

meticulously chosen. The outcome of these selections is the closed-loop response depicted in Fig. C.1.

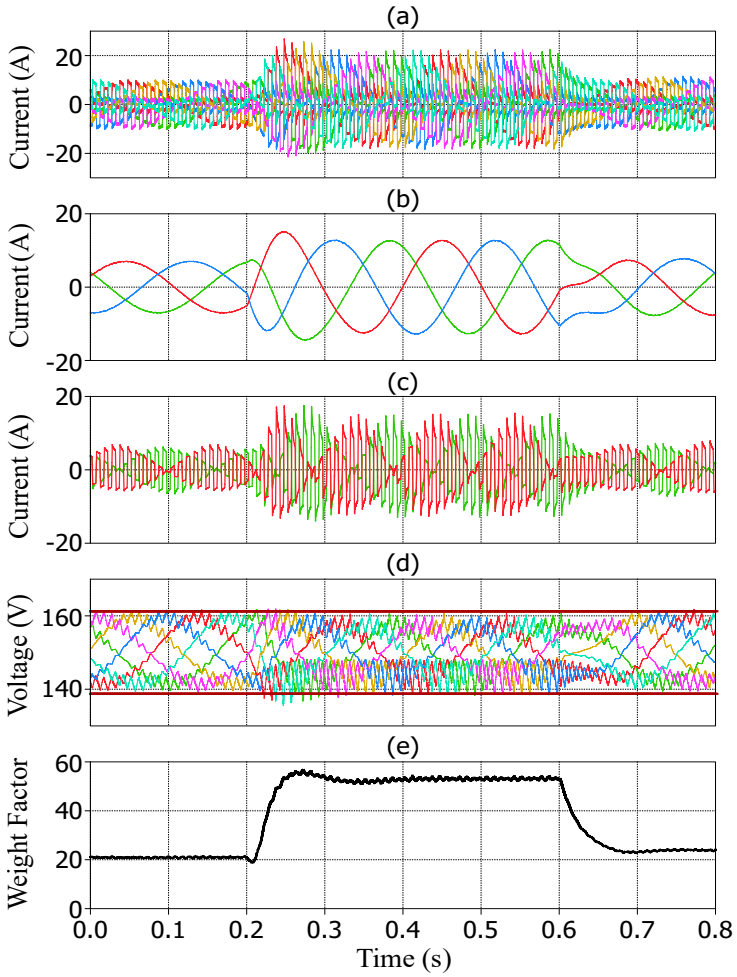

Figure C.1: HIL results of the weighting factor adapter using the PI controller. (a) Cluster current, (b) currents at the AC port, (c) circulating currents, (d) capacitor voltages, and (e) PI controller output.

Annex D. The conventional SISO-based control system used for comparison with the proposed Two-Stage CCS-MPC

The control scheme utilised in the comparison conducted in Chapter 2 is presented below. This scheme employs 9 linear controllers for reference calculation and control of circulating currents. For the reader's ease and for the completeness of this thesis, Fig. D.1 illustrates the control scheme used in [11]. However, specific details can be found in the original publication.

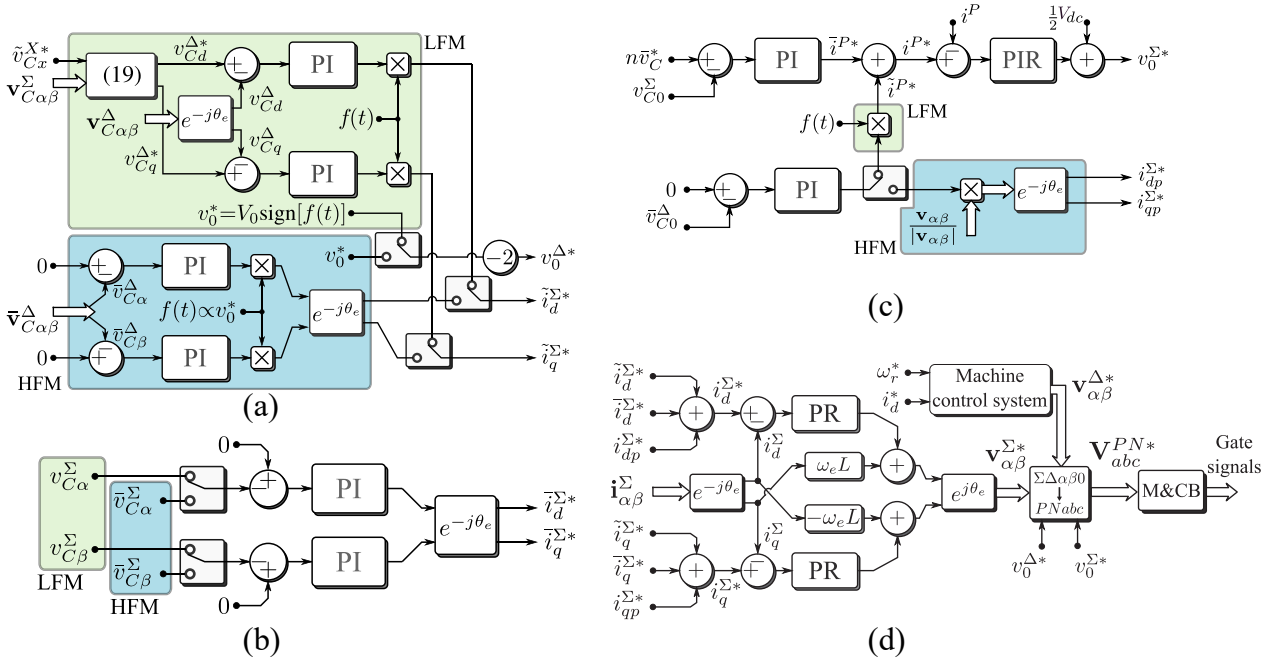

Figure D.1: Control scheme proposed in [11] for circulating current control. (a) Control of the vector $v^{\Delta}_{C\alpha\beta}$, (b) Control of the vector $v^{\Sigma}_{C\alpha\beta}$, (c) Control of the voltages v^{Σ}_{C0} and v^{Δ}_{C0}, and (d) Circulating current controller and gate signal generation.

Annex E. Modulation scheme and sorting algorithm

In this thesis, a single modulation scheme has been employed, specifically the Level-Shifted Multicarrier Modulation, in which all triangular carriers are in phase. The implementation of this modulation scheme is carried out on a Xilinx Kintex-7 XC7K325T FPGA operating at a clock frequency of 100 MHz. The triangular carriers are generated using Up/Down counters that range from 0 to 4999, each with corresponding offsets for its carrier level. Further details regarding the implementation of the Level-Shifted Multicarrier Modulation can be found in the reference [90].

When the counters reach their minimum and maximum values, a signal with a duration of one clock cycle is generated to synchronise all voltage and current measurements. Additionally, it triggers an interrupt signal that executes the control routine on the processor, resulting in double-edge sampling. This setup yields triangular carriers with a frequency of 10 kHz and a sampling frequency of 20 kHz. Fig. E.1 illustrates one of the carriers and how it synchronises with the trigger signal.

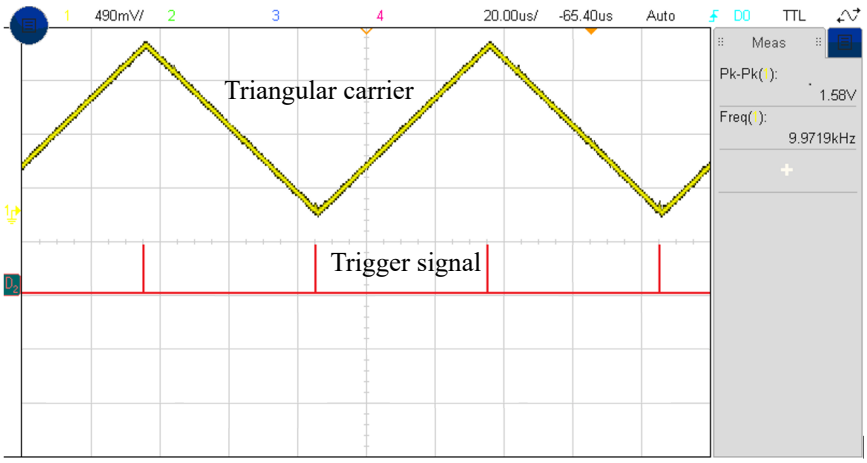

Figure E.1: Carrier and synchronization signal.

The sorting algorithm is also implemented within the FPGA. This algorithm rearranges the switching signals generated by the modulation strategy, taking into consideration the voltage sign to be synthesised, the sign of the current flowing through the cluster, and the magnitudes of the capacitor voltages. If the cluster current and voltage are in the charging phase, submodules with lower capacitor voltages are inserted. Conversely, if the cluster current and voltage are in the discharging phase, submodules with higher capacitor voltages are inserted. This algorithm operates at a slower pace than the control strategy, running at a frequency of 2.5 kHz to minimise the number of commutations caused by the sorting process.

Annex F. Proof of the Submitted Paper

Continuous Control Set Model Predictive Control of a Hybrid-MMC for Wind Energy Applications

Journal:	*Transactions on Industrial Electronics*
Manuscript ID	Draft
Manuscript Type:	Regular paper
Manuscript Subject:	Renewable Energy Systems
Keywords:	Predictive control, Power conversion, Wind energy
Are any of authors IEEE Member?:	Yes
Are any of authors IES Member?:	Yes